

Jet Cross-Sections at 8 TeV with the ALICE Experiment.

A Dissertation Presented for the

Doctor of Philosophy

Degree

The University of Tennessee, Knoxville

Andrew John Castro

December 2019

© by Andrew John Castro, 2019

All Rights Reserved.

“Most people are not looking for provable truths. As you said, truth is often accompanied by intense pain, and almost no one is looking for painful truths.”

— Haruki Murakami

Acknowledgments

My time in Tennessee has been some of the most enriching, fun, and frustrating time in my life. Through my time here, I have had one steadfast pillar that supported me through it all, Megan. I could never thank you nor love you enough.

To my family. I would like to thank my father, Jaime. For shaping me into the man I have become and for the long hikes and backpacking trips that we've done together. He helped curate my love and passion for being in the outdoors. I would like to give a very special thanks to my sister Ali, her husband Adam, my amazing nieces Amara, Amelia, and my equally amazing nephew Alyas. I would also like to thank Nancy, Jim, and Lindsey along with all the members of the Swanton and Stobie families for making me feel like a part of them.

Thank you to my best friend Saul. For all the great memories we've had growing up together, for the crazy trips to India and Mexico, and for taking a Grey Hound from San Francisco to Knoxville to visit me.

I would like to deeply thank the heavy ion group at the University of Tennessee for the support they gave me. I would like to Soren Sorensen and Christine Nattrass for their

guidance. To Rebecca and Kyle for becoming life long friends. To Pat, Redmer, and Adam for giving me input and trouble shooting on the analysis.

I would also like to thank the members of my committee; Christine Nattrass, Ken Read, Soren Sorensen, and Ivan Maldonado.

Abstract

In nuclear collisions a deconfined state of partons, quarks and gluons, interact creating a near ‘perfect’ fluid called the Quark–gluon plasma(QGP). As this state of matter expands and cools, the quarks once again combine into the hadrons measured in particle detectors. Understanding the energy loss mechanisms of this phase of matter is one of the major goals of the nuclear physics program at the Large Hadron Collider(LHC).

The first principle processes that govern hadronization are not understood from a theoretical Quantum Chromodynamic (QCD) framework, but are well described phenomenologically using Monte Carlo simulations. As partons interact with one another, they fragment into collimated sprays of particles known as jets. The topologies and properties of hadronic jets measured in collider experiments can be correlated to the hadronization phase in nuclear collision. Measuring jet cross-sections as a function of the jet radius in high energy experiments can constrain different hadronization models from one another and allow for more precise measurements of the QGP.

Inclusive jet cross sections and ratios of jet cross sections are measured in this thesis using the 2012 proton–proton data collected at $\sqrt{s} = 8$ TeV with the ALICE detector at the LHC. This thesis presents results of jets with radii from 0.2 to 0.4, over a wide kinematic

range between $20 \text{ GeV}/c$ and $100 \text{ GeV}/c$ in momentum. This thesis used both minimum bias and single shower triggered data from the ALICE Electromagnetic Calorimeter. The cross sections are corrected for detector effects by unfolding and the results are compared to Monte Carlo simulations using Pythia, Herwig, and PHOJet in order to gauge different hadronization effects.

Table of Contents

1	Introduction	1
2	Quantum Chromodynamics	4
2.1	The QCD Lagrangian	4
2.2	Jets	6
2.3	Jet Finding Algorithms	16
2.4	Monte-Carlo Generators	23
2.5	The Quark-Gluon Plasma	25
3	The LHC and ALICE	33
3.1	Overview of The LHC	33
3.2	The ALICE Experiment	36
4	The ALICE TPC Upgrade	48
4.1	Physics Motivation	48
4.2	Gaseous Electron Multiplier Foils	51
4.3	Research and Development	53
4.4	Production of The Inner Readout Chambers	58

4.5	GEM and Chamber Quality Assurance	60
4.6	Outlook	64
5	8 TeV Data Selection	66
5.1	Min Bias and EMCAL Triggered Events	67
5.2	EMCAL Clusters	71
5.3	TPC Tracks	75
5.4	Raw Jet Reconstruction	78
6	Corrections and Systematic Uncertainties	84
6.1	Raw Jet Spectra	85
6.2	Acceptance Correction	89
6.3	EMCAL Triggered Data and Scaling	89
6.4	Particle Level Corrections	94
6.5	Jet Reconstruction and Matching Efficiency	104
6.6	Systematic Uncertainties	105
7	Jet Results and Outlook	114
7.1	8 TeV Inclusive Jet Results and Discussion	114
7.2	Summary and Conclusion	123
Bibliography		126
Appendix		142
A	Particle Identification via Bethe-Bloch	143

List of Tables

5.1	2012 8 TeV data taking period.	68
6.1	EMCal jet acceptance for radii 0.1 - 0.5.	90
6.2	Summary of JES and Yield Uncertainties.	113

List of Figures

1.1	The fundamental particles of the Standard Model[1].	2
2.1	Strong coupling constant (α_s) as a function of the momentum transfer (Q)[2].	6
2.2	Diagram showing a jet created by two partons undergoing a hard scattering, forming into hadrons, and detected in a calorimeter[3].	7
2.3	Schematic of a proton-proton collision. Starting from the bottom, two partons confined within the colliding protons have a hard interaction. The outgoing partons will induce partonic showers by radiating quarks and gluons. The partonic showers will eventually form into final state hadrons, due to confinement, which are measured in high energy experiments[4].	9
2.4	Proton PDF at $Q^2 = 10$ GeV (left) and $Q^2 = 10$ TeV (right) from the NNPDF Collaboration[5].	11
2.5	Lowest order quark-antiquark annihilation to top-antitop pair[6].	12
2.6	Parton cascade in a hadronic collision[7].	13
2.7	$u\bar{d}$ generating a $d\bar{d}$ pair via string breaking which will form color neutral hadrons, black lines show the string like equipotentials.[8].	14

2.8	Fragmentaion functions from e^+e^- and DIS experiments with fits[9] as a function of the total cross-section, σ .	16
2.9	Cartoon showing collinear and infrared safe jet candidates[10].	17
2.10	Lego plot of all four jet finders used on a single event with $R = 1$ jet radius[11].	22
2.11	The QCD phase diagram[12].	26
2.12	Comparison of the processes in a proton-proton collision with no medium and a heavy-ion collision with a colored medium stage[13].	28
2.13	Jet energy loss in a QCD medium[12].	29
2.14	Jet R_{AA} at 5.02 TeV with the ATLAS experiment[14].	31
3.1	LHC accelerator complex. The four main experiments are shown in their relative locations[15].	34
3.2	The ALICE Detector at CERN[16].	38
3.3	ALICE tracker, multiplicity, timing, and vertex detectors located near the interaction point[16].	38
3.4	The ALICE Time Projection Chamber[17].	40
3.5	The TPC readout region[18].	41
3.6	TPC momentum and tracking resolution[19].	43
3.7	ALICE EMCal along with super modules, tower strips, and towers[20].	44
3.8	Energy resolution in the EMCal measured in a 2007 test beam at CERN (blue) compared to GEANT3 simulations of the EMCal (orange), fits for the parameters A, B, and C are also shown[21].	46

3.9 Cluster Spectra from the ALICE EMCal. MinBias is shown in black while the red and blue points show the spectra using the gamma trigger at two energy thresholds[22].	47
4.1 Simulation of the invariant mass spectra for dileptons in a typical heavy-ion run with current ALICE performance (left) and after upgrade of ALICE for Run-3 (right) in PbPb at $\sqrt{s_{NN}} = 5.5$ TeV. The dilepton yields originating from the QGP are shown (red and orange), along with background contributions from light-hadrons (blue), and charm (magenta)[23].	50
4.2 Scanning electron microscope image of a GEM foil from top (left) and profile (right)[24].	51
4.3 Profile of GEM with electric-field lines and gradients (left). Simulation of an ionization electron (yellow line) entering a GEM from a drift volume, amplification electrons (green dots, yellow lines) and back flow ions (red lines) are created (right)[25].	52
4.4 ITS-TPC matching (<i>left</i>) and inverse momentum resolution (<i>right</i>) for a 4-GEM stack simulated in Garfield++ [26].	54
4.5 Final design of the upgraded readout chambers with a stack of 4 GEMS [27].	55
4.6 dE/dx resolution of the 4-GEM IROC prototype(<i>left</i>) and the separation power between electrons and pions as a function of gain (<i>right</i>)[28].	56
4.7 Energy resolution of the iron peak as measured from the prototype IROC with varying GEM voltages as a function of IBF%[28].	57

4.8	Simulation of the four GEM (blue) layers after test beam. The configuration is such that the two GEMs closest to the drift volume (right) absorb the amplification ions created by the two GEMs closest to the readout (left) [28].	57
4.9	The author assembling an Inner Readout Chamber at Tennessee.	58
4.10	Production flow of the IROCs (red), OROCs (blue), and GEM foils (green)[26].	
	59
4.11	Schematic for the setup of the GEM foil spark test (<i>left</i>)[29] and the GEM mounted in the HV gas box (<i>right</i>).	61
4.12	Schematic of the gas tightness testing setup at the University of Tennessee <i>(Courtesy of Joseph Rasson)</i>	62
4.13	Leak rate of the 49 chambers built at Tennessee with the maximum failure rate at 0.25 ml/hr shown <i>(Courtesy of Charles Hughes)</i>	63
4.14	Testing for chamber sparking next to the LHC beam line (<i>left</i>) and real time output from the spark test during a live beam (<i>right</i>).	64
5.1	LHC state during the 8 TeV run.	66
5.2	Min Bias event rejection summary.	70
5.3	Vertex displacement from primary interaction point for accepted Min Bias events.	70
5.4	EMCal cell occupancy after bad channels removed.	71
5.5	Matched track-cluster distance.	73
5.6	EMCal cluster time distribution before cuts.	74
5.7	Corrected EMCal cluster yield.	74

5.8	Hybrid Track η and ϕ yields.	77
5.9	Accepted hybrid track resolution.	78
5.10	Accepted track p_T yield.	78
5.11	$R = 0.2$ leading track p_T per jet p_T	79
5.12	$R = 0.2$ number of constituents in a jet per jet p_T	80
5.13	$R = 0.2$ $z_{leading}$ from the Min Bias data sample.	81
5.14	Jet rejection reason.	82
5.15	$R = 0.2$ NEF per jet P_T	83
6.1	Raw inclusive $R = 0.2$ jet spectra from the 8 TeV Min Bias and EMCal triggered data	86
6.2	Raw inclusive $R = 0.3$ jet spectra from the 8 TeV Min Bias and EMCal triggered data	87
6.3	Raw inclusive $R = 0.4$ jet spectra from the 8 TeV Min Bias and EMCal triggered data	88
6.4	Distance to closest reconstructed jet patch to $R = 0.2$ jet with the EMCal triggered data.	91
6.5	Distance to closest reconstructed gamma patch to $R = 0.2$ jet with EMCal triggered data.	92
6.6	EMCal triggered data correction factors for $R=0.2$, $R=0.3$, and $R=0.4$ jets.	93
6.7	Response Matrices for $R = 0.2$ (top left), $R=0.3$ (top right), and $R = 0.4$ (bottom) jets.	96
6.8	$R = 0.2$ bin-by-bin corrected Min Bias jet spectra.	98

6.9	$R = 0.3$ bin-by-bin corrected Min Bias jet spectra.	99
6.10	$R = 0.4$ bin-by-bin corrected Min Bias jet spectra.	100
6.11	$R = 0.2$ bin-by-bin corrected EMCAL triggered jet spectra.	101
6.12	$R = 0.3$ bin-by-bin corrected EMCAL triggered jet spectra.	102
6.13	$R = 0.4$ bin-by-bin corrected EMCAL triggered jet spectra.	103
6.14	Jet reconstruction efficiency for jets between $R = 0.2$ and $R = 0.4$.	105
6.15	Jet reconstruction efficiency for jets between $R = 0.2$ and $R = 0.4$.	106
6.16	Systematic due to TPC tracking efficiency.	108
6.17	Systematic due to Hadronic correction.	108
6.18	Systematic due to clusterization algorithm.	109
6.19	Inclusive TPC track momentum resolution, Min Bias 8 TeV.	110
6.20	Systematic due to P_T resolution.	111
6.21	Systematic due to energy resolution.	111
7.1	8 TeV inclusive jet differential cross-section for $R = 0.2$.	115
7.2	8 TeV inclusive jet differential cross-section for $R = 0.3$.	116
7.3	8 TeV inclusive jet differential cross-section for $R = 0.4$.	117
7.4	Ratio of the jet cross-sections $R = 0.2$ to $R = 0.4$.	120
7.5	Ratio of the jet cross-sections $R = 0.3$ to $R = 0.4$.	121
7.6	Ratio of the jet cross-sections $R = 0.2$ to $R = 0.3$.	122
7	Energy loss of a muon traversing a copper medium between 0.1 MeV to 100 TeV [1].	143

8	Specific energy loss for the ITS(<i>left</i>) and the TPC(<i>right</i>) with Bethe-Bloch fits from different particle species traversing each detector[30].	144
---	---	-----

Chapter 1

Introduction

From the Vedas to the ancient Greeks, generations have described the constituents of nature in terms of indivisible ‘elements’. It wasn’t until the beginning of the 20th century that the ancient elements of earth, wind, fire, and water were abandoned for the atomic theory of nature. By the 1960’s, what would become known as the Standard Model of Particle Physics was taking shape. The four ancient elements were replaced by the two fundamental particles types: the mass carrying fermions with spin 1/2, and the force carrying bosons with spin 1, as seen in Figure 1.1.

The Standard Model is the unification of the three symmetry groups, $SU(3) \times SU(2) \times U(1)$, representing the strong, weak, and electromagnetic forces respectively[31]. In terms of scientific accomplishments, the Standard Model is one of the most tested theories of nature with an agreement between the theory and observed results up to ten digits[32]. Even though the Standard Model gives us a deep understanding of many natural phenomena and has a wide range of uses, from understanding the evolution of the Big Bang, the bonding of atoms and molecules, and the nature of light, to cancer treatments and nuclear security,

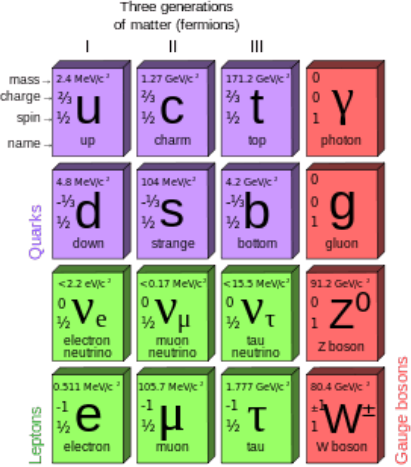


Figure 1.1: The fundamental particles of the Standard Model[1].

it is fundamentally an incomplete theory of nature. The fact that Gravity has yet to be unified into a quantum theory tells us that the Standard Model is incomplete. High energy experiments give us some of the most extreme conditions possible to test the Standard Model and to look for phenomena outside of the theory. Are there new symmetries and laws that manifest at high energies? Can we create dark matter or dark energy in a laboratory? Are quarks and leptons fundamental or finite in size? Do the four fundamental forces emerge from some yet unknown unified force? And why is antimatter absent in the Universe? All of these open questions are of great interest and currently form large areas of active research.

The theory of strong interactions, Quantum Chromodynamics QCD is described by the SU(3) group and is analogous to Quantum Electrodynamics (QED) with gluons being the force mediator instead of photons and quarks carrying mass. Quarks and gluons are known as partons and are particles that interact via the strong force. At low energies and over large length scales, partons are confined to a color neutral state and they must clump together into color neutral hadrons. As two colored partons begin to separate, at some point it becomes energetically favorable to create a quark–antiquark pair out of the vacuum rather

then expanding the distance between neighboring partons. Due to confinement, high energy scatterings between two partons will lead to a spray of hadrons known as a ‘jet’. The other main attribute of QCD is asymptotic freedom, as the interactions between partons become more energetic and the length scale decreases, the strong coupling constant becomes exceedingly small, $\alpha_{strong} \ll 1$, and the partons freely interact with one another. Due to asymptotic freedom, nuclear matter undergoes a phase transition called the Quark–Gluon Plasma (QGP) at high energies and densities.

The analysis performed during this thesis explored jet production and kinematics in proton-proton collisions at the Large Hadron Collider. It will also report constraints on the different mechanisms involved in jet production and help serve as a baseline for jet measurements in heavy-ion collisions.

This thesis will present an overview of QCD in Chapter 2, with an emphasis on jet physics and heavy ion collisions. Chapter 3 will give a brief overview of the LHC and the ALICE experiment, including the relevant subsystems for this thesis. Chapter 4 will discuss the contribution to the upgrade of the ALICE Time Projection Chamber performed during my Ph.D. studies. A discussion of quality control and assurance performed on the data collected from ALICE is given in Chapter 5. Chapter 6 will discuss the analysis corrections and systematic error calculations. Finally, Chapter 7 will present the final fully corrected results and give an outlook on the analysis.

Chapter 2

Quantum Chromodynamics

In 1968 deep inelastic scatterings performed at the Stanford Linear Accelerator Center showed that the proton had internal structure[33] called partons at the time. Within a decade of this discovery the partons were broken into two categories: the mass carrying fermions were known as the quarks and the gauge boson force carriers were called gluons. The interactions of these two types of particles were described by the quantum field theory known as Quantum Chromodynamics (QCD) and by the SU(3) symmetry group. SU(3) guarantees that color charge is conserved and this results in quarks grouping together into ‘colorless’ hadrons.

2.1 The QCD Lagrangian

QCD is the strongest of the known fundamental forces. It is a gauge field theory described by the Lagrangian density

$$\mathcal{L} = -\frac{1}{4}F_{\mu\nu}^\alpha F_\alpha^{\mu\nu} - \alpha_s(\bar{q}_j \gamma_\mu T_\alpha q_j)G_\alpha^\mu + \bar{q}_j(i\gamma^\mu \partial_\mu - m)q_j \quad (2.1)$$

where q and \bar{q} represent the color/anti-color fields summed over color j , α_s is the strong coupling strength, γ^μ is the Dirac gamma matrix, G_α^μ is the gauge field for color α , G_α^μ is similar in analogy to the \mathbf{W} matrix from the electroweak theory. $F_{\mu\nu}^\alpha$ is the field strength tensor and it describes the gluon interactions. The first term of the Lagrangian is the gluon contribution and carries no mass variable. The second term describes how quarks and gluons interact with each other. The final term describes quark interactions and the coupling between them and will be explored further in this thesis.

At short distances, less than 0.2 fm , the strong coupling constant becomes exceedingly small and the second term of the Lagrangian displays an important property known as asymptotic freedom[34]. Numerically the strong coupling constant is given as,

$$\alpha_s = \frac{1}{\beta_0 \ln(Q^2/\Lambda^2)} \quad (2.2)$$

where α_s is the strong coupling constant, Q^2 is the momentum transfer between two interacting partons, Λ^2 is a cutoff below which QCD phenomena are strongly suppressed, and β_0 is a scale factor. Figure 2.1 shows the value of α_s as a function of the momentum transfer measured from various particle experiments and clearly shows the decreasing strength at high energies.

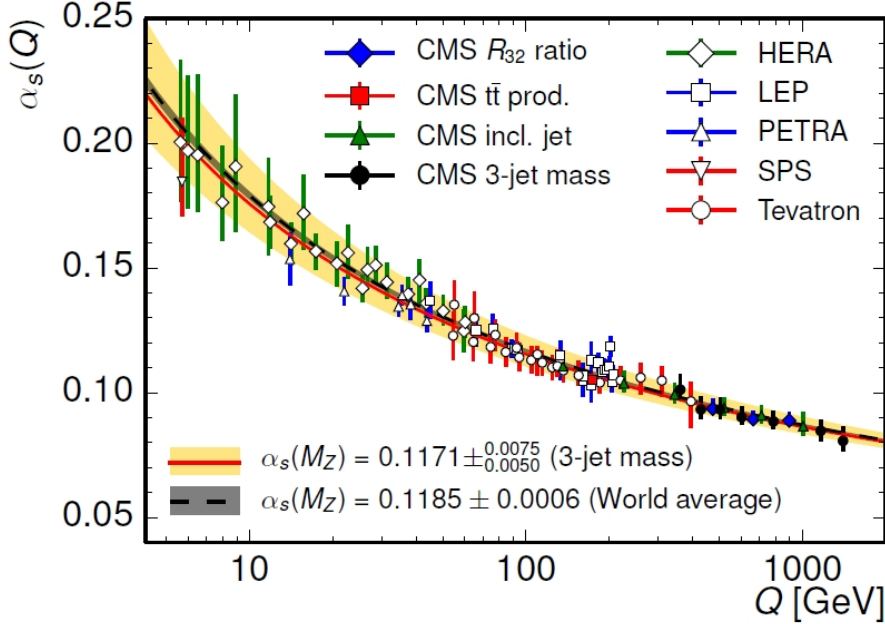


Figure 2.1: Strong coupling constant (α_s) as a function of the momentum transfer (Q)[2].

2.2 Jets

Hard probes (large Q^2 interactions), are produced in the earliest stages of a high energy collision when the largest momentum transfer processes occur. The interaction and scattering of partons is a $2 \rightarrow 2$ process, meaning that two partons will interact and the outgoing partons also come in pairs. As two highly energetic partons propagate away from one another they will instigate a shower of daughter partons via gluon radiation and the generation of low-mass $q\bar{q}$ pairs. These daughter partons will go on to form collimated sprays of hadrons known as a ‘jet’. If the jet was created in a high energy experiment, the final state hadrons will be recorded as tracks in a tracking detector or energy deposits in a calorimeter. This process is shown in Figure 2.2.

The physicist James Daniel Bjorken postulated that a correlation could be surmised by summing over the final state transverse momentum of the hadrons that form a jet to the

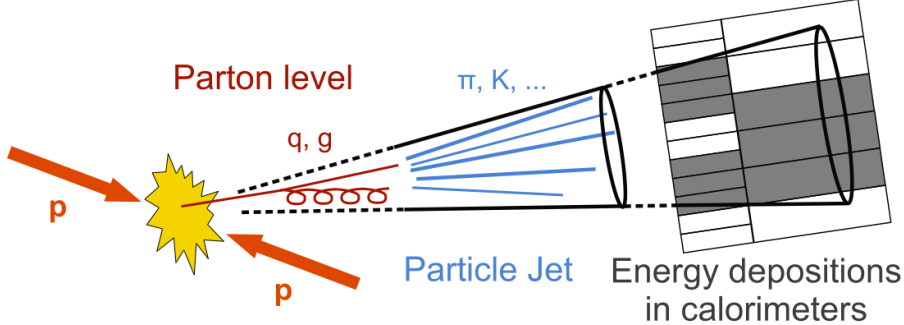


Figure 2.2: Diagram showing a jet created by two partons undergoing a hard scattering, forming into hadrons, and detected in a calorimeter[3].

parton that initiated the hard scattering[35][36]. This has led to jets becoming the work-horse for both experimentalists and theorists over the past 30 years in probing QCD phenomena. This thesis makes use of jets as an important probe of QCD and the following sections are devoted to developing a background for both the theoretical and experimental treatment of jet physics. The following sections of this chapter will be devoted to the background of jet production.

Jet Production and The Factorization Theorem

Due to confinement bare quarks are unobserved, therefore experimentalists must probe QCD interactions by detecting the color neutral final state hadrons measured in collider experiments. The factorization theorem allows for the final state jet cross section to be broken into a number of steps that can either be calculated perturbatively using pQCD or modeled phenomenologically. Using the factorization theorem the jet cross section in a pp collision is:

$$d\sigma^{pp \rightarrow jet} \sim f_{a/A}(x_1, Q^2) \otimes f_{b/B}(x_2, Q^2) \otimes d\sigma_{ab \rightarrow c+X}(x_1, x_2) \otimes D_{c \rightarrow h/jet}(z, Q^2) \quad (2.3)$$

Breaking Equation 2.3 down we have:

- $f_{a/A}(x_1, Q^2)$ and $f_{b/B}(x_2, Q^2)$ are the parton distribution functions (PDF) that describe the probability of finding parton, a or b , within nuclei, A and B , with a given momentum fraction, $x = p_{parton}/p_{hadron}$ as a function of Q^2 .
- $d\sigma_{ab \rightarrow c+X}(x_1, x_2)$ is the pQCD parton-parton cross section due to the hard scattering of the two partons, a and b , to an intermediate parton (c).
- $D_{c \rightarrow h/jet}(z, Q^2)$ is the fragmentation function (FF) that describes the probability that an outgoing parton, c , fragments and hadronizes into a final state hadron, h , within a jet with momentum fraction, $z \equiv p_{hadron}/p_{parton}$.

Figure 2.3 shows a cartoon of a pp collision broken into the relevant steps in accordance with the factorization theorem. The best place to test QCD phenomena using hard probes, i.e. jets, is at high energy hadron colliders, such as those found at CERN¹, Fermilab, and BNL. The time scale that a hard probe is created in a high energy collision is on the order of $\tau \approx 1/p_T \approx 0.1 \text{ fm}/c$ at $p_T = 1 \text{ GeV}$, which corresponds to some of the earliest stages of the nuclear collision. The factorization theorem is an incredible tool for understanding high energy interactions and the following sections will discuss the important concepts enveloped in it.

¹Discussed in detail in Chapter 3

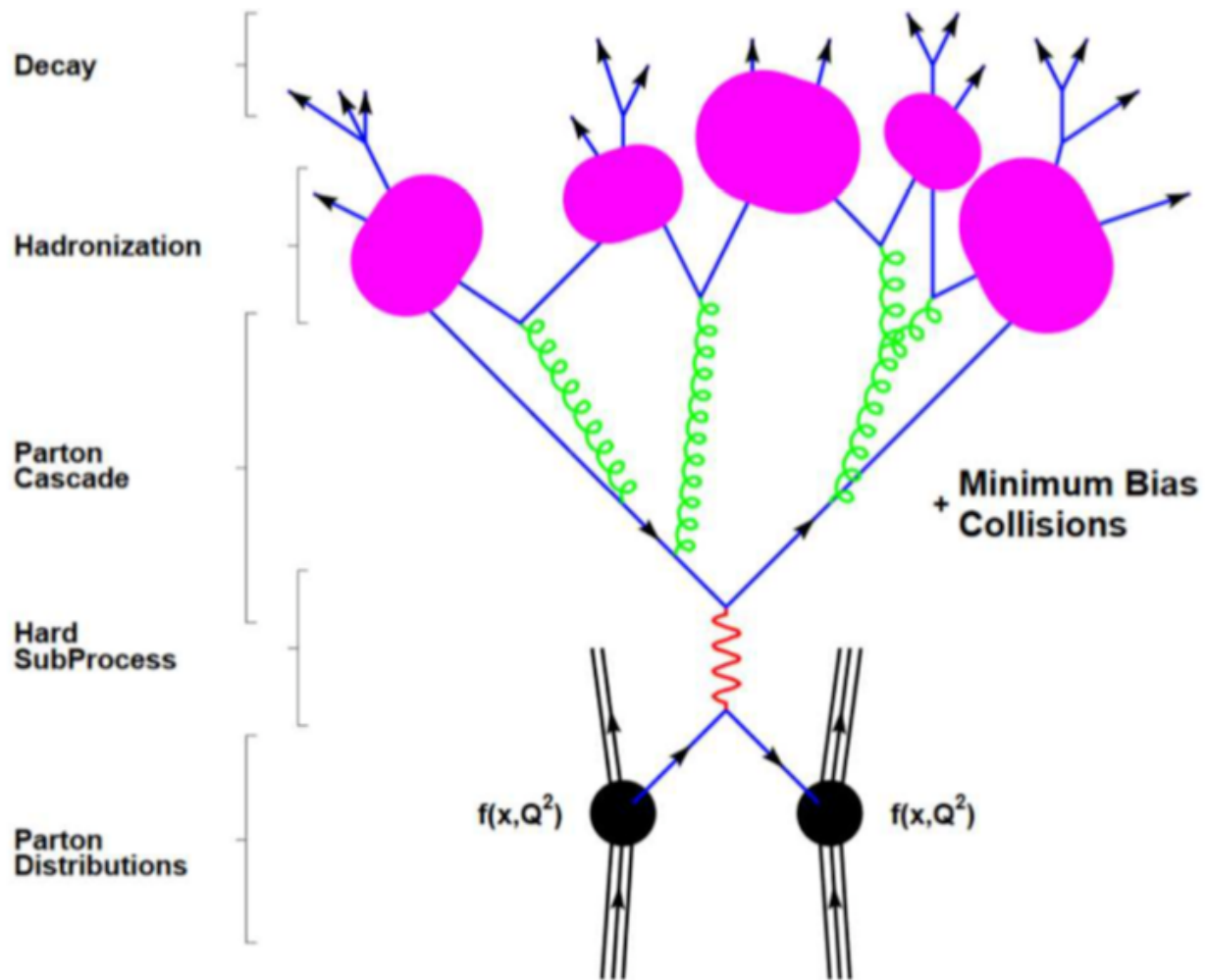


Figure 2.3: Schematic of a proton-proton collision. Starting from the bottom, two partons confined within the colliding protons have a hard interaction. The outgoing partons will induce partonic showers by radiating quarks and gluons. The partonic showers will eventually form into final state hadrons, due to confinement, which are measured in high energy experiments[4].

Parton Distribution Functions

The PDF occurs twice in Equation 2.3 due to the two partons that will undergo the hard scattering being confined in two different protons. PDFs convey the structure of a nucleon in terms of the number of flavored quarks or gluons ($u(x)$, $d(x)$, $s(x)$, $\bar{u}(x)$, $\bar{d}(x)$, $\bar{s}(x)$, $g(x)$) and must obey certain constraints and summation rules. In the case of a proton, with electric charge ($e = +1$),

$$+1 = \frac{2}{3} \int_0^1 [u(x) - \bar{u}(x)] dx - \frac{1}{3} \int_0^1 [d(x) - \bar{d}(x)] dx \quad (2.4)$$

and isospin ($I = 1/2$),

$$\frac{1}{2} = \frac{1}{2} \int_0^1 [u(x) - \bar{u}(x)] dx - \frac{1}{2} \int_0^1 [d(x) - \bar{d}(x)] dx \quad (2.5)$$

have a solution,

$$\int_0^1 [u(x) - \bar{u}(x)] = 2 \quad (2.6)$$

$$\int_0^1 [d(x) - \bar{d}(x)] dx = 1 \quad (2.7)$$

This corresponds to the classical partonic view that protons contain two up quarks and a down quark similarly, and similarly the neutron, with charge $e = 0$ and isospin $I = -1/2$, is composed of two down quarks and an up quark. Naively, we could assume that the three quarks composing a proton would each carry a momentum fraction of approximately $1/3$ the total momentum of a proton. However, high energy deep inelastic scattering experiments

conducted at the Stanford Linear Collider in the 1960's[37] measured the momentum carried by the three quarks as only accounting for about 1/2 the total proton momentum. This led to a more complex and dynamic model of the proton structure with the other half of the proton momentum being carried by neutral partons, which would eventually become known as gluons.

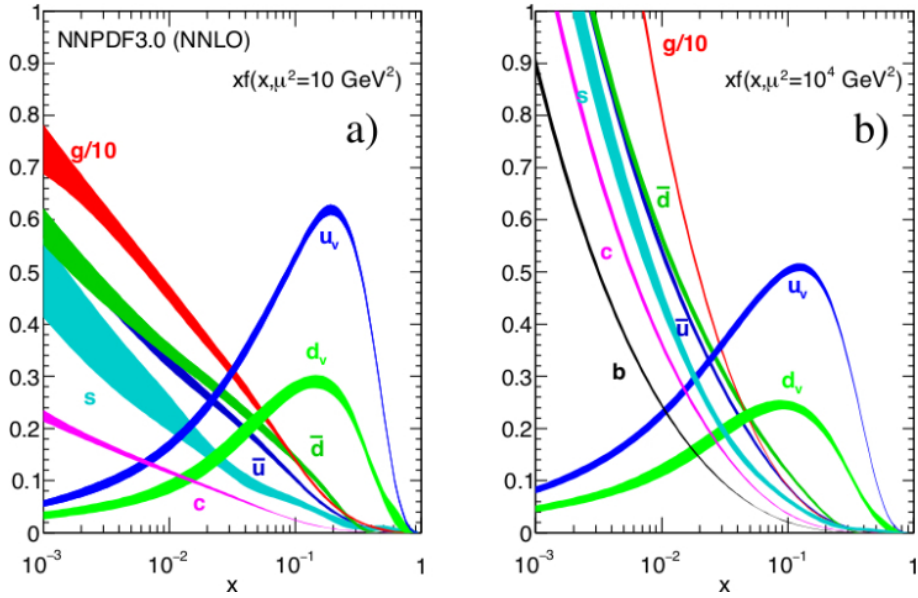


Figure 2.4: Proton PDF at $Q^2 = 10 \text{ GeV}$ (left) and $Q^2 = 10 \text{ TeV}$ (right) from the NNPDF Collaboration[5].

Determining the structure of the partons making up a nucleon is a major endeavor by both theorists and experimentalists. Two of the most popular PDFs available to physicists are the CTEQ[38] (Coordinated Theoretical-Experimental Project on QCD) and the NNPDF[39] (Neural Network Parton Distribution Function) sets. Figure 2.4 shows the proton PDF as a function of the momentum fraction for two energy ranges. At high values of x , the two up quarks account for about 2/3 of the momentum fraction while the down quark accounts for about 1/3 of the total momentum. These quarks are collectively called the valence quarks. At high energies (low values of x) we see that the proton has non negligible contributions

from gluons, anti-quarks, strange, and even charm quarks. These are collectively known as the sea partons. Today, the modern picture of a proton's structure is mostly composed of gluons and sea quarks at low values of x and this domination only increases as a function of Q^2 [40].

Parton-Parton Cross-Section

The quark-pquark, quark-gluon, and gluon-gluon cross section can be calculated using perturbation theory. To the zeroth order in α_s this cross-section would be a simple quark-antiquark annihilation and would be calculable using Feynman diagrams as seen in Figure 2.5[41]. Higher ordered contributions, such as the creation of virtual gluons, require the hard cross-section to be expanded as a series in terms of α_s . Calculations of the hard cross-section that incorporate these higher order terms are known as *next-to-leading order* (NLO) with N denoting the number of terms after the leading order that have been included in the cross-section calculation. Various calculations of the hard cross-section of different QCD processes have been performed over the years typically using either power series or logarithmic expansions of α_s [42] and corrections for LO, NLO, and even NNLO constitutes a very active field in high energy physics. Perturbative techniques of the hard cross-section have been extremely successfully in describing jet features in hadronic collisions[40].

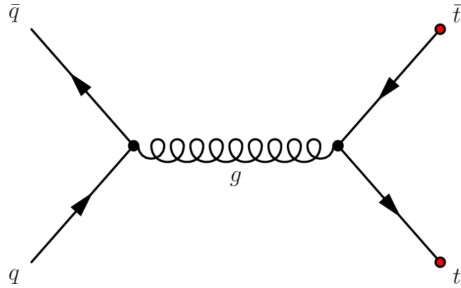


Figure 2.5: Lowest order quark-antiquark annihilation to top-antitop pair[6].

Hadronization

Hadronization, the process by which the colored pQCD partons form into colorless non-pQCD hadrons, represents a significant barrier in progressing jet physics. This is due to the fact that hadronization encompasses several smaller processes, which in themselves are hard to characterize. Thus, like PDFs, an accurate description of hadronization requires a phenomenological approach by which experimental results help complement theoretical calculations. Jet production via hadronization[7] follows two distinct stages. First, the partons that underwent a hard scattering start to emit radiation via gluon bremsstrahlung up until time, $t < Q^2$. This is known as the parton cascade. The parton cascade is the precursor to a jet as most of the radiation generated will travel in the same direction as the initial hard scattered parton. However, this immediately poses an issue in jet physics as radiation generated at a wide angle away from the momentum axis of the initial hard scattered parton will not be associated with the jet.

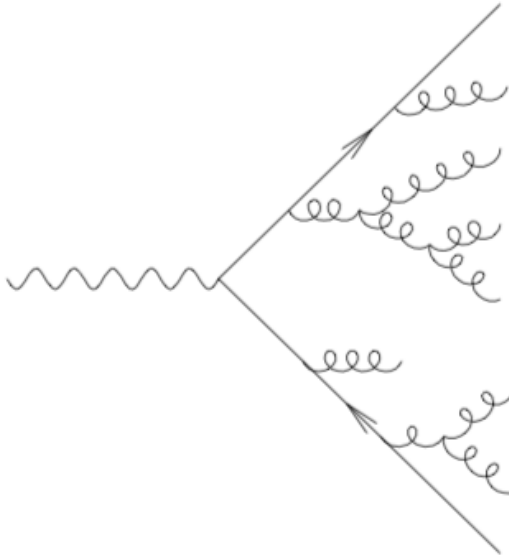


Figure 2.6: Parton cascade in a hadronic collision[7].

After the cascade has ended, the partons form into color neutral hadrons. There are two main phenomenological models used to describe the hadron forming process, the Lund String Model and the Cluster Hadronization Model.

The QCD potential is

$$V(r) = -\frac{\alpha_s}{r} + \sigma r \quad (2.8)$$

where the first term of Equation 2.8 is similar to the Coulomb potential with a $1/r$ dependence and is the dominate term at short distance. The second term has a string-like potential with σ referring to a string-like tension. The Lund String Model uses this potential, ignores gluon radiation, and has fragmentation occur via breaking the string tension with the production of $q\bar{q}$ sea quarks. The created sea quarks will carry some momentum fraction, z , of the initial parton until z falls below some cutoff. Figure 2.7 shows two quarks undergoing a string breaking, each of the quarks initiating the string breaking will combine with a sea quark in an iterative manner to form hadrons.

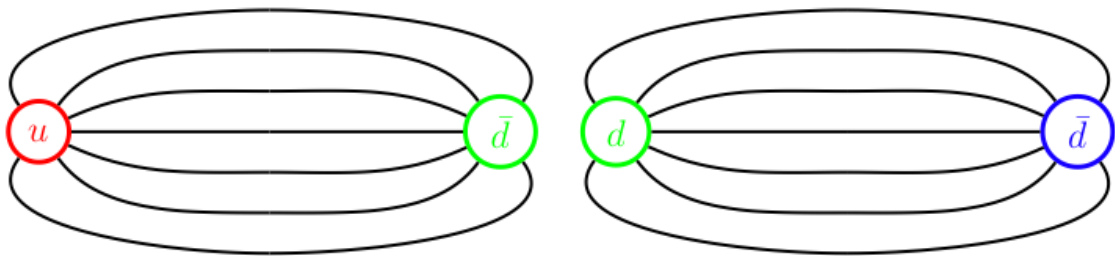


Figure 2.7: $u\bar{d}$ generating a $d\bar{d}$ pair via string breaking which will form color neutral hadrons, black lines show the string like equipotentials.[8].

The Cluster Hadronization Model has gluons splitting after the parton cascade phase into $q\bar{q}$ pairs. These pairs will form color-singlet clusters with other neighboring quarks in

phase-space. These color-singlets will typically be a few GeV/c^2 in mass and are treated as excited meson resonances. These psuedo-resonances will decay via their normal branching ratios into the stable hadrons[43].

Fragmentation

Similar to the way a PDF quantitatively describes the structure of a nucleon, the fragmentaion function (FF) quantitatively describes the hadronization process. The FF is also similar to the PDF in that it is also a probability distribution, thus it follows the probabilistic rule that

$$\sum \int_0^1 z D_{c \rightarrow h/jet}(z, Q^2) dz = 1 \quad (2.9)$$

where the sum is carried over the particles constituting the jet, $c \rightarrow h/\text{jet}$ states that the function in question is only concerned with a parton, c, fragmenting into a final state particle, h, that is part of a jet. The fractional momentum of the hadrons created from the fragmenting parton, $z \equiv p_{\text{hadron}}/p_{\text{parton}}$, is an exponentially decreasing distribution between 0 and 1 which shows how fragmented hadrons carry the partial energy from the initial parton scattering. Parton-Hadron Duality[44] states that the leading hadron should correlate with the kinematic properties associated with the hard scattered quark that initiated the jet. Thus we can measure the fragmentation function as $z = p_{\text{hadron}}/p_{\text{jet}}$. The formulation of the FF as the fractional energy carried by the hadrons in a jet was a breakthrough in pQCD techniques and is analogous to the way an electron passing through an absorber creates

photon showers. These photons continue generating conversion electrons until the total energy has been dissipated into the material.

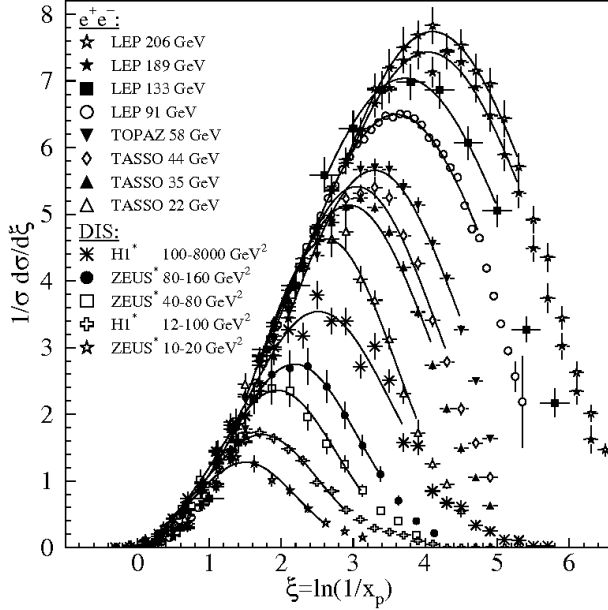


Figure 2.8: Fragmentation functions from e^+e^- and DIS experiments with fits[9] as a function of the total cross-section, σ .

Figure 2.8 is the FF in terms of the Gaussian equation, with σ referring to the total cross-section, $z dN/dz = -dN/d\xi$, and $\xi = -\ln 1/z_p$. The Gaussian peaks in Figure 2.8 along with the suppression of the FF at low z values due to gluon coherence were predicted by pQCD.

2.3 Jet Finding Algorithms

A jet arises from the fragmentation of a hard parton to final state hadrons. However, grouping the hadrons together into a jet is ambiguous. Jet finding algorithms are used because they standardized the definition between theorists and experimentalists and give results comparable to each other. Early on in jet physics, both theorists and experimentalists used

a wide variety of jet finders and definitions which made comparisons between experiments or to theoretical calculations nearly impossible[11]. For example, a radiated gluon that splits into a quark anti-quark pair may become one or two jets depending on the angular separation and the algorithm used. Early jet finders tended to be sensitive to soft particles or could give widely varying yields to the number of jets in an event. In 1990, the Snowmass Accord[45] reached a standardized definition of a jet between experimentalists and theorists. The agreement maintained that any algorithm that clusters particles into a jet must be both infrared and collinear safe (IRC).

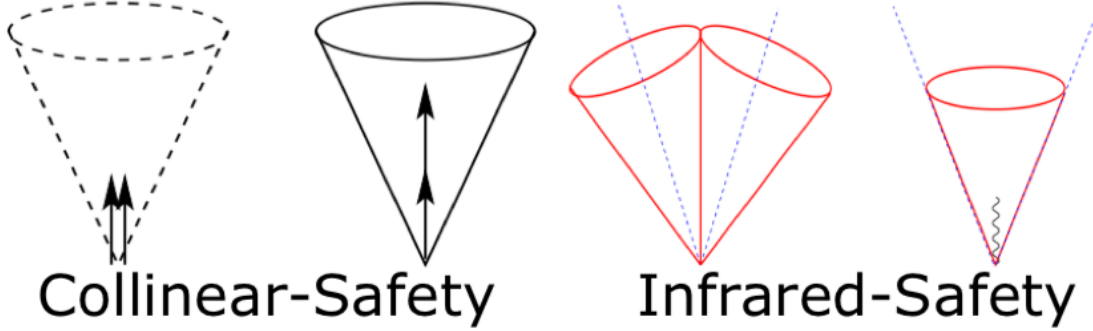


Figure 2.9: Cartoon showing collinear and infrared safe jet candidates[10].

A hard, high momentum transfer, scattered parton will undergo collinear splittings, emissons of gluons, as part of the fragmentation process. This is a difficult process to model theoretically so jet finding algorithms maintain collinear safety. Collinear safety ensures jets remained unchanged due to any gluon emissions. Infrared safety in turn requires that the emission of soft radiation should not affect jet. This makes jets returned by the algorithm a signature of a hard process. Both of these processes are shown in Figure 2.9. After the adoption of these standards from the Snowmass Accord, old algorithms that violated these rules were patched and new jet finders were developed to comply with IRC safety. The

most prevalent jet finding algorithms today fall into two categories: cone algorithms and sequential recombination/clustering algorithms.

Cone Algorithms

Cone algorithms made up the bulk of early jet finders. The only IRC safe cone algorithm still in use today is the seedless infra-red safe cone algorithm (SIScone). SIScone defines a cone of radius R around the highest momentum particle in the coordinates of (η, ϕ) ². This is the proto-jet. SIScone then proceeds through an iterative process of finding all the particles within the jet radius such that $R \leq \sqrt{\phi^2 + \eta^2}$ and calculates a new jet center based on these particles' momenta and a new weighted jet axis (η, ϕ) . If the new center matches the proto-jet center, the proto-jet is tagged as a stable jet. All the particles in that jet are removed and SIScone moves onto the next highest p_T particle. Cone algorithms tend to be unpopular due to being computationally expensive, difficult to implement theoretically, and can give results not calculable in perturbation theory.

Sequential/Recombination Algorithms

The other class of jet finders are the sequential/recombination algorithms, which are favored by experimentalists and theorists, and are IRC safe. There are three sequential/recombination algorithms: k_T , Anti- k_T , and the Cambridge/Aachen jet finders, with

²It is possible to use a Cartesian coordinate system in particle colliders, with the z-component referring to points along the beam axis while the xy-plane is perpendicular to the beam axis. However, this system is not invariant under a Lorentz boost. Therefore it is more useful to use the cylindrical-like coordinates of pseudorapidity (η) and the azimuth angle (ϕ). Pseudorapidity may be thought of as the polar angle in a cylindrical coordinate system with $\eta = 0$ when the polar angle is perpendicular to the beam axis and $\eta = \infty$ along the beam axis. ϕ is the azimuth angle that rotates around the beam axis. Both, η and ϕ are invariant for Lorentz boosts along the beamline and allow for easy comparisons between the center-of-mass frame and the laboratory frame of a high energy collision.

k_T referring to the component of a jet constituent's momentum perpendicular to the jet axis. All of the algorithms use a similar method. First they find the distance between every pair of particles, $d_{i,j}$, such that

$$d_{i,j} = \min[p_{T,i}^a, p_{T,j}^a] \frac{\Delta_{ij}^2}{R^2} \quad (2.10)$$

where $p_{T,i}^a$ is the transverse momentum of particle i , a is free parameter that is set based on which algorithm is used, $\Delta_{ij}^2 = (\eta_i - \eta_j)^2 + (\phi_i + \phi_j)^2$ is the distance between the particles, and R is the radius of the jet. A second distance is defined in the sequential/recombination algorithm scheme,

$$d_{i,B} = p_{T,i}^a \quad (2.11)$$

which is only a function of the particles transverse momentum. Sequential/Recombination algorithms find the set of all particles, $d_{i,j}, d_{i,B}$, such that if $d_{i,B}$ is the minimum for particle i it is tagged as a jet and removed from the list. If $d_{i,j}$ are a minimum for particles i and j these two particles are merged together into a new particle (ij) and a new minimum is found between (ij) and a new particle k until all the particles are either merged into jets or the minimization function is no longer satisfied.

k_T Algorithm

The k_T algorithm sets the value a to 2, this results in a minimization function,

$$d_{i,j} = \min[p_{T,i}^2, p_{T,j}^2] \frac{\Delta_{ij}^2}{R^2} \quad (2.12)$$

which clusters low momentum particles first, making this algorithm susceptible to the underlying event, UE, or pile-up, PU. Thus the k_T algorithm is good at estimating any background present in a high energy collision.

Anti- k_T Algorithm

The Anti- k_T algorithm sets the value a to -2, resulting in a minimization function,

$$d_{i,j} = \min \left[\frac{1}{p_{T,i}^2}, \frac{1}{p_{T,j}^2} \right] \frac{\Delta_{ij}^2}{R^2}. \quad (2.13)$$

The minimization function begins with high- p_T particles, thus the area and axis of a jet is only slightly perturbed by soft particles. This makes the Anti- k_T algorithm robust in jet finding with events having pile-up. The Anti- k_T algorithm is the default jet finding algorithm used at the Large Hadron Collider and is the one used in this thesis.

Cambridge/Aachen Algorithm

The Cambridge/Aachen algorithm sets a to 0 and this results in a minimization function of,

$$d_{i,j} = \frac{\Delta_{ij}^2}{R^2} \quad (2.14)$$

which makes it independent of particle momentum and sensitive to PU and the UE. Due to the fact that the Cambridge/Aachen algorithm is only dependent on the particle coordinate it is most useful in studying jet structure.

Figure 2.10 shows the jets found in a single event using all four jet finding algorithms. It should be noted that the Cambridge/Aachen and k_T algorithms have highly irregular and

large shapes, making them both susceptible to the presence of a UE, while SIScone finds an additional jet due to splitting. The Anti- k_T algorithm finds circular jets which demonstrates its' robustness to hard radiation.

Once a stable jet is found, a recombination scheme is deployed in order to garner the jet kinematics. By adding the 4-vector, $\mathbf{p}^\mu = (\mathbf{E}, \mathbf{p}_x, \mathbf{p}_y, \mathbf{p}_Z)$, for all of the associated particles composing a jet, we may obtain the jet momentum, energy, coordinates, etc. In a particle collider with the tracks from a tracking detector measuring particle momentum and the towers of a calorimeter measuring particle energy we obtain the following relationships

$$p_T^{jet} = \sum_{particles} p_T = \sum_{tracks} p_T \quad (2.15)$$

$$E^{jet} = \sum_{particles} E = \sum_{towers} E \quad (2.16)$$

$$\eta^{jet} = \frac{1}{2} \ln \left(\frac{|\mathbf{p}^{jet}| + p_L^{jet}}{|\mathbf{p}^{jet}| - p_L^{jet}} \right) \quad (2.17)$$

$$\tan \phi^{jet} = \frac{p_y^{jet}}{p_x^{jet}} \quad (2.18)$$

where p_L refers to the longitudinal momentum which is the momentum component parallel to the beam axis, η^{jet} and ϕ^{jet} are the jet coordinates in psuedo-rapidity and the azimuth angle. This method of adding the 4-vector of the particles composing the jet together in order to gain the jet kinematics is known as the E-scheme[46].

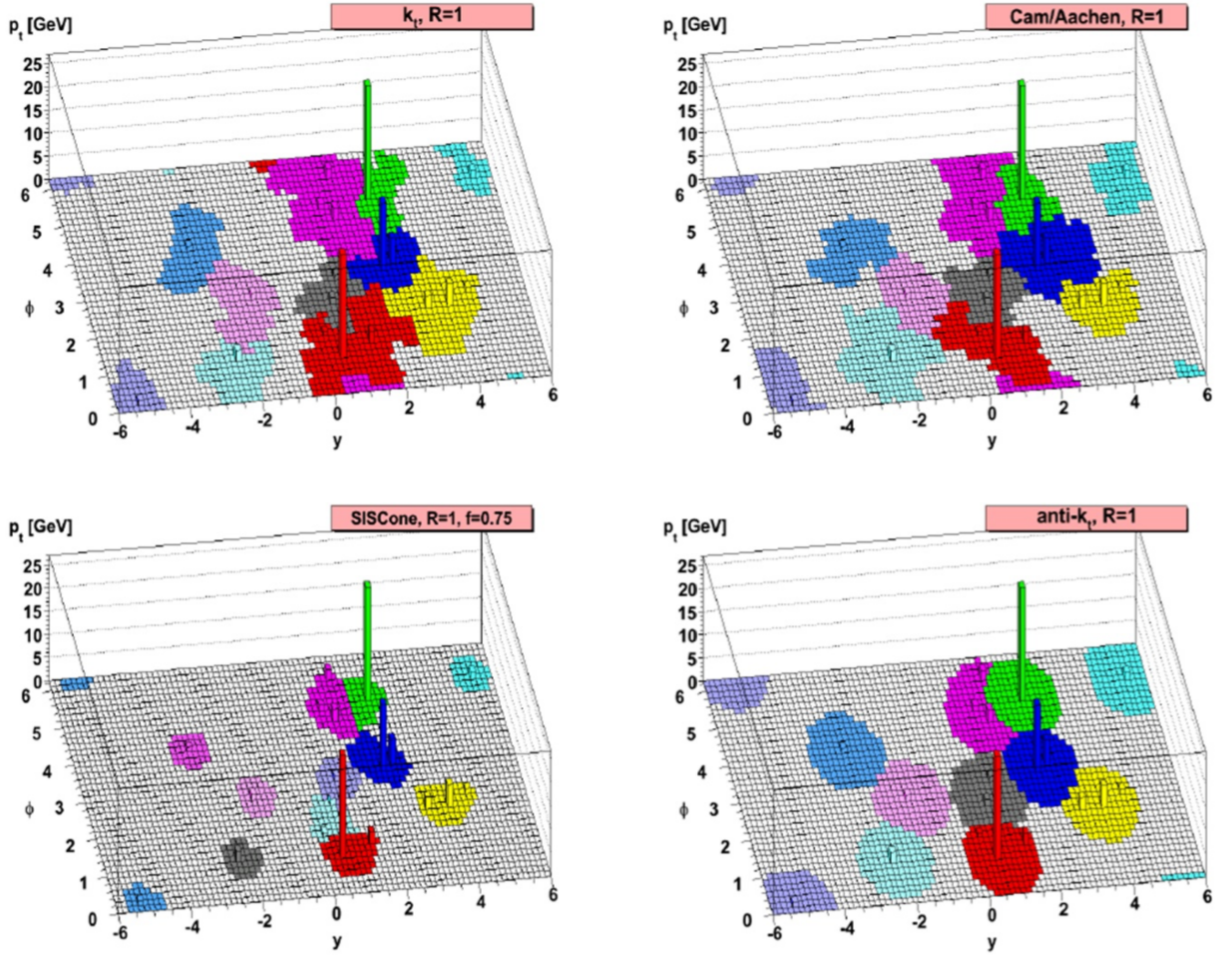


Figure 2.10: Lego plot of all four jet finders used on a single event with $R = 1$ jet radius[11].

FastJet

FastJet[46] is a C++ software package that performs jet finding. Due to the computational efficiency, ease of use, and straight forward implementation, FastJet is the preferred jet finding software package used by theorists and current high energy experiments. It implements the four previously discussed jet finders along with both the E-scheme and a boost invariant p_T scheme (BIpt-scheme) for recombination. The BIpt-scheme obtains the jet momentum and energy in the same manner as the E-scheme but uses a weighted average to find the jet coordinates,

$$\eta^{jet} = \sum_{particle} \frac{p_T^{particle}}{P_T^{jet}} \eta^{particle} \quad (2.19)$$

$$\phi^{jet} = \sum_{particle} \frac{p_T^{particle}}{P_T^{jet}} \phi^{particle} \quad (2.20)$$

In addition to basic jet measurements, FastJet contains a number of advance features, which allows it to be used to study jet area, jet substructure, and jet background subtraction[47].

2.4 Monte-Carlo Generators

Monte Carlos allow for the simulation of high energy events on a statistical basis. Particle level generators use different phenomenological models of the factorization theorem in order to simulate the energy, momentum, particle species, multiplicity, and direction of travel expected in a high energy collision. In this thesis Monte Carlos are also used to understand and correct for inefficiencies due to the experiment using a GEANT simulation of ALICE, this is discussed in more depth in Chapter 5. The following sections will go over some of the

different Monte Carlos used in this thesis and the physics behind how they simulate high energy collisions.

PYTHIA

PYTHIA[48], is a Monte Carlo software tool-kit used to model proton-proton collisions. The package uses pre-defined parton distribution functions as input. Afterwards it simulates the partonic showers and radiation due to a hard scattering by generating the leading-order, LO, scattering matrix elements. Hadronization is performed in PYTHIA using the Lund String Model. The final state hadrons are formed using the branching ratios to decay excited states.

PYTHIA underestimates jet production due to the limitations of using LO calculations. Therefore, it uses an arbitrary value (K-factor) to make NLO corrections to the LO cross section. The K-factor is defined as

$$K = \frac{\sigma_{NLO}}{\sigma_{LO}}. \quad (2.21)$$

NLO corrections to the cross-section will not match experimental results, especially at low energies. PYTHIA implements additional phenomenological adjustments used to better match data. PYTHIA encompasses these parameters into sets known as ‘tunes’, with PYTHIA 6.4 Perugia-2010 tune being used for this analysis[49].

PHOjet

PHOjet is a **FORTRAN 77** Monte Carlo simulator used to model proton-proton collisions. It is an alternative to PYTHIA and is better at modeling soft physics processes present in high

energy collisions. PHOjet implements the Dual Parton model[50][51] and multiple parton interactions[52] to model soft physics, similar to Pythia. Hard interactions are implemented in PHOjet using LO scattering elements and it uses PYTHIA for the fragmentation and hadronization phase. Due to its ability to model soft physics, PHOjet is better at comparing to Min Bias³ data and understanding jet results in a low kinematic range. PHOjet also acts as a benchmark in understanding any bias due to using other Monte Carlo generators, such as PYTHIA. PHOjet v1.2 is used in this thesis.

HERWIG

The Herwig[53] Monte Carlo generator is a **FORTRAN** software package used to generate proton-proton events. It is similar to PYTHIA in that it calculates the LO hard scattering of partons, however it uses the cluster model of hadronization to produce jets based on gluon splitting. It is also similar to PHOjet in regards to the evolution of final state jets with soft gluon angular ordering. By comparing Herwig, PYTHIA, and PHOjet it is possible to test for sensitivities to jet production in high energy events due to different types of hadronization models and soft radiation.

2.5 The Quark-Gluon Plasma

At the temperatures and pressures typical to the universe today nuclear matter is confined to a colorless hadrons. However, it was theorized that at extreme temperatures, such as those experienced in the early universe, partons would have undergone a phase transition where

³Events with a low total transverse momentum and high cross section

they were no longer bound in a color neutral state. This state of matter would have been analogous to a conventional plasma where the electrons are no longer bound to a nucleus, thus the state was dubbed the Quark-Gluon Plasma (QGP).

The nuclear phase diagram is shown in Figure 2.11 as a function of temperature and the net baryon density. Normal nuclear matter is confined to the bottom left while increasing temperatures and/or densities correspond to the QGP. Modern particle colliders, such as RHIC and the LHC, are able to obtain the densities and temperatures necessary to create a QGP and are likewise shown in the figure. The reason for particle colliders being located at low baryon density is due to the fact that at collider energies at mid-rapidity the plasma are dominated by quark-antiquark pairs, so the net baryon density is close to zero. This dilutes the total baryon density in the initial system and is more akin to what the early Universe was like.

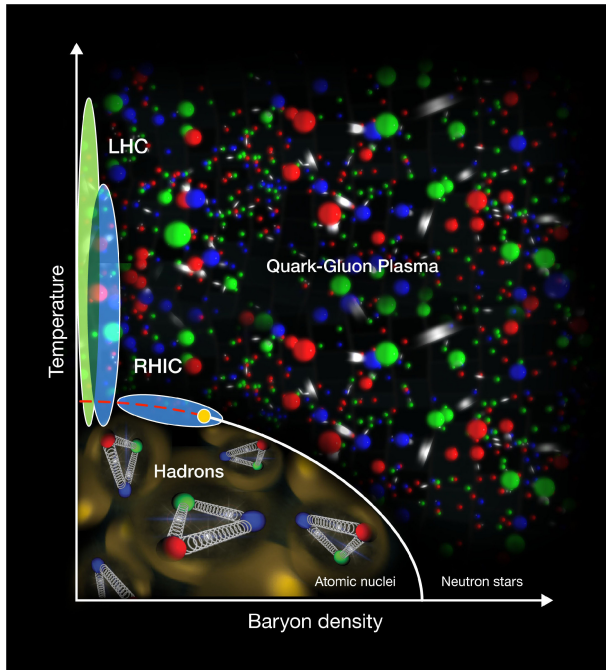


Figure 2.11: The QCD phase diagram[12].

Nuclear Collisions

By colliding heavy nuclei together in high energy colliders it is possible to obtain the energy densities and temperatures associated with the QGP. The first signatures for the QGP were measured via a J/ψ suppression at the Super Proton Synchrotron, located at CERN in 2000[54]. In 2005, the four experiments on the RHIC collider: BRAHMS[55], PHENIX[56], PHOBOS[57], and STAR[58], co-announced the observation of a new state of matter consistent with the hot and dense QGP. The results from RHIC indicated that the QGP behaves more like a perfect fluid over a plasma-like state[59].

Figure 2.12 shows the difference between a proton-proton collision and a heavy-ion collision. The heavy-ion collision mirrors the processes in a proton-proton collision (left) described in depth in Section 2.2. After the initial hard scattering the phase transition to a QGP occurs. The QGP undergoes a hydrodynamical evolution and expansion until it cools to a colorless hadronic gas. After the phase transition occurs hadrons will undergo chemical reactions until the final particle species is set, once these reactions cease we have a chemical freeze-out. The hadron gas continues to expand and cool until all soft elastic interactions and momentum transfers cease. This is the kinetic freeze-out, after which the final momentum spectra is set. Understanding how the final particle composition accounts for the measured light-nuclei seen in heavy-ion collisions was the topic of a paper I published and more information about this subject in heavy-ion physics can be found here[60].

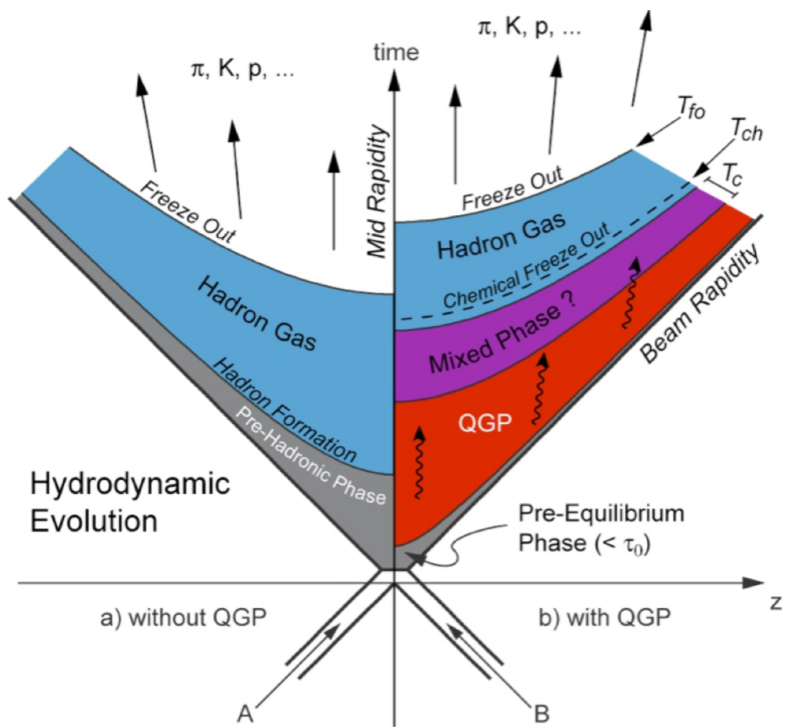


Figure 2.12: Comparison of the processes in a proton-proton collision with no medium and a heavy-ion collision with a colored medium stage[13].

Jets and The QGP

Jets are an excellent probe of the properties of the QGP. Jets are produced in the earliest stages, before the formation of the QGP, and survive the full evolution of a heavy-ion collision. As a jet propagates through the QGP, it will lose energy to the medium through a combination of gluon radiation to the colored medium and inelastic scatterings. These energy loss mechanisms are dependent on the distance a parton travels through the QGP and on the species of the parton.

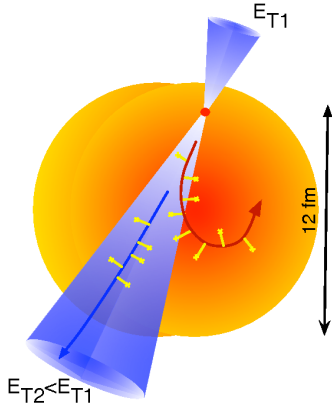


Figure 2.13: Jet energy loss in a QCD medium[12].

Figure 2.13 shows two back-to-back partons undergoing a hard scattering. Both will fragment into jets, but the first parton with transverse energy, E_{T1} , will be subjected to much less energy loss over the second parton due to the first parton only traveling through the outer edge of the QGP. The species dependent partonic energy loss arises from kinematic constraints to gluon emission from the heaviest of quarks. This radiation is suppressed at angles smaller than the ratio of the quark mass to its energy and has been dubbed the *Dead-Cone Effect*[61]. Tagging the flavor dependence of jets, either via measuring electrons from semi-leptonic decays or reconstructing the secondary vertex of heavy flavor mesons, has

recently shown that energy loss via the Dead-Cone Effect is strongly suppressed with jets containing a charm quark[62].

One way of quantifying the energy loss in a heavy-ion collision is via measurements of the nuclear modification factor, R_{AA} ,

$$R_{AA} = \frac{1}{N_{binary}} \frac{d^2 N_{AA}/dp_T d\eta}{d^2 N_{pp}/dp_T d\eta} \quad (2.22)$$

where N_{binary} is the number of nucleon-nucleon collisions and is estimated using a Glauber model[63] of a nucleus while $d^2 N_{AA}/dp_T d\eta$ and $d^2 N_{pp}/dp_T d\eta$ are the spectra measured in nucleus-nucleus and proton-proton collisions respectively. R_{AA} may be thought of as asking the question: Does a heavy-ion collision scale as a superposition of N_{binary} nucleon-nucleon collisions? A R_{AA} value of 1 corresponds to no modification in a heavy ion collision not already present in a proton-proton collision. The observation of R_{AA} below unity shows a suppression of jets in heavy-ion collisions. Where does the missing energy go? This is still a subject for debate and it is not clear whether the energy may propagate outside of the cone radius of the jet or if the energy may become thermalized in the medium.

Figure 2.14 shows the nuclear modification factor with $R = 0.4$ jets in the ATLAS experiment at 5.02 TeV[14]. The different colored bands in the figure are centralities⁴

⁴The purple 10 - 20% band denotes the most central events (i.e. the two colliding nuclei have a low impact parameter and collide nearly head-on), while the 70 - 80% red band denotes the least central events (i.e. the two colliding nuclei have a high impact parameter and barely graze one another). An in depth discussion of centrality may be found here[64].

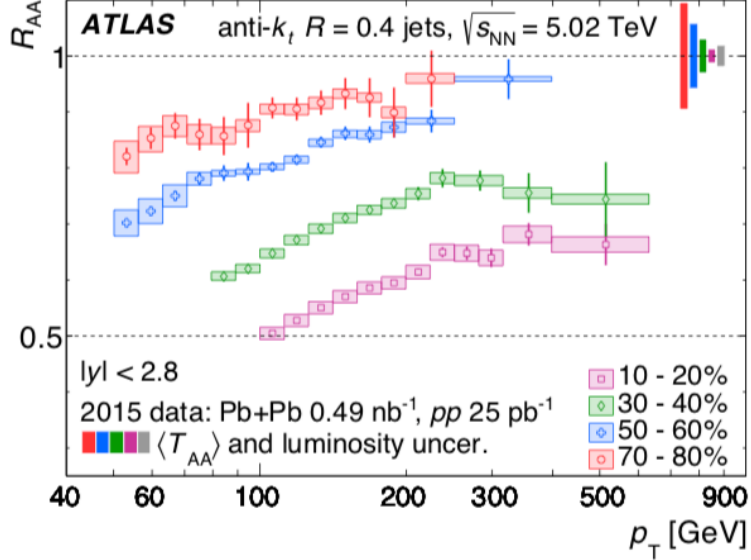


Figure 2.14: Jet R_{AA} at 5.02 TeV with the ATLAS experiment[14].

Collectivity in Proton-Proton Collisions

As previously stated a QGP is believed to be absent in proton-proton collisions, thus any signature of a QGP should likewise be absent. However, one way of quantifying the presence of the QGP is via the Bjorken energy density.

$$\varepsilon = \frac{1}{\tau A} \frac{dE_T}{d\eta} \quad (2.23)$$

where A is the transverse area of the nuclei, τ is the proper time, and $dE_T/d\eta$ is the transverse energy per unit psuedorapidity. It can be shown that the 150 MeV critical temperature need for the phase transition to the QGP corresponds to $1 - 3 \text{ GeV}/fm^3$ energy density. The quantity $dE_T/d\eta$ can be related to the mean transverse momentum $\langle p_T \rangle$ and particle multiplicity⁵ per unity psuedorapidity as:

⁵Multiplicity is defined as the number of particles per event

$$\frac{dE_t}{d\eta} \approx \langle p_T \rangle \frac{dN}{d\eta} \quad (2.24)$$

where $\langle p_T \rangle$ is the mean transverse momentum and $dN/d\eta$ is the particle multiplicity per unit pseudorapidity. This suggests that in very high multiplicity proton-proton events signatures of the QGP may be present. Although suppression has never been observed in high multiplicity proton-proton collisions, physicists have recently measured azimuthal correlations in such systems[65]. This gives a ‘hint’ that flow may be present in high multiplicity proton collisions. CMS presented results in proton-proton collisions at 13 TeV using soft-particles, $p_T \leq 2 \text{ GeV}/c$, consistent with hydrodynamical predictions[66]. These results have opened new debates and questions into the very nature of the QGP. Measuring jets to high accuracy over a wide kinematic range is important because it serves as a baseline measurement for the inducing the QGP properties in heavy-ion collisions. This will be explored in more detail throughout the rest of this thesis.

Chapter 3

The LHC and ALICE

3.1 Overview of The LHC

The Large Hadron Collider (LHC)[\[67\]](#) is a circular particle accelerator located on the Franco-Swiss border near the city of Geneva. It is operated by the European Organization for Nuclear Research (CERN) and has carried out proton-proton (pp), lead-proton (pPb), and lead-lead (PbPb) collisions at center of mass energies of 0.9-14 TeV, 5.0 TeV, and 2.76-5.5 TeV, respectively. The LHC is approximately 17 miles in circumference and is located 200 meters underground, inside the old accelerator tunnel used by the Large Electron-Positron[\[68\]](#) collider of the 1980's. There are over 8000 physicists and engineers making up the four main experiments at the LHC: ATLAS[\[69\]](#), CMS[\[70\]](#), LHCb[\[71\]](#), and ALICE[\[72\]](#). Numerous physics results have been published, with the most famous being the discovery of the Higgs boson in 2012[\[73\]](#)[\[74\]](#).

Figure [3.1](#) shows a schematic of the LHC along with the pre-accelerators that help to accelerate protons and ions to their final energies before a collision at one of the four

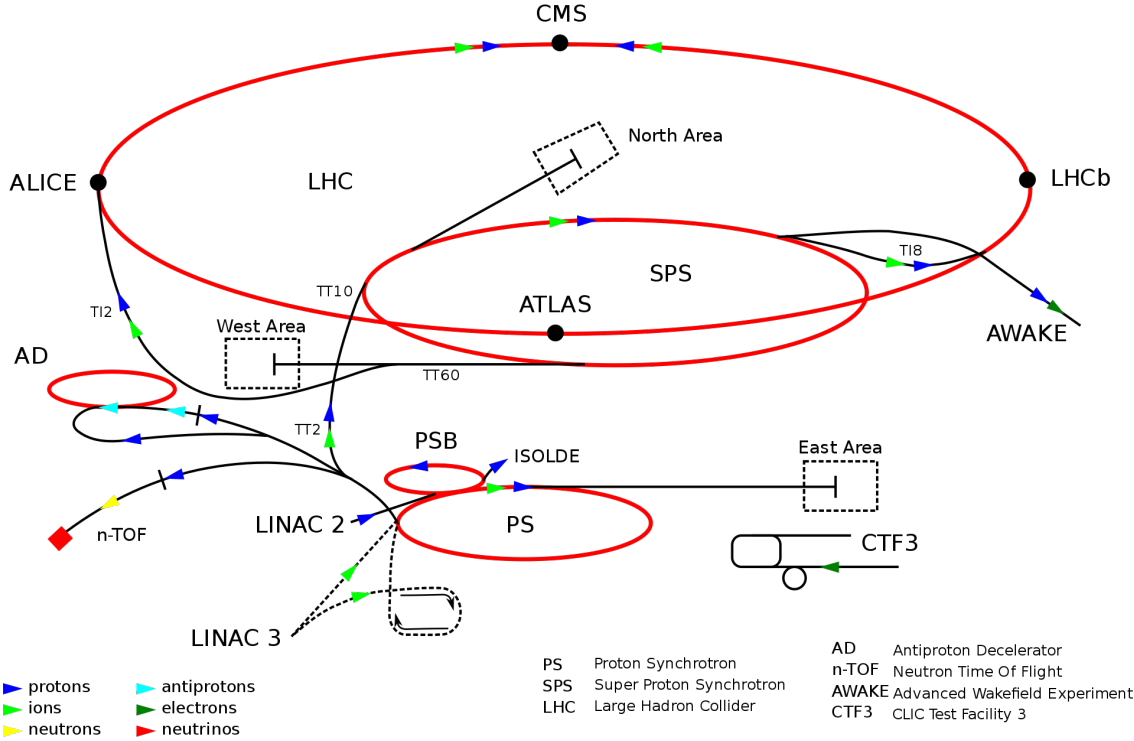


Figure 3.1: LHC accelerator complex. The four main experiments are shown in their relative locations[15].

experimental interaction points (IP). Protons are injected into the LHC in groups called ‘bunches’. Every bunch is comprised of about 120 billion protons with about 50 nanoseconds between the arrival of the next bunch. The bunch scheme during the heavy-ion run is reduced to 200 nanoseconds due to the high multiplicity of the events and additional computational resources needed.

LHC Operations

The LHC first attempted particle collisions in September of 2008. The initial ramping up of the super conducting magnets led to mechanical failure of the helium pipes inside of the LHC beam line. This fault caused the LHC to remain shut down for over a year while the accelerator was repaired and new safety procedures were implemented. The first successful

collisions occurred in 2009 with proton collisions at a reduced energy of 0.9 TeV. 2010 marked the beginning of a new era in the high energy frontier with proton collisions at a record setting 7 TeV. The only other major fault that has occurred was in the summer of 2016. A stone marten chewed through a high voltage line in a power transformer on a ground level building at the LHC. The LHC went offline for about a week while repairs occurred and quickly resumed the physics program. Unfortunately, the marten did not survive.

The typical operating year at the LHC allows for any repairs or upgrades on the experiments to be performed during the offline period for the first few months. After the offline period, the proton physics program begins and lasts until approximately mid-November. The heavy-ion program begins after the proton physics run and lasts until the first week of December, after which the LHC shuts down for the remainder of the year.

From 2014 until early 2015 the LHC was shutdown for major renovations and upgrades to the accelerator and a number of sub-detectors on each experiment. This was known as long shutdown 1 (LS1). Since the end of 2018, the LHC has been in another long shutdown (LS2), which aims at upgrading the accelerator to a high luminosity, Hi-Lumi. This will be discussed in detail along with the upgrades to ALICE in Chapter 4.

LHC Accelerator Complex

The LHC accelerator complex is a succession of particle accelerators that increase the energy of particles before they are injected into the next accelerator. Hydrogen atoms are first passed through a high voltage environment that strips any electrons from around the proton. Once the protons are stripped of their electrons, they are injected into the linear accelerator (LINAC). The LINAC uses radio frequency cavities to accelerate particles to 50 MeV before

they enter the first circular accelerator the Proton Synchrotron (PS). The PS begins to focus the protons into bunches and further accelerates them to 1.4 GeV before the beam enters the Super Proton Synchrotron (SPS). The SPS accelerates the particles to 450 GeV. The beam is then injected into the LHC and accelerated to the final collision energy. Afterwards the beam gets ‘squeezed’, or tightly focused, with a series of quadrupole magnets. The final step is to ‘adjust’ the beam to overlap with the counter-rotating beam at the four interaction point (IP) where the main LHC experiments are located. Once the adjust phase is completed, collisions will occur at each experiment and data collection begins. This entire process from stripping the electrons to collisions in each IP takes 20 minutes.

In order for the beam parameters to be maintained in the LHC, numerous dipole and quadrupole magnets are used to accelerate, focus, and bend the particle beams. The magnets use a superconducting niobium-titanium alloy that is maintained at an operating temperature of 1.9 K using helium-4. Upgrading these magnets is one of the major goals during LS2 as part of the Hi-Lumi upgrade of the LHC[75].

3.2 The ALICE Experiment

A Large Ion Collider Experiment (ALICE) is a general purpose detector that covers a solid angle of 4π around the IP. It is 26 m long, 16 m high, 16 m wide, and weighs approximately 10,000 tons[75]. Like many other large scale detectors, ALICE is made up of 18 sub-detectors that perform tracking, particle identification (PID), timing, vertex reconstruction, and calorimetry.

Figure 3.2 shows the ALICE detector with human figures to set the scale. Figure 3.3 shows the area closest to the interaction point with the TZERO, VZERO, Inner Tracking System and Forward Multiplicity Detector. These detectors give basic information on the collision such as vertex location, centrality, and timing. Further out from the central region are a number of tracking detectors, like the Time Projection Chamber and Time-of-Flight detectors, which focus on measuring charged particle momentum and PID. Next are the calorimeters that measure particle and jet energies, such as the Electromagnetic Calorimeter, Photon Spectrometer, and Dijet Calorimeter. All of these sub-detectors are housed in the L3 magnet, seen as the red octagon in Figure 3.2. The L3 magnet provides an approximately uniform magnetic field of 0.5 T over the central area of ALICE and helps ensure the high PID performance ALICE has over a wide kinematic region[76]. At high rapidity, there is a muon tracker and trigger for muon identification. The following sections give a more detailed discussion of the sub-detectors used for this analysis

TZERO

The TZERO (T0)[77] detector is a double layer Cherenkov counter located at 70 cm (T0A) and 370 cm (T0B) from the IP. The T0 functions as a trigger and timing detector that determines the precise moment in time at which an event ‘starts’ in the ALICE detector. The timing information from the T0 is fed to other sub-detectors, like the Time-of-Flight and Time Projection Chamber detector, which is used for track reconstruction. in the case of the Time Projection Chamber The T0 also gives feedback on the target luminosity of the ALICE experiment to the LHC operations center.

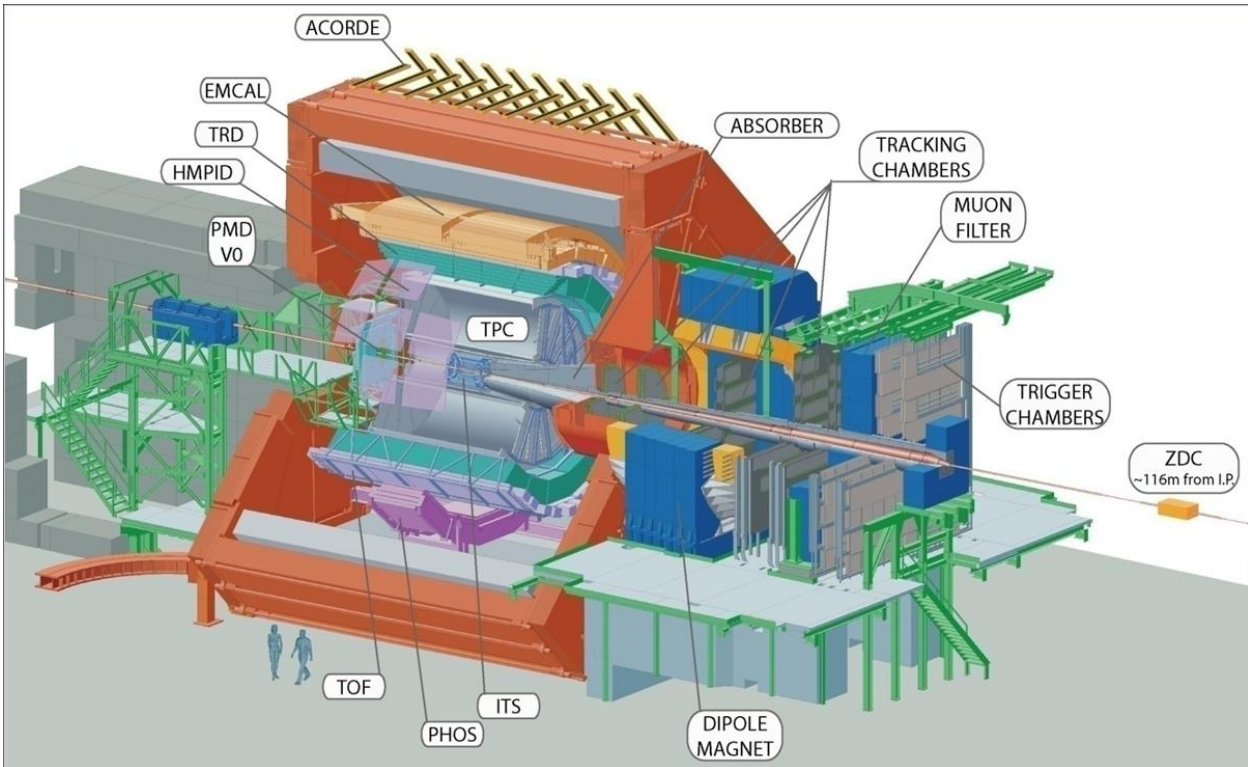


Figure 3.2: The ALICE Detector at CERN[16].

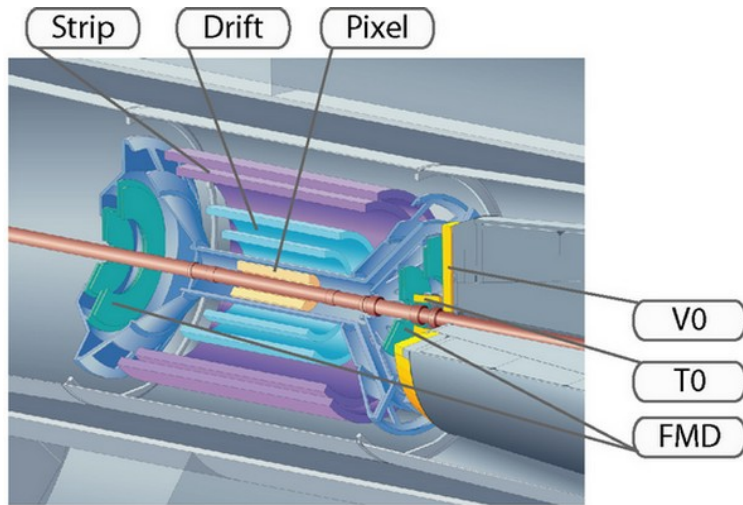


Figure 3.3: ALICE tracker, multiplicity, timing, and vertex detectors located near the interaction point[16].

VZERO

The VZERO (V0)[78] detector is a double layer scintillator array and similar to the T0 is asymmetrically placed at a distance of 86 cm (V0A) and 329 cm (V0C) away from the primary IP. It provides the ‘minimum bias’ (Min Bias)¹ trigger information for events and centrality information during the heavy-ion run. Centrality² is determined by measuring the multiplicity amplitude from the V0 and fitting these results to a Glauber³ distribution. The V0 is also capable of precision measurements of the target luminosity in the ALICE detector.

Inner Tracking System

The Inner Tracking System (ITS)[81] is six layers of solid state silicon detectors. Closest to the beam line are two layers of Silicon Pixel Detectors. The next two layers are Silicon Drift Detectors and furthest from the beam line are two layers of Silicon Strip Detectors. The main purpose of the ITS is to perform momentum measurements, PID, and vertex reconstruction of charged tracks. PID⁴ is performed by measuring the ionization energy, $\frac{dE}{dx}$, of charged particles as they traverse the detector[82]. The ITS has a spatial resolution of $100 \mu m$. This allows for measurements of short lived hadrons by reconstructing secondary vertices, which is useful in measuring hadrons containing heavy quarks, bottom and charm.

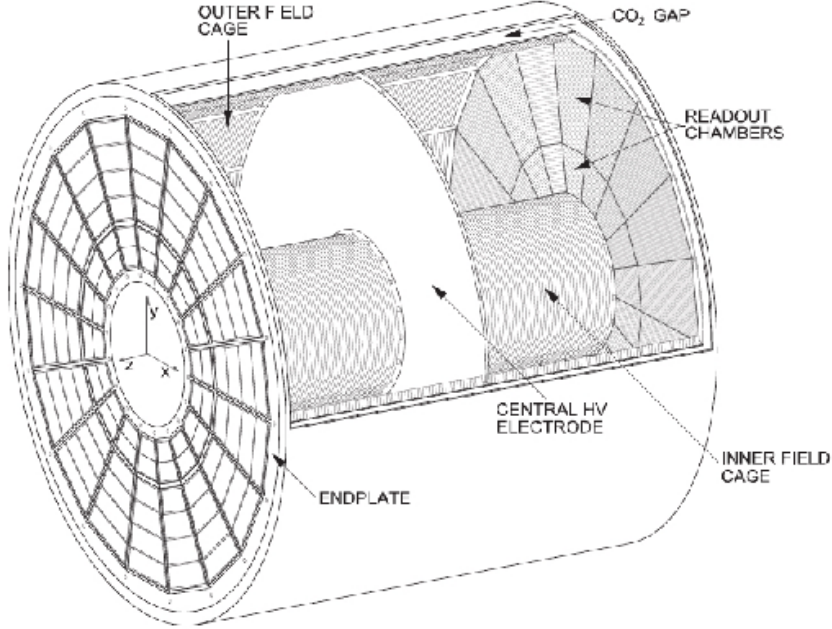


Figure 3.4: The ALICE Time Projection Chamber[17].

Time Projection Chamber

The Time Projection Chamber (TPC)[17] is a gaseous charged particle tracker and the largest of its kind in the world. The TPC has full azimuthal coverage, a pseudorapidity acceptance of $|\eta| \leq 0.7$, and a volume of 93 m^3 . Figure 3.4 shows a schematic of the TPC. As charged particles traverse the drift volume of the TPC, they ionize the gas inside⁵. A central cathode in the TPC with a voltage of 100 kV induces a uniform electric field of 400 V/m along the beam axis throughout the drift volume. Ionized electrons will drift down to the cylindrical endcaps of the TPC where the read-out chambers (ROC) are located. There are 18 ROCs

¹A Min Bias event is unsurprisingly defined as an event with the least amount of bias possible. Events recorded with a Min Bias trigger attempt to not artificially prefer either diffractive or non-diffractive processes over one another[79].

²Centrality (c) is an estimation of the impact parameter (b) between the two colliding nuclei. It is proportional to the cross-section and is given as $c = \frac{1}{\sigma_{inel}} \int_0^b db \frac{d\sigma}{db}$

³The Glauber model treats the nucleons composing a nucleus as hard shells, more can be found here [80].

⁴See Appendix A

⁵The TPC has operated with $Ne - CO_2$ (90-10) and $Ar - CO_2$ (90-10) gas mixtures in the past

on each side of the TPC which are further broken into an Inner Read Out Chamber (IROC) and an Outer Read Out Chamber (OROC).

The TPC Readout

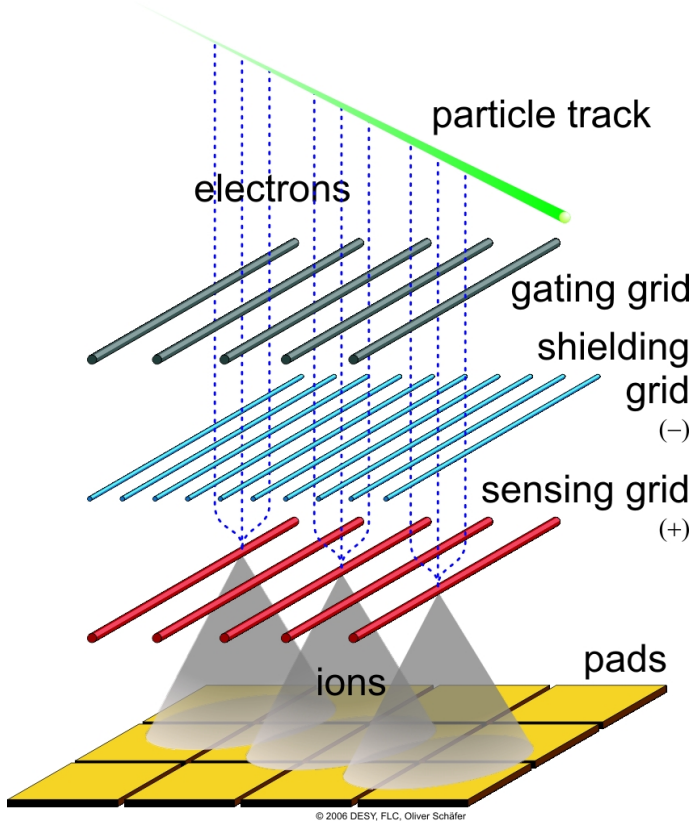


Figure 3.5: The TPC readout region[18].

The TPC incorporates a Multi-Wire Proportional Chamber (MWPC) design for amplification and copper pads for readout⁶. Ionized electrons created from charged particles take approximately $100 \mu\text{s}$ to move from the drift volume to the readout region. Once these electrons enter the readout region, they will undergo an amplification process with the MWPC, seen as the sensing grid wires in Figure 3.5. This amplification process will turn the

⁶There are 72 MWPCs and 500K copper pads in the ALICE TPC

few dozen ionized electrons generated from a charged particle into thousands of amplified electrons that are sensed by the cooper pads and read from the front-end electronics(FEE).

Amplification using MWPCs has the disadvantage of creating thousands of ions known as ‘backflow ions’ that can move back into the drift volume of the TPC. The presence of backflow ions in the drift volume of the TPC will cause distortions in the uniform electric field of the TPC. These distortions are known as ‘space-charge’ distortions and will compromise the physics performance of the TPC. In order to minimize the space-charge distortions, the TPC incorporates a gating grid[83]. Once an event is detected in the readout electronics of the TPC, a high voltage is induced on the gating grid. This will capture any backflow ions moving from the amplification region to the drift volume. When engaged, the gating grid introduces a dead time as any ionization electrons from new events occurring in ALICE will also get captured. The current configuration of the gating grid is designed to engage for 300 μs after an event is first detected. This has been shown to absorb approximately 99% of the backflow ions created while preserving the TPC physics performance. The dead time due to the gating grid along with the drift time for charged particles in the TPC limits the readout to 3.5 kHz. Upgrading the triggered operation of the current TPC to a continuous readout for the Hi-Lumi upgrade of the LHC will be discussed in detail in Chapter 4.

TPC Performance

In order to reconstruct the trajectory of a particle, an iterative process known as a Kalman filter approach is used. The x, y coordinates, which are perpendicular to the beamline, are determined via the signal induced on the copper pads. The z component, which is parallel to the beamline, is reconstructed using the timing information from the T0.

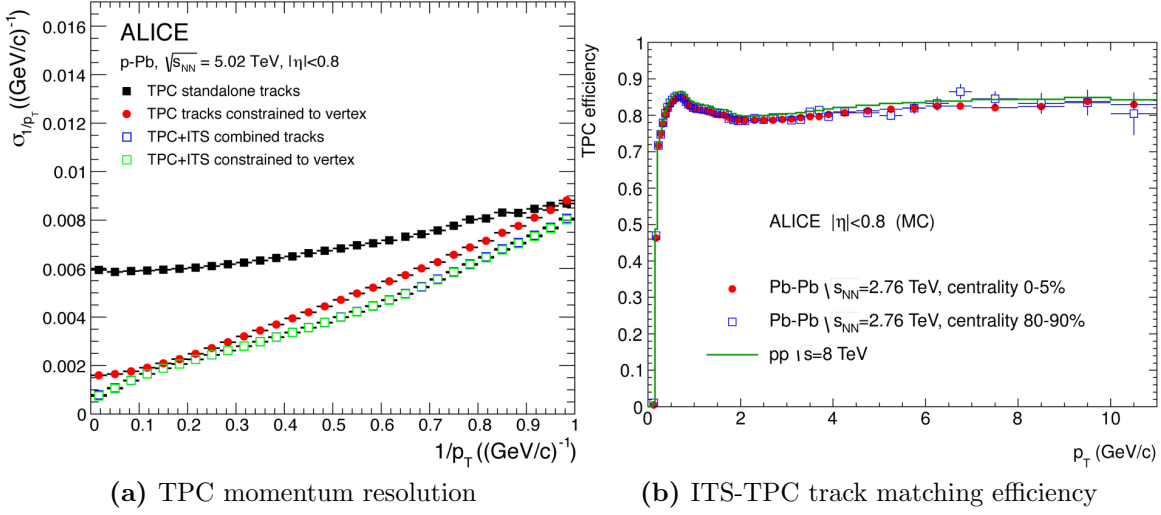


Figure 3.6: TPC momentum and tracking resolution[19].

The TPC has excellent momentum resolution between 150 MeV/ c to 100 GeV/ c [84].

Figure 3.6a shows the inverse momentum resolution as being below 5% in black. The inverse momentum resolution was further improved to below 0.5% over the full kinematic range by matching TPC tracks to ITS tracks and constraining those tracks to originating from the primary vertex region, red and green respectively. The total efficiency between ITS tracks to TPC tracks is stable at about 80%, as seen in Figure 3.6b.

Electromagnetic Calorimeter

The Electromagnetic Calorimeter (EMCal)[85] is a lead based sampling calorimeter located at a radius of 4.5 meters from the beam pipe. It covers a pseudorapidity of $|\eta| \leq 0.7$ and has azimuthal coverage of $\Delta\phi = 107 \text{ deg}$.

Figure 3.7 shows the layout of the EMCal. The smallest element of the EMCal is the ‘tower’⁷. The tower serves as the readout and is made up of several layers of alternating scintillator and Pb-absorber. Particles that interact via the electromagnetic force initiate a

⁷There are 12K towers in the EMCal

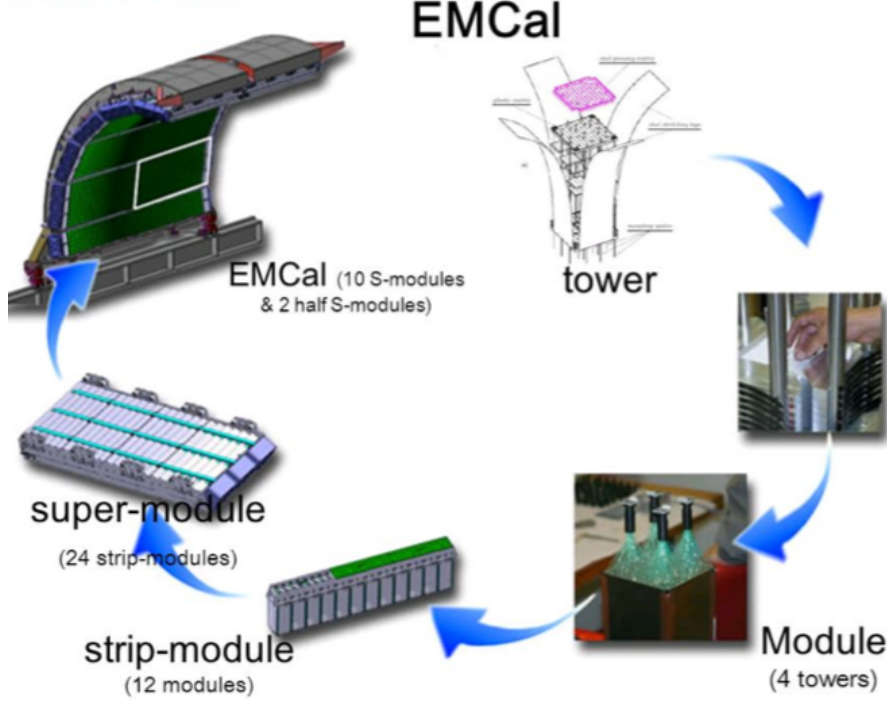


Figure 3.7: ALICE EMCal along with super modules, tower strips, and towers[20].

shower in the absorber material in the tower. This electromagnetic shower induces light in the scintillator to accumulate in the avalanche photodiodes in proportion to the particle's energy. A ‘module’ is an array of four towers that share readout electronics. Twelve modules are placed in a single strip that provides support to the structure. The largest component of the EMCal is the super-module, consisting of 1,100 towers, which serves as the mounting structure to the ALICE detector. The super-modules span a 20 degree angle in azimuth and ALICE currently has 10 full sized super-modlues and two 1/3 size super modules. A second calorimeter was installed in 2015, the Dijet Calorimeter(DCAL), and allows for back-to-back jet measurements.

EMCal Performance

As particles enter the EMCal they initiate an electromagnetic shower. The shower of electromagnetic particles spans several neighboring towers, these towers are grouped together into ‘clusters’ and the Analog-To-Digital Conversion signal from the clusters corresponds to the energy deposited by the particle. The EMCal was designed so that photons and electrons will fully shower inside of the tower region and thus fully deposit their energy. Hadrons on the other hand will usually punch through the EMCal and only deposit a small fraction of their energy.

PID can be performed using the EMCal via track-cluster matching from the TPC. TPC tracks are geometrically matched to the centroid of a cluster and if no track is matched, the cluster originated from a photon. If a track is matched, then the ratio of E/P, the energy of a matched cluster to the momentum of a TPC track, can be used to separate electrons from hadrons.

The energy resolution of the EMCal follows the form seen in Equation 3.1

$$\frac{\sigma}{E} = \sqrt{A^2 + \frac{B^2}{E} + \frac{C^2}{E^2}} \quad (3.1)$$

where E is the cluster energy, A characterizes stochastic fluctuations such as photon collection efficiency, B is a function of the systematic effects such as detector non-uniformity, and C is a function of the noise in the Front-End Electronics (FEE).

As seen in Figure 3.8, excellent agreement exists between the measured performance of the EMCal compared to simulations in a kinematic range between 10 GeV - 100 GeV and the resolution improves as the particle energy increases. The stochastic term, A, is the largest

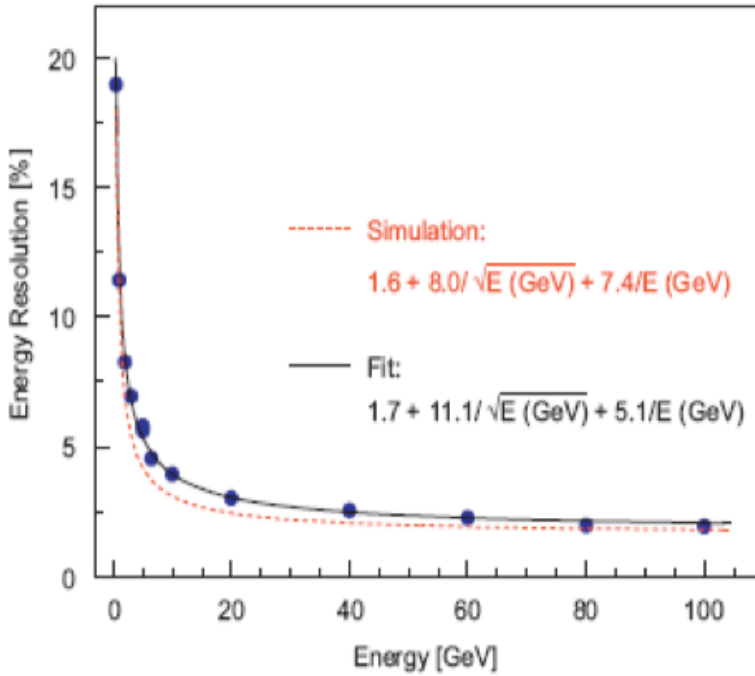


Figure 3.8: Energy resolution in the EMCal measured in a 2007 test beam at CERN (blue) compared to GEANT3 simulations of the EMCal (orange), fits for the parameters A, B, and C are also shown[21].

source of uncertainty in the energy resolution in the EMCal. Unlike the TPC, the resolution improves at high- p_t making the EMCal ideal for measuring high energy particles and jets.

EMCal Trigger

Due to the high luminosity in the LHC, only a small fraction of events may be recorded to disk for later analysis. ALICE employs a variety of triggers to record events that have the highest value for performing quality physics analysis. The EMCal can trigger on events in order to increase the effective sample size for high- p_T jets, photons, and electrons. The two main triggers[86][87] for the EMCal are a jet trigger and a gamma trigger. The gamma trigger is comprised of a 4x4 patch of EMCal towers, while the jet trigger is a 16x16 patch of towers. Once the gamma trigger has surpassed a minimum energy threshold of 5 GeV[88] the

event is tagged as a gamma event and the patch location is recorded. EMCAL jet triggered events have an energy threshold of 20 GeV and are similarly tagged and recorded. The 5 GeV and 20 GeV thresholds used to fire the EMCAL triggers are not fixed and the values quoted are specific to the 2012 8 TeV data set.

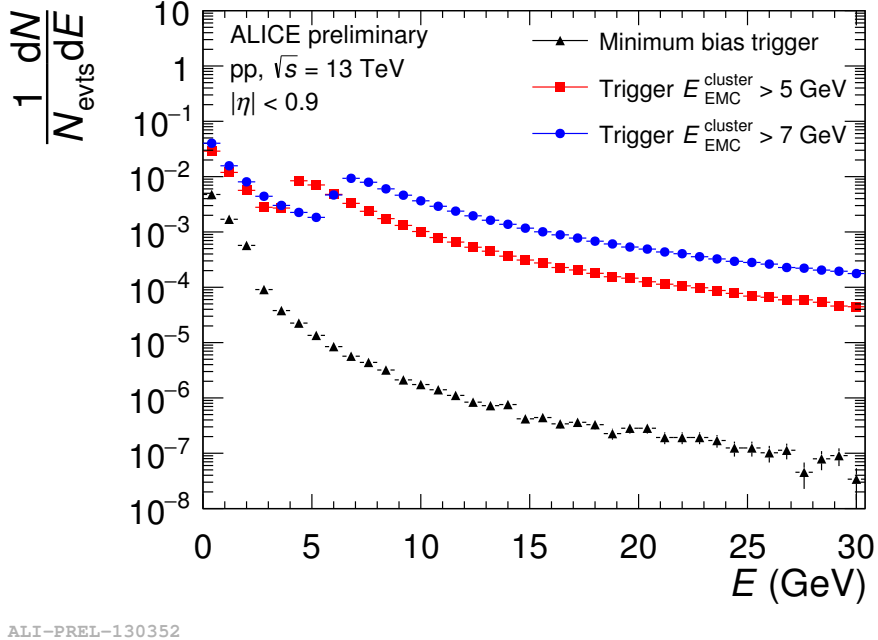


Figure 3.9: Cluster Spectra from the ALICE EMCAL. MinBias is shown in black while the red and blue points show the spectra using the gamma trigger at two energy thresholds[22].

Figure 3.9 shows the spectra from clusters measured in the EMCAL using MinBias data in black and the gamma trigger from the EMCAL set to two thresholds, 5 GeV and 7 GeV. Recording the events that satisfy the EMCAL triggers introduces a bias towards high- p_T processes. By using events that had an EMCAL trigger, we can extend the kinematic range of an inclusive jet measurement, as seen in Figure 3.9. In order to account for this bias it is necessary to calculate a trigger efficiency by comparing spectra from inclusive jets recorded using the MinBias trigger to the spectra generated from the EMCAL triggers in the 8 TeV data set. The calculation of the trigger efficiency will be discussed in depth in Chapter ??.

Chapter 4

The ALICE TPC Upgrade

From 2014 until 2018, I worked on the upgrade of the TPC to a continuous readout. This included working on a test beam in 2014 for a prototype Read-Out Chamber (ROC) using Micropattern Gaseous Detectors (MPGD) over the current Multi-Wire Proportional Chamber (MWPC) design. Once a final design for the new ROCs was chosen the production of the new Inner Read-Out Chambers (IROCs) using a stack of four Gaseous Electron Multiplier (GEM) foils took place at the University of Tennessee. During this period I assembled 49 new IROCs. In 2018, I traveled to Yale University and CERN to help with quality assurance of the IROCs built at Tennessee.

4.1 Physics Motivation

As of the end of 2018, the LHC has been in the second long shutdown (LS2) and upgrading to the High Luminosity LHC (Hi-Lumi LHC)^[89] which was briefly mentioned in Section 3.1. The goal of the LHC upgrade is to move into an era of high precision measurements of rare

QCD processes and increase the production of soft probes. Once the upgrade is complete the expected event rate in ALICE will be 50 kHz in MinBias PbPb collisions. This will lead to a factor of x100 increase in MinBias data and a factor of x10 increase in high- p_T triggered data recorded by ALICE.

The ALICE experiment has focused on probing the thermodynamic properties of the QGP in the past. The increase in event rate expected from the Hi-Lumi LHC will open new ways to probe the QGP including[23]:

- Increasing the production of jets and allowing separation of jet measurements based on the flavor of the initial parton.
- Studying the production mechanisms of light-nuclei, antihyper-nuclei, and other exotic hadrons.
- Probing the initial state of the QGP by measuring low-mass dileptons that originate from the earliest stages of a heavy-ion collision.
- Increasing the yields of heavy-flavor mesons reconstructed via secondary-vertices.

In order to do this ALICE will implement a number of upgrades [90] during the shutdown that include:

- Replacing the V0 and T0 detectors with a combined detector, called the Forward Interaction Trigger (FIT)[91].
- Improving the ITS and Muon Tracker spatial resolution by using Monolithic Active Pixel Sensors (MAPS)[92][93].

- Removing the 400 nanosecond dead time associated with the TPC and upgrading the FEE cards to handle the increase in data bandwidth[23].
- Implementing new Online/Offline (O^2) data processing architecture[94].

Leptons weakly couple to the QGP[95] and by studying these the initial states in heavy ion collisions may be probed[96]. Figure 4.1 on the left shows a simulation of the mass spectra for dileptons between 0 GeV/c - 1 GeV/c using the current ALICE central detectors with tight kinematic cuts. The yields that are quantifiable do not allow for the separation of leptons created via different processes in the QGP. After the increase in event rate and the upgraded ITS with improved tracking capabilities, measuring the low-mass dileptons that interacted with the QGP will be possible as shown on the right of Figure 4.1.

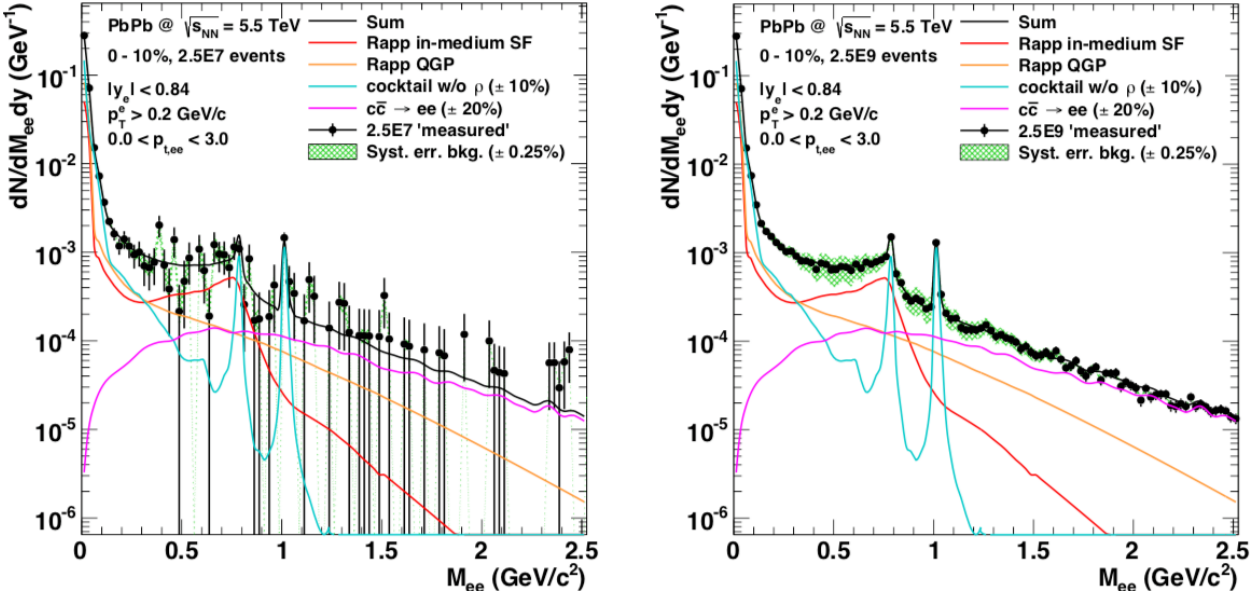


Figure 4.1: Simulation of the invariant mass spectra for dileptons in a typical heavy-ion run with current ALICE performance (left) and after upgrade of ALICE for Run-3 (right) in PbPb at $\sqrt{s_{NN}} = 5.5 \text{ TeV}$. The dilepton yields originating from the QGP are shown (red and orange), along with background contributions from light-hadrons (blue), and charm (magenta)[23].

The TPC used in the ALICE experiment along with the readout was discussed in Section 3.2. The ALICE collaboration first proposed an upgrade of the TPC in 2012 with a Letter of Intent (LoI)[23]. A Technical Design Report (TDR)[27] was published in 2013 with an initial design overview. An addendum to the TDR[28] was published in 2015 after the performance of prototype ROCs was measured on a test beam at CERN in 2014. The overall goals of the TPC upgrade are to continuously readout events in the high luminosity environment expected after LS2, to minimize the accumulation of space-charge distortions in the drift field, and to maintain the PID and tracking performance of the current TPC.

4.2 Gaseous Electron Multiplier Foils

Gaseous Electron Multiplier (GEM) Foils were first proposed by CERN physicist Fabio Sauli in 1997[97]. GEMs belong to a new form of detector technology known as Micropattern Gaseous Detectors[98] that use microelectronic or chemical etching techniques to print a readout structure onto a material surface.

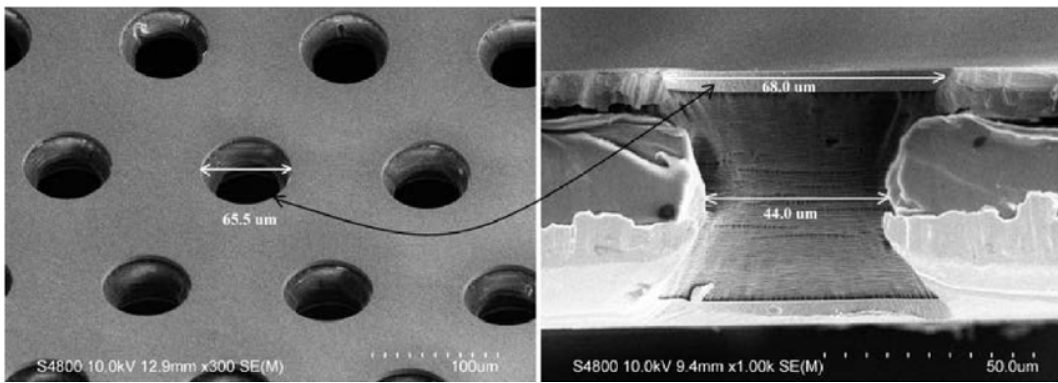


Figure 4.2: Scanning electron microscope image of a GEM foil from top (left) and profile (right)[24].

GEM foils are a Kapton sheet, typically $50 \mu\text{m}$ thick, with a thin copper coat on both sides of the surface. A weak acid and stencil are used to chemically etch holes throughout the foil. Typically, the holes are between $10 \mu\text{m} - 100 \mu\text{m}$ in diameter and between $100 \mu\text{m} - 300 \mu\text{m}$ in pitch, as seen in Figure 4.2. A few hundred volts is applied to each of the copper surfaces of the GEM foil causing a strong electric field to be induced in the GEM holes¹.

When an ionization electron from a charged track enters a GEM hole it will cause an avalanche of electrons and ions to be produced, amplifying the signal, to MWPCs. Due to the high voltage and strong electric fields around the GEM foil, any back flow ions created from the avalanche will get absorbed by the copper surfaces on the GEM foil, as seen in Figure 4.3.

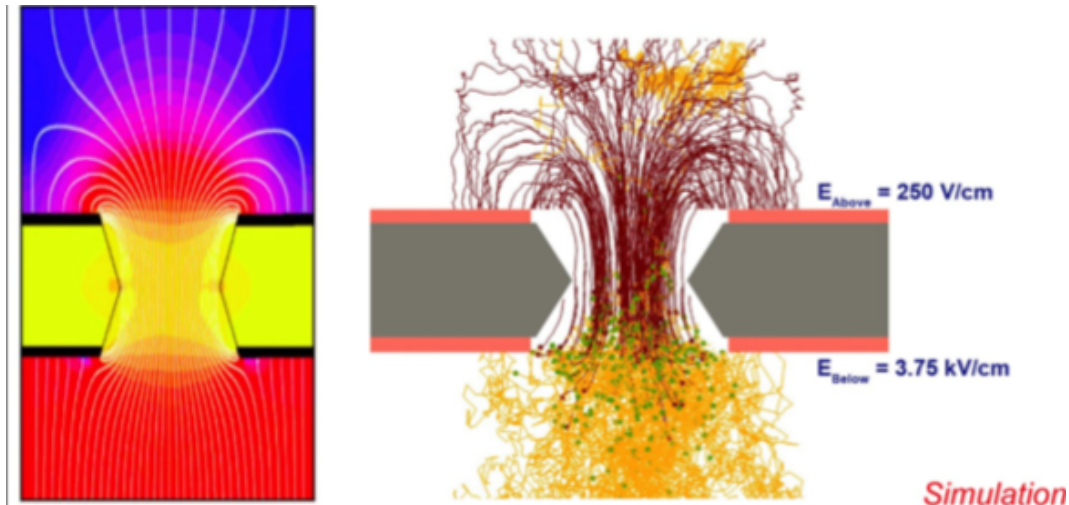


Figure 4.3: Profile of GEM with electric-field lines and gradients (left). Simulation of an ionization electron (yellow line) entering a GEM from a drift volume, amplification electrons (green dots, yellow lines) and back flow ions (red lines) are created (right)[25].

The configuration of the pitch and size of the holes on a GEM foil is directly correlated to the amplification properties and ability to capture back flow ions. GEMs with larger holes or shorter pitch between the holes will have more amplification but will also be more

¹The electric field is on the order of 10 kV/cm

ineffective at capturing ions. Likewise, GEMs with shorter holes or larger pitch will have better ion capturing abilities yet worse amplification properties. By stacking multiple GEMs on top of one another it is possible to maximize the amplification properties and minimize the backflow.

Creating GEMs with a uniform hole distribution and stacking them in a consistent manner in order to minimize the overlap of holes from one layer to another restricted them to small prototypes and impeded their use on large experiments. Around 2010 two methods were developed, the single-mask technique[99] and the NS2 assembly[100], which allowed for a systematic way of etching holes and stretching GEMs so they could be properly aligned. These methods allowed for GEMs to become a viable amplification device for large experiments. As of 2018 the TOTEM, COMPASS, ATLAS, and LHCb experiments have all incorporated GEMs in their trackers. Future colliders, such as the Electron-Ion Collider (EIC), plan on using them[101].

4.3 Research and Development

Initially, it was decided that the new ROCs would incorporate a stack of three GEMs with a hole geometry similar to the one incorporated on the LHCb experiment's[102] tracking detector. This was a starting point to bench mark performance for the ALICE TPC upgrade as well as an opportunity to use experts in GEM technology already present at CERN. The first phase of the R&D involved simulating the performance of the LHCb 3-GEM stack in the high event rate environment expected after the Hi-Lumi LHC upgrade using the software package Garfield++[103], which is a GEANT[104] add-on package built to simulate different

types of micro pattern gaseous detectors. It was quickly observed from the simulations that a 3-GEM stack would be insufficient in maintaining the performance needed for the TPC while minimizing the ion back flow. An additional layer of GEM was added to the 3-GEM stack in simulation and it was observed that this configuration would preserve the TPC performance.

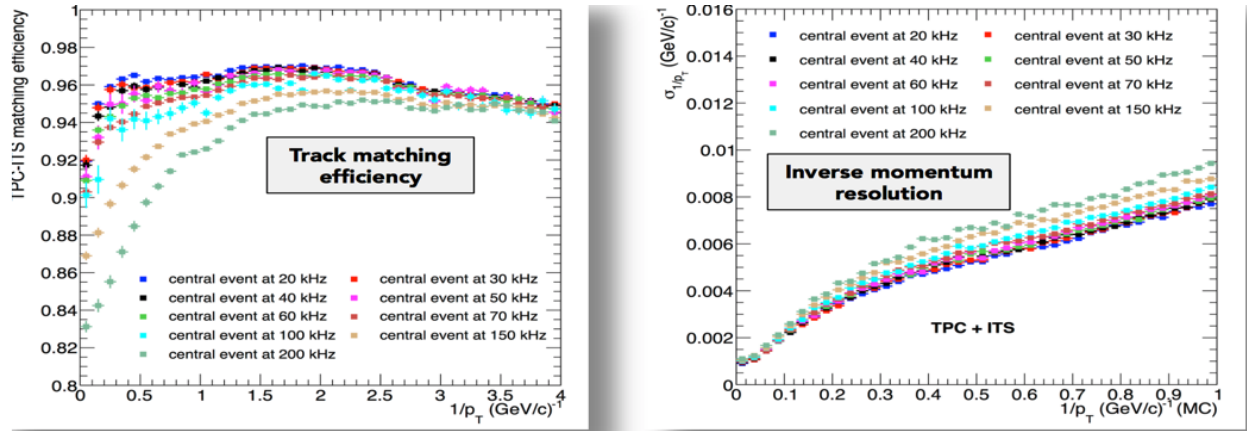


Figure 4.4: ITS-TPC matching (*left*) and inverse momentum resolution (*right*) for a 4-GEM stack simulated in Garfield++ [26].

Figure 4.4 shows simulations of the track matching efficiency from the ITS to the TPC and the inverse momentum resolution for a 4-GEM stack as a function of several collisions. The efficiency and resolution only start to diminish at an event rate above 100 kHz, which is double the expected rate after the LHC upgrade, and are well within the range of the current TPC, operating at 3.5 kHz.

The optimal hole configuration was also explored with simulations. Having a first and forth layer with a pitch of $140 \mu m$ and the second and third layer with a pitch of $280 \mu m$, allowed for the ROCs to maintain minimal ion back flow while amplifying the signal from tracks. Figure 4.5 shows the design of the ROCs with a 4-GEM stack. The copper pad plane is glued to a reinforced fiberglass sheet, known as the strongback, to add material strength.

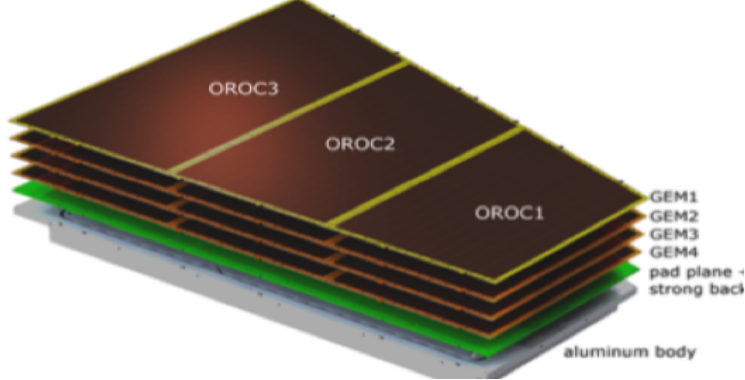


Figure 4.5: Final design of the upgraded readout chambers with a stack of 4 GEMS [27].

2014 Test Beam

During the 2014 test beam, I mounted the prototypes on the beam line, recorded data from the test beam, and monitored the performance in real time. To quantify the performance of the prototype, it is useful to define the effective gain (G_{eff}) and ionic back flow percentage (IBF%). The effective gain is a measure of the amplification properties and in a gaseous detector is defined as

$$G_{eff} = \frac{I_{anode}}{e N_{ion} R} \quad (4.1)$$

where e is the fundamental electric charge of an electron, I_{anode} is the current in the anode, N_{ion} is the number of captured ions, and R is the illumination rate from an active source.

The IBF% is defined as,

$$IBF\% = \frac{I_{cathode}}{I_{anode}} = \frac{1 + \epsilon}{G_{eff}} \quad (4.2)$$

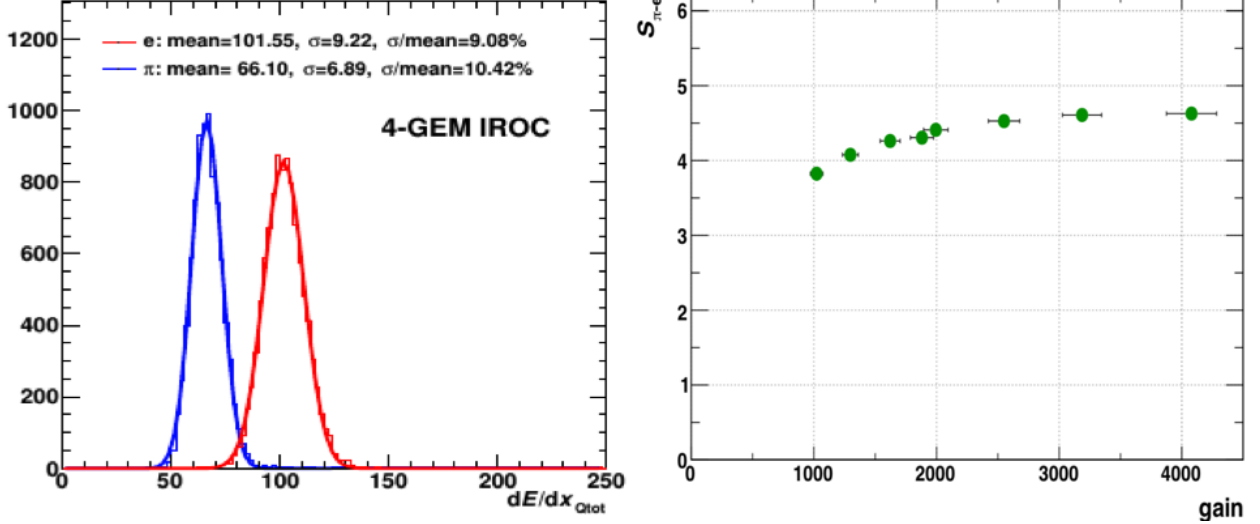


Figure 4.6: dE/dx resolution of the 4-GEM IROC prototype (*left*) and the separation power between electrons and pions as a function of gain (*right*) [28].

where $I_{cathode}/I_{anode}$ is the ratio of the currents measured in the cathode and anode portion of a readout as seen in Figure 3.5. The IBF% can also be defined in terms of the number of backflowing ions (ϵ) created at an effective gain (G_{eff}).

The test involved using the beam from both the SPS and PS² at the LHC cast onto an iron target. This iron target created secondary showers and tracks were measured by the prototype for both energy resolution and PID performance. The nominal TPC gas of $CO_2 - N_2$ (90-10) was used during the test beam.

Figure 4.6 shows the particle identification performance for separating electron and pion tracks created by the iron target. The separation power between the two Gaussian peaks increases until a gain of 2000 so this was chosen as the target effective gain for the new ROCs.

Figure 4.7 shows the energy resolution of the iron peak as a function of the relative voltages between GEM 2 (U_{GEM2}) and the ratio of voltages between GEM 3 (U_{GEM3}) and

²See Section 3.1.

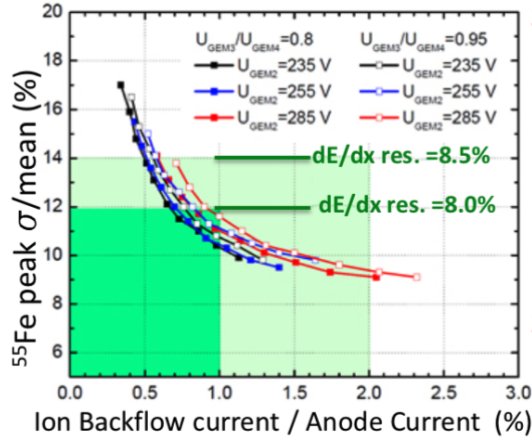


Figure 4.7: Energy resolution of the iron peak as measured from the prototype IROC with varying GEM voltages as a function of IBF%[28].

GEM 4 (U_{GEM4}). This shows that the IBF% remains below 1% at an energy resolution of approximately 10% which is consistent with the current TPC performance. The voltages were chosen such that GEM 1 and GEM2, which are closest to the drift volume, would focus mostly on capturing backflow ions, while GEM 3 and GEM 4, which are closest to the copper pad readout, would primarily perform the amplification as shown in Figure 4.8.

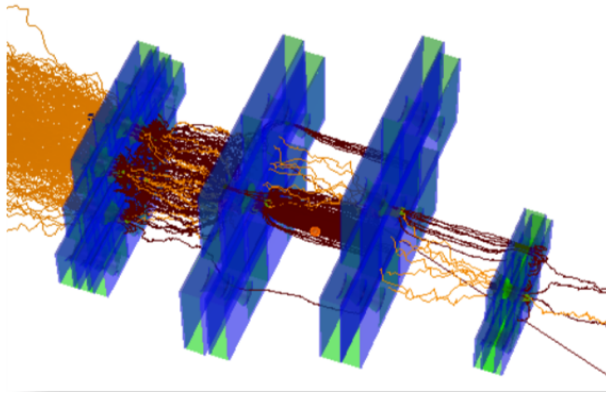


Figure 4.8: Simulation of the four GEM (blue) layers after test beam. The configuration is such that the two GEMs closest to the drift volume (right) absorb the amplification ions created by the two GEMs closest to the readout (left) [28].

4.4 Production of The Inner Readout Chambers

Once a final design was settled on from the simulation and prototype R&D, the project entered the production phase. A minimum of 36 new ROCs needed to be built with the 4-GEM stack to replace the old ROCs in the TPC, while 4 additional ROCs were constructed as spares. Due to the size and weight of the ROCs, production of the IROC took place in the United States and the OROC production mainly in Germany.

Figure 4.10 shows the production flow for the construction of the 4-GEM ROCs. After GEMs were received from the manufacturer, they went through a number of quality assurance tests before they were shipped to Wayne State University, where they were stretched and mounted for the IROC. The aluminum bodies were manufactured at the University of Texas Austin and shipped to Tennessee. At Tennessee we glued the pad plane, aluminum body and strong back together before it was shipped to Yale, where the chambers were fit with the GEMs from Wayne State. The production steps for the OROC mirror those performed by the IROC except that it was performed mainly by German institutes.

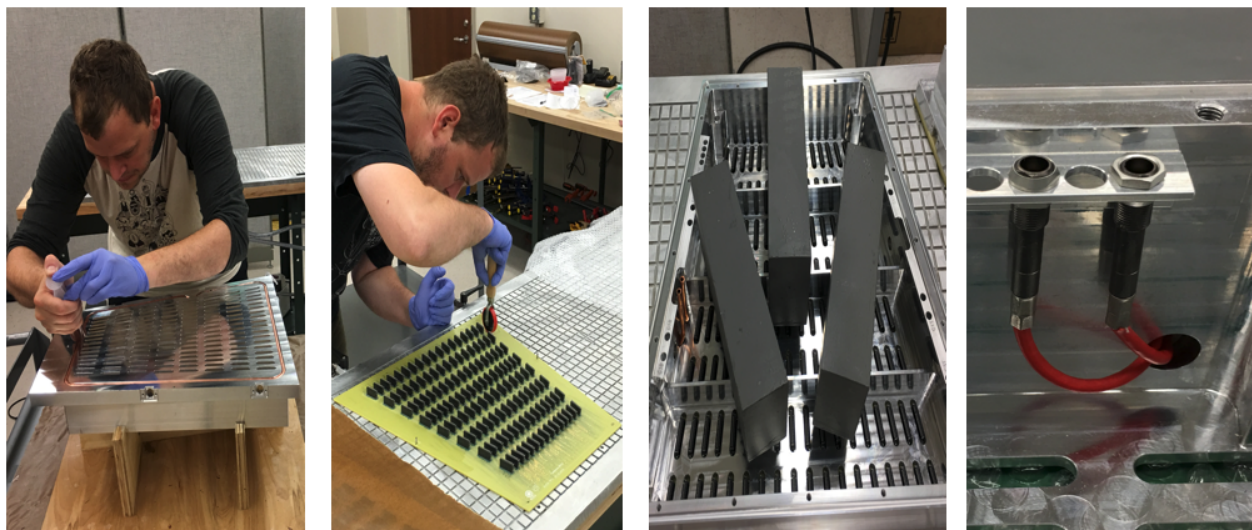


Figure 4.9: The author assembling an Inner Readout Chamber at Tennessee.



Figure 4.10: Production flow of the IROCs (red), OROCs (blue), and GEM foils (green)[26].

Figure 4.9 shows the procedure followed at Tennessee in order to build an IROC. Furthest on the left is a picture of a copper pipe glued into the aluminum body. This copper pipe is flushed with a coolant that maintains the temperature of the Front End Electronics (FEE) during data taking. The next two photos show the pad plane being mounted on a vacuum table while glue is applied to it and the aluminum body. Once all the components were placed, glued, and mounted on the table the IROC was loaded with lead bricks and allowed to cure for 24 hours. The right most picture shows the final step of the high-voltage (HV) feedthroughs mounted and glued for the GEM foils. Before a completed IROC left Tennessee we performed a gas tightness test that will be discussed more in the next section. Full production of the IROCs ended in November of 2018 with a total of 49 chambers being built at Tennessee. Eight surplus of chambers were built with excess materials to provide spares.

4.5 GEM and Chamber Quality Assurance

A stringent set of quality assurance (QA)[29][24] protocols were implemented to monitor any damage sustained during transport and to quickly identify any flaws in the production procedures. The QA can be broken into two major categories: QA performed on the GEM foils as received from the manufacturer and QA performed on complete/semi-complete chambers as they were going through the different production steps. I will discuss only the QA tasks that I was directly involved with.

GEM Quality Assurance

In order to evaluate the performance of a GEM foil, a spark test was performed on every foil. Sparks are caused by the discharge of the foil and may be due to the presence of dust on a foil, imperfections in the hole geometry, or a short between the two copper layers of the GEM. The final design of the GEM foil segmented each into twelve sectors with a $10 M\Omega$ bias resistor to ground across every segment. Any sparks from charge accumulation that occur on the GEM will only discharge a given segment and not the entire foil. Because of the delicate nature of the GEM foil, sparks have the potential to permanently damage a foil or seriously effect the performance of a ROC. Thus GEMs with a high spark rate should be excluded as soon as possible in the production flow.

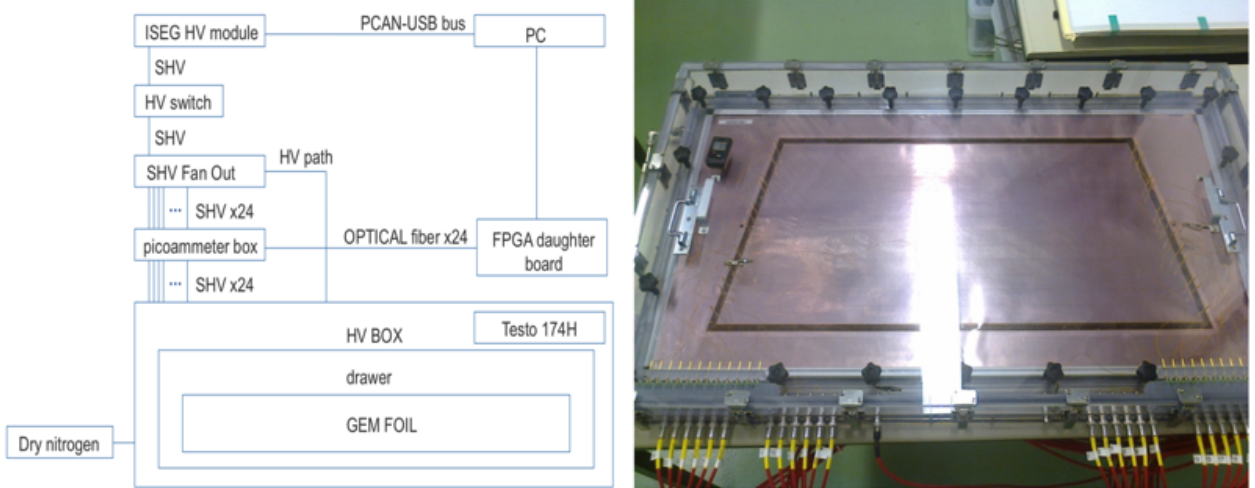


Figure 4.11: Schematic for the setup of the GEM foil spark test (*left*)^[29] and the GEM mounted in the HV gas box (*right*).

The GEM foil spark test involved mounting each foil in a high voltage box, which was flushed with N_2 until it reached a relative humidity of $\approx 10\%$. Once this humidity was reached 500 V is placed across each segment of the GEM and monitored with a LabView interface. A spark is defined as the LabView recording a current above 10 nA across the bias

resistor through any GEM segment and read by a multi-channel picoammeter. The criteria for a GEM to fail this QA was to have more than five sparks over a 20 minute recording window.

Chamber Quality Assurance

Most of the QA I helped with was on ROC chambers as they went through the production steps. Before completed IROC chambers were sent to Yale, I performed a gas leak test. The leak test consisted of mounting an individual chamber into an aluminum test vessel and flushing the inside of the vessel with N_2 gas. By using a flowmeter to measure the rate that N_2 gas entered the test vessel and an oxygen sensor to measure the amount of oxygen present at the output of the test vessel, we could infer the leak rate of each IROC chamber. Figure 4.12 shows a schematic of the setup on the left, and a typical output from the LabView interface on the right. By flowing at two different rates and measuring the oxygen content at each rate we could confirm the leak rate.

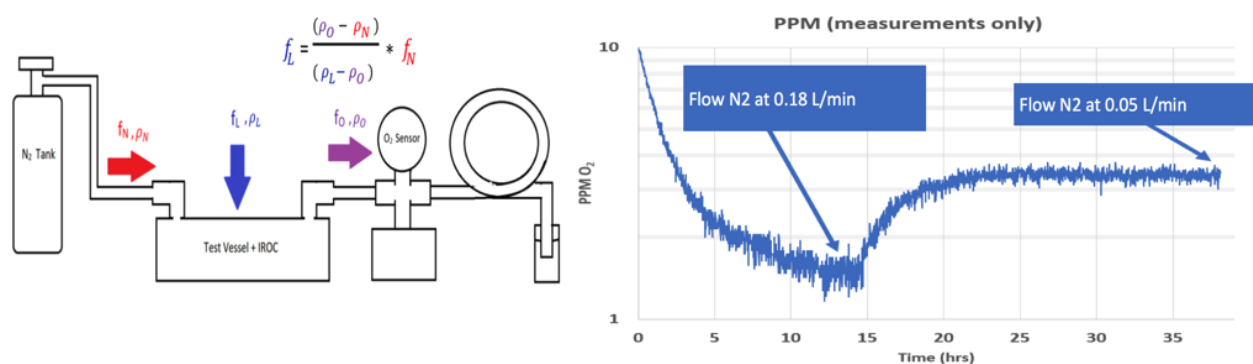


Figure 4.12: Schematic of the gas tightness testing setup at the University of Tennessee (*Courtesy of Joseph Rasson*).

The leak rate of a chamber, f_L , can be quantified as

$$f_L = \left(\frac{\rho_0 - \rho_N}{\rho_L - \rho_0} \right) f_N \quad (4.3)$$

where f_N is the flow rate of N_2 gas into the test vessel, ρ_L is the concentration of O_2 in the laboratory, ρ_N is the O_2 impurity present in the N_2 bottle, and ρ_0 is the O_2 reading from the LabView interface.

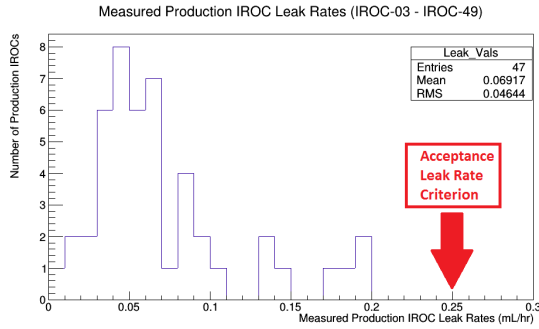


Figure 4.13: Leak rate of the 49 chambers built at Tennessee with the maximum failure rate at 0.25 ml/hr shown (*Courtesy of Charles Hughes*).

A maximum leak rate of 0.25 mL/hour was placed as the rejection criteria for a given chamber. If a chamber had a leak rate above this, the N_2 gas could get swapped out with a helium gas tank so we could identify the areas on the IROC causing the leak with a helium sniffer and patch the area with epoxy. Figure 4.13 shows the leak rate for all IROCs produced at Tennessee. Due to none of the chambers surpassing the leak threshold the helium sniffer was not used in the production of the IROCs.

Once an IROC chamber was fitted with the 4 GEM foils at Yale and sent to CERN, a spark test was performed over the entire chamber. The test involved placing each chamber next to the LHC beam line, flushing with the nominal TPC gas, placing the nominal voltage across each GEM, and monitoring the spark rate once a beam was present in the LHC. Figure

4.14 shows me installing the completed IROC chambers next to the LHC beam line in front of ALICE and the output from the spark monitor. The voltage across each chamber could be varied in real time in order to minimize sparking while maintaining the IROC performance, thus reducing the rate of degradation on a per chamber basis once installed in the TPC.

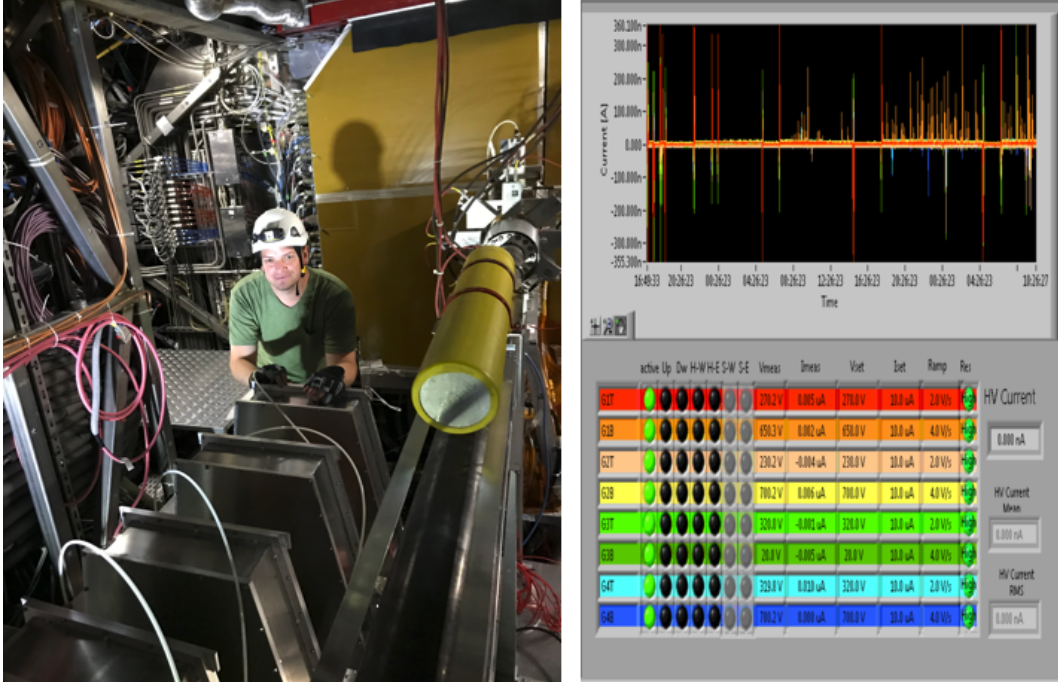


Figure 4.14: Testing for chamber sparking next to the LHC beam line (*left*) and real time output from the spark test during a live beam (*right*).

4.6 Outlook

As of 2019, the 49 IROCs assembled at Tennessee have been received at CERN. None of the built chambers have surpassed the gas leak test performed at CERN and so far only 4 chambers exhibit sparking rates above the failure threshold. Due to having 13 spare IROC chambers we evaluated all the chambers for the 36 best performing IROCs for the final installation. In May of 2019, the LHC beamline around ALICE was decommissioned and

the TPC was moved to a surface level clean room for the installation of the chambers. The new FEE electronics and the ROC chambers were installed in the TPC through the summer of 2019. Afterwards, there will be a 10 month commissioning with the TPC, during which the performance of the upgraded TPC will be evaluated with cosmic rays. By the end of 2020, the TPC should be back in the ALICE cavern and the beam line will have been re-installed. The Hi-Lumi run of the LHC is expected to start in March of 2021.

Chapter 5

8 TeV Data Selection

Beginning in March of 2012, the LHC began seven months of pp collisions at $\sqrt{s} = 8$ TeV.

During the seven months of taking data, the LHC spent 60% of the time in a state of stable beams as seen in Figure 5.1.

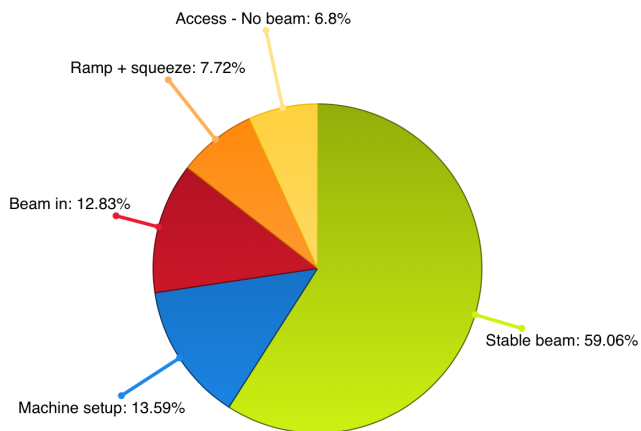


Figure 5.1: LHC state during the 8 TeV run.

The proton-proton Min Bias trigger is satisfied with at least one hit recorded in the SPD or V0. ALICE recorded almost 200 million events from this period that satisfied the

Min Bias trigger. ALICE also recorded almost 20 million high- p_T events triggered from the EMCAL. Any overview of the EMCAL trigger is given in Chapter 3.

ALICE is a state-of-the-art experiment with excellent tracking and particle identification capabilities, as discussed in Chapter 3. However, just like any real world experiment, it contains a number of inefficiencies and imperfections. This means that the data collected during the 8 TeV proton-proton collisions must be examined and any inaccuracies in the data must be removed before any conclusions may be reached. Data may be compromised at either the event-level, the experiment erroneously recorded something as an event, or at the constituent-level, one of the subdetectors mismeasured a feature of a particle. The remainder of this chapter focuses on the corrections and quality assurance performed on the 8 TeV data.

5.1 Min Bias and EMCAL Triggered Events

During the 8 TeV data collection period, approximately 180 million Min Bias events were recorded, as summarized in table 5.1. These events were separated into periods, which dictate the particular beam and detector configurations used. The 8 TeV data was divided into 7 periods, which were further parsed into runs. A period defines a particular configuration that the ALICE detector or LHC was in. Periods can differ from another in terms of types of particles colliding, collision energies, trigger conditions, etc. Runs represent an uninterrupted time of data acquisition with ALICE. A run can be as short as 5 minutes or as long as 10 hours. Runs were separated into ‘good’ runs when both the TPC and EMCAL were fully operational, ‘semi-good’ runs when a sector of the TPC was turned off but not around the

region below the EMCal, and ‘bad’ runs when a portion of the TPC was turned off directly below the EMCal or something else critically compromised the data. This analysis only incorporated good and semi-good runs.

Table 5.1: 2012 8 TeV data taking period.

Period	# of runs	# of Min Bias events
LHC12c	89	~ 24 M
LHC12d	140	~ 62 M
LHC12e	5	~ 2 M
LHC12f	56	~ 15 M
LHC12g	8	~ 0.4 M
LHC12h	159	~ 75 M
LHC12i	40	~ 3 M
Total	497	~ 181 M

Approximately 15% of the data sampled were unusable due to malfunctions in TPC chambers, EMCal super modules, or the electronics of the EMCal or TPC. The LHC12f and LHC12g EMCal triggered data is not used in this analysis due to a different trigger condition in the EMCal from the other periods. Besides the bad runs excluded from each of the periods due to QA, the rest of the 8 TeV data was used in this thesis. The LHC reported the integrated luminosity as $\mathcal{L}_{int} = 8.95 \text{ pb}^{-1}$ for the 8 TeV data[105].

Monte Carlo Anchored Data

Two Monte Carlo data sets which used a full GEANT simulation of the ALICE detector were produced by the ALICE collaboration and used for the Monte Carlo corrections in this analysis. The first used a Pythia particle-level simulation embedded in the ALICE GEANT simulation with about 17 million Min Bias generated events. The other uses a PHOjet embed

events consisting of about 21 million Min Bias triggered events. Both models used a Min Bias tuning and neither incorporated simulations of the EMCAL trigger for high- p_T events.

Event Selection Criteria

Due to inefficiencies in ALICE it will inevitable contain ‘bad’ events within a data set. We therefore set a quality assurance criteria by which an event is used in this analysis. For example, the LHC must be in a state of stable beams, cosmic rays must be excluded by only accepting tracks that originate from a vertex inside the detector, and the relevant detectors for a given analysis must be functioning as intended. Events were required to meet the following conditions:

- The event has a primary vertex reconstructed, this helps exclude cosmic ray events.
- The primary vertex occurs within a 10 cm window of the primary interaction point, this maintains our detector acceptance and ensures good particle reconstruction.
- The vertex resolution must be below 0.25 cm, this ensures that the vertex is real and not a misreconstruction.
- The event passes basic pile-up checks based on the V0 and T0 signals, this ensures that we dont have data from different collisons overlapping one another.

A summary of the rejection reasons for an event are shown in Figure 5.2. Most of the rejected events were excluded due to the event not satisfying the vertex requirements. The vertex rejection does not impose a bias on my final results because these events are low multiplicity and low momentum transfer which have a low probability for jet production.

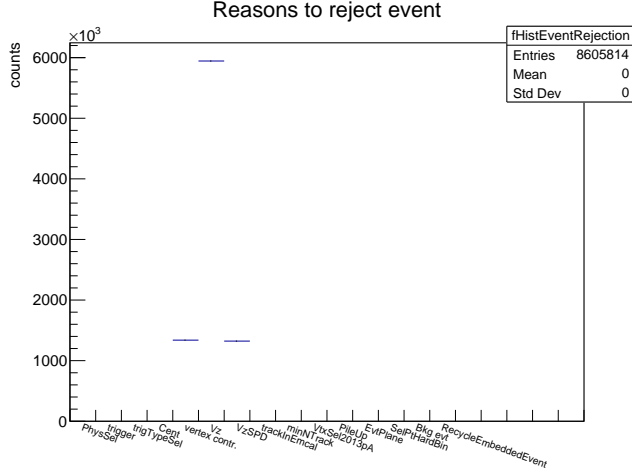


Figure 5.2: Min Bias event rejection summary.

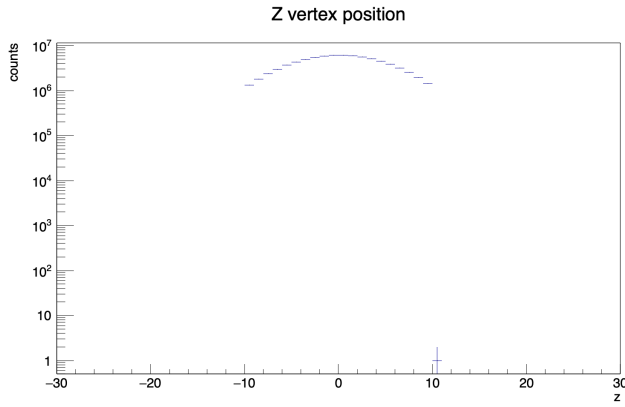


Figure 5.3: Vertex displacement from primary interaction point for accepted Min Bias events.

Figure 5.3 shows the reconstructed vertex for the accepted Min Bias events. We see that the vertex distribution peaks at the primary interaction point as expected.

In addition to the vertex requirements the 8 TeV data set was investigated for the presence of LED events. The EMCal uses a system of LEDs for calibrations. Previous ALICE data sets had events contaminated by the LED firing. The presence of LED events within the 8 TeV data was investigated by measuring the EMCal cell multiplicity per super-module for each event. No LED events were found within the 8 TeV data set. The EMCal triggered

data used similar event criteria to the Min Bias data and triggered most events were rejected due to the vertex requirements.

5.2 EMCal Clusters

Corrections were applied to cells including the removal of hot and dead towers (bad channels) based on the average occupancy and energy of the towers, calibrations to cell timing caused by the physical layout of the EMCal (such as differences in cabling length), and an energy calibration based on the π^0 mass. Figure 5.4 shows a bad channel map after removing the hot and dead towers from a typical run. The ϕ distribution is segmented into 5 parts representing the five super modules of the EMCal.

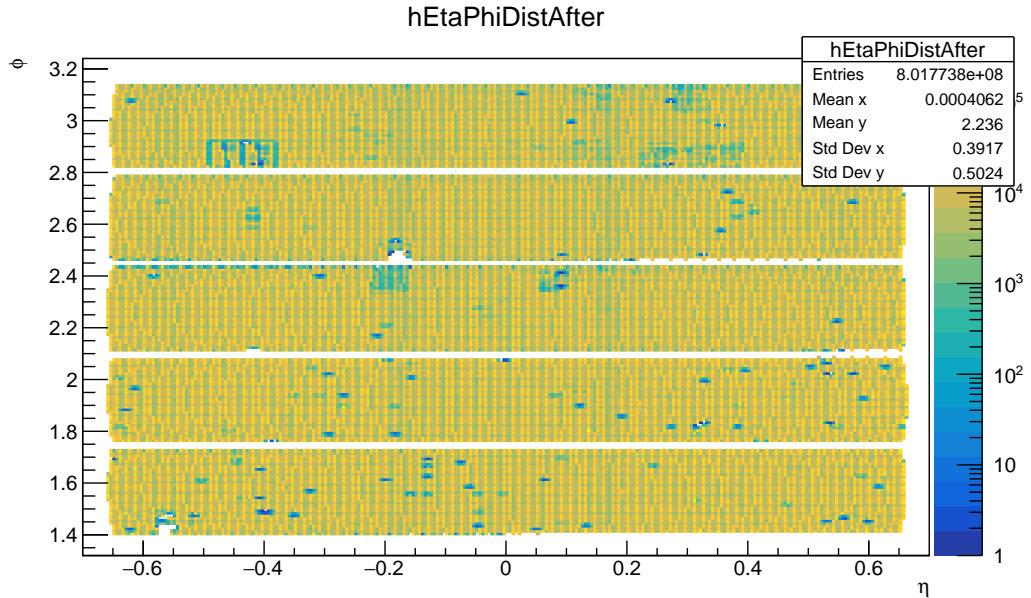


Figure 5.4: EMCal cell occupancy after bad channels removed.

After these corrections were applied, the towers were grouped together into clusters using a clustering algorithm. The algorithm finds any EMCal tower with minimum tower energy

of 300 MeV and uses this as a seed, after which all adjacent towers with a minimum energy, $E_{cell} \geq 100$ MeV, are iteratively added using a method similar to the k_T algorithm from Chapter 2. After this point the set of clusters for a given event have been reconstructed. The cluster energy is the sum of the seed tower and grouped neighbor tower energies. EMCal clusters are corrected for exotics. This correction was performed by cutting all clusters with a $F_{cross} \geq 0.97$, where

$$F_{cross} = 1 - \frac{E_{cross}}{E_{cell}}, \quad (5.1)$$

where E_{cross} is the sum of the four cells sharing a full edge with the leading cell and E_{cell} is the center pixels energy. The main source of exotic clusters in the EMCal is most often due to a hadron hitting the Avalanche Photodiode (APD) in a tower. This will concentrate the energy of the cluster into a single tower while the adjacent towers will contain only a small fraction of the cluster energy. The exotic clusters were removed before jet finding occurred as they are an artifact of the detector performance.

The EMCal is optimized to measure neutral particles, photons and neutral pions as they will fully shower inside of the sub-detector. Hadrons are detected by the EMCal, but will only shower a fraction of their intrinsic energy. A hadronic correction was performed in order to account for double counting as charged hadrons will deposit energy in both the TPC and EMCal. To identify charged hadrons, charged tracks from the outer layer of the TPC were propagated to the EMCal, by fitting the trajectory of the track to a curve, and fitting the tracks and clusters geometrically. Figure 5.5 shows the distance between the centroid of a cluster in the EMCal and the nearest track propagated from the TPC. Hadrons are identified

by requiring the matched distance to be, $\sqrt{\Delta\phi^2 + \Delta\eta^2} \leq 0.015$, which is within one EMCAL tower distance. A non-linear correction to the cluster energy is applied based on the 2010 test beam data to account for the non-uniform energy response.

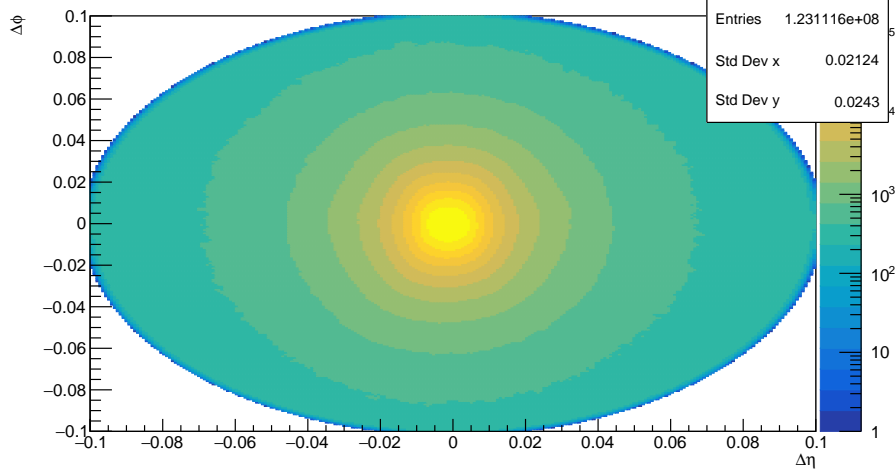


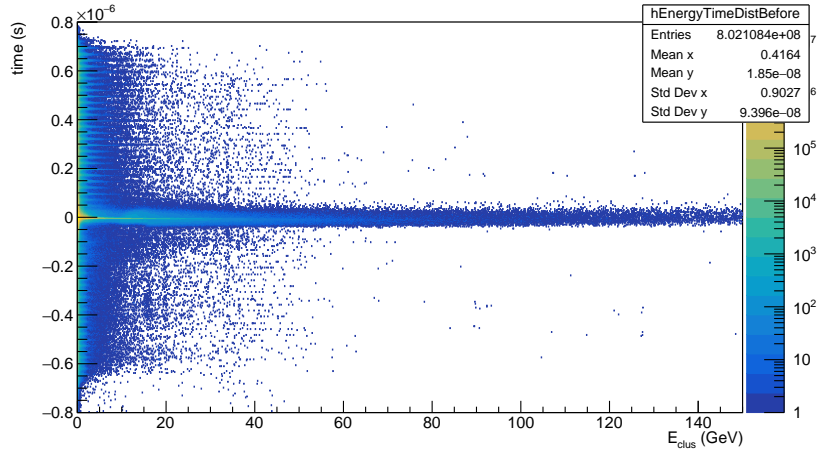
Figure 5.5: Matched track-cluster distance.

Corrections for the double counting from hadrons is based on correcting the EMCAL cluster energy by a weight function

$$E_{corr} = E_{clust} - f_{sub} \times \sum p, \quad (5.2)$$

where $\sum p$ is the magnitude of the 3-momentum of the hadron and $f_{sub} = 1$ is the nominal value for the weight. If $E_{corr} \leq 0$ the cluster was removed. This may be caused by cluster pile-up and only accounted for a small fraction of the clusters. In order for a cluster to be accepted $E_{corr} \geq 300$ MeV was required, because a minimum ionizing particle (MIP) will on average deposit 280 MeV in the EMCAL.

A final cut was performed on the cluster timing, obtained from the T0, the time of arrival for a particle is shown on the y-axis of Figure 5.6.



Cutting on the cluster time is done in order to readout only the particles created from an event and to limit the contamination due to slower particles from previous events. The main source of the slow moving particles are ‘slow’ neutrons and K_L^0 from the previous collision or detector noise, this analysis limited cluster time to $t_{clus} \in [-50 \text{ ns}, 100 \text{ ns}]$.

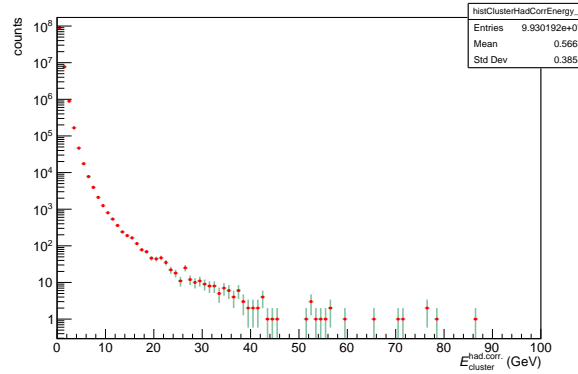


Figure 5.7 shows the final cluster energy distribution with all the cuts and corrections. The same cuts and corrections were applied to the EMCAL triggered data. Clusters with an energy greater than 300 MeV were used for the jet finding due to the uncertainty in the energy response of the EMCAL

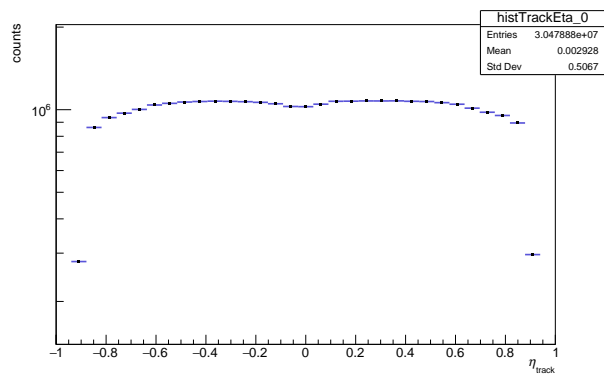
5.3 TPC Tracks

Tracks were reconstructed in the TPC using a Kalman filter which helps alleviate any corrections needed due to multiple scatterings, dead sectors, energy loss, etc. The Kalman filter used in ALICE reconstructs tracks using the following approach. First, the algorithm finds hits on the outer radius of the TPC where the track density is the lowest. For each of these track candidates the algorithm starts to reconstruct the track by adding hits from the TPC as it's traced inward from the TPC radius. Once all the hits are reconstructed into tracks on the inner radius of the TPC, ITS track reconstruction takes over and the track is traced back to the primary vertex as best as possible. If the track reconstruction was successful a second pass begins, this time starting from the primary vertex, moving through the ITS, and finishes at the outer wall of the TPC. Track candidates that are successfully reconstructed during both of the passes go through a third and final reconstruction starting from the outer wall of the TPC moving backwards towards the vertex region. Once the three passes are complete the track parameters are finalized and the tracks from the event are recorded. Tracks can have a number of inefficiencies and non-uniformities present in them. Using ‘hybrid’ tracks helps with non-uniformities and ensures that tracks have a uniform distribution in the detector. Hybrid tracks consist of two track sets, the first being

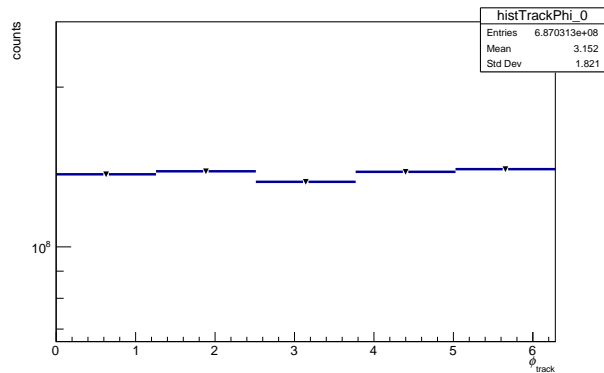
all tracks with at least one hit in the SPD (Global), and the second set being all tracks that can be constrained to the primary vertex (Complimentary). By using complimentary tracks for jet finding we ensured good p_T measurement because the track traversed a large portion of the TPC.

The reconstruction of a signal from the ITS and TPC form good tracks if the χ^2/NDF , chi-square per degrees of freedom, is required to be less than 4 in the TPC and χ^2 is required to be less than 36 in the ITS. For this analysis, the minimal $p_{T,track}$ was 150 MeV/c and the track was constrained to the acceptance: $-0.9 \leq \eta \leq 0.9$ and $0 \leq \phi \leq 2\pi$, shown in Figure 5.8. Tracks were further constrained by forcing them to have a distance of closest approach to the primary vertex of less than 2.5 cm in the plane transverse to the beam line and less than 3.0 cm along the beam axis. The spatial distributions of the hybrid tracks remain relatively flat as expected in the 8 TeV data set for good and semi-good runs.

An important parameter of the hybrid track is the track p_T resolution which determines how well the track momentum was measured. The quality of the jet p_T resolution was maintained by only accepting tracks into the jet finder with a resolution below 1% as seen in Figure 5.9, which was obtained by varying the parameters from the kalman fit. The accepted complimentary track p_T distribution may be seen in Figure 5.10. Tracks should travel in a smooth curve unless they decay in the detector. Tracks in the TPC may exhibit a kink due to the particle decays or misreconstructions. Tracks with a kink were excluded from this analysis. The track quality control used in this thesis followed previous ALICE jet results[107]. The cuts and quality control were used uniformly for tracks from Min Bias events and from the EMCal triggered data.



(a) Hybrid Track η



(b) Hybrid Track ϕ

Figure 5.8: Hybrid Track η and ϕ yields.

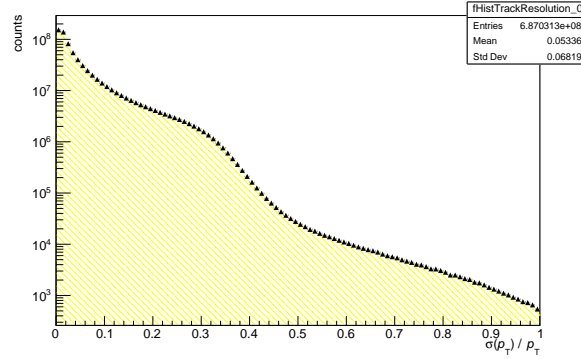


Figure 5.9: Accepted hybrid track resolution.

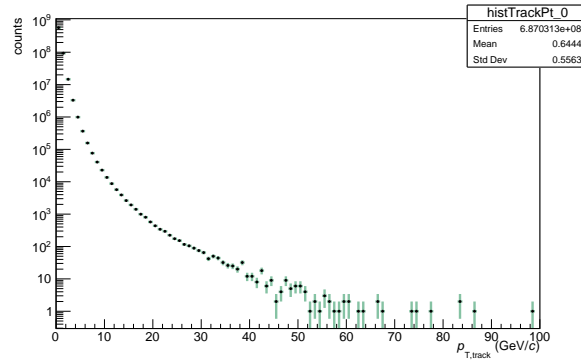


Figure 5.10: Accepted track p_T yield.

5.4 Raw Jet Reconstruction

Tracks and clusters that passed the QA requirements were used for anti- kt jet reconstruction to measure inclusive jets. A minimum threshold of 5 GeV was used to reconstruct a jet in this analysis because of ambiguities in the QCD definition jet below this range. This analysis used the p-scheme recombination method discussed in Chapter 2. No tracks above 100 GeV/c were used in the jet finding due to the tracking resolution, Figure 5.11 shows the distribution of the track momentum for a given jet momentum. In addition a cut was applied that a jet must be composed of at least two constituents, as shown in Figure 5.12.

The z for the leading track,

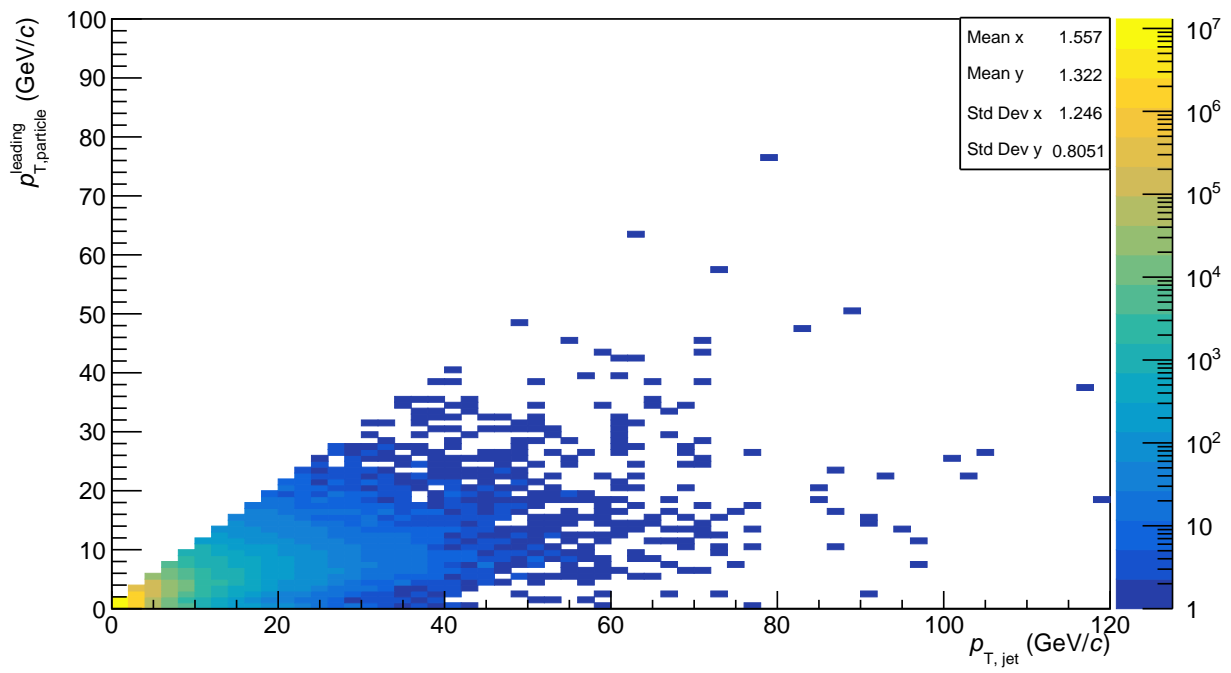


Figure 5.11: $R = 0.2$ leading track p_T per jet p_T .

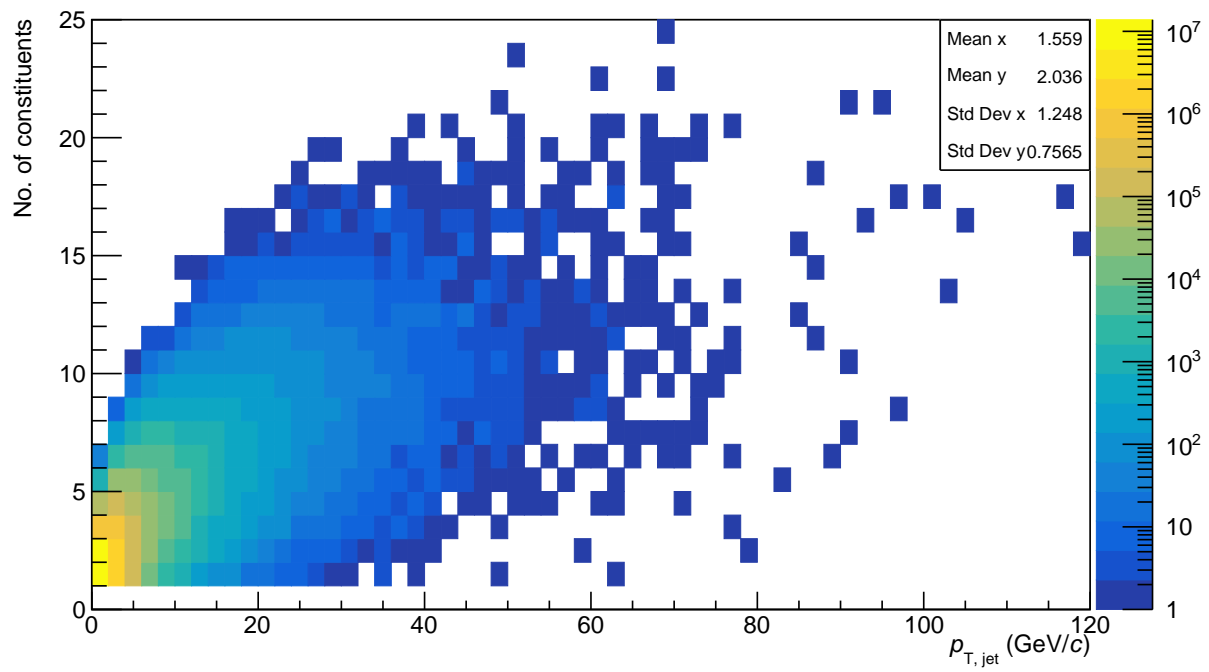


Figure 5.12: $R = 0.2$ number of constituents in a jet per jet p_T .

$$z_{leading} = \frac{p_{leading,proj}}{p_{jet}}, \quad (5.3)$$

may be artificially high due to misidentifying secondary decay particles as primary vertex tracks and assigning them a much larger p_T . Additionally, fake clusters, such as exotics, may skew the $z_{leading}$ quantity.

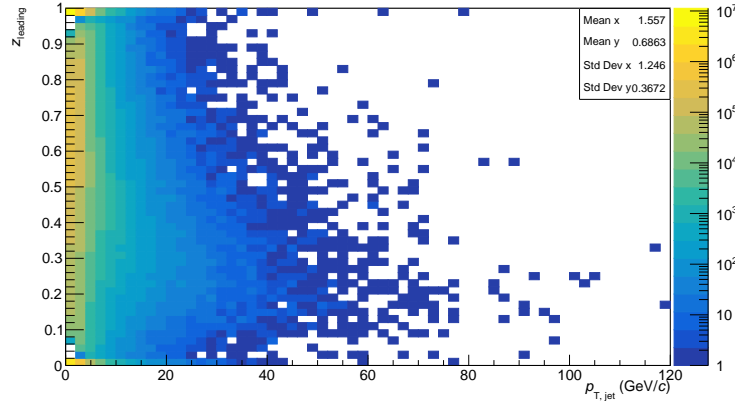


Figure 5.13: $R = 0.2$ $z_{leading}$ from the Min Bias data sample.

The $z_{leading}$ was investigated during this analysis. Figure 5.13 shows the $z_{leading}$ for a given jet p_T . We observed an excess of jets, especially at low jet p_T , of $z_{leading}$ values close to 1 or zero. Previous jet results from ALICE removed these jets with a cut on $z_{leading} \geq 0.03$ and $z_{leading} \leq 0.97$ in order to exclude tracks created from low energy daughter decays and noisy towers from the EMCAL. However, a $z_{leading} \sim 1$ corresponds to a jet dominated by a singular high- p_T particle. Although unlikely this is allowed by QCD and thus no $z_{leading}$ cut was implemented in this analysis. In between .03 and .97 we see the $z_{leading}$ is continuous and uniform as expected.

A jet area of, A_{jet} , cut was imposed on accepted jets.

$$A_{jet} \geq 0.6\pi R_{jet}^2 \quad (5.4)$$

The area is estimated in FastJet using ‘ghost’ particles. As jet reconstruction is being performed, these fake particles with infinitesimal p_T are placed randomly throughout the event. The number of ghost particles captured in a jet is proportional to the jet area, thus the precision of the jet area is sensitive to the reconstruction of soft particles. Jet area cuts are atypical in a proton-proton analysis, however one is implemented in this thesis so that the final jet cross-sections can serve as a baseline measurement for heavy-ion jet measurements.

Figure 5.14 shows the rejection reason for a jet from the 8 TeV data, the dominate reason for cutting a jet was due to the area criteria this cut skewed towards low- p_T jets. Jet area cuts are atypical in proton-proton measurements. Due to the high multiplicity environment present in heavy-ion collisions area cuts are much more common, by using an area cut the jet results presented in this thesis better serve as a baseline measurement for jet quenching.

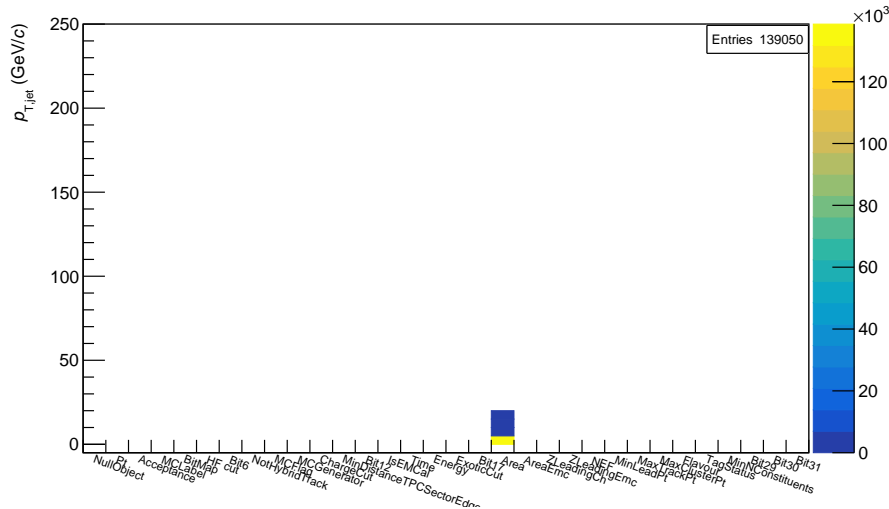


Figure 5.14: Jet rejection reason.

The Neutral Energy Fraction (NEF) is the total jet energy carried by the neutral components of the jet, i.e. EMCAL clusters. Figure 5.15 shows the NEF for $R = 0.2$ jets from the Min Bias sample.

The 8 TeV data was investigated and we observed an excess of jets at low- p_T with NEF values around zero or one, similar to what was seen with the $z_{leading}$ distribution. The cause for these excesses were explored in this analysis, but no hard source was identified and no cut to the NEF was used. Previous ALICE jet results cut the low and high range of the NEF, but from the QCD standpoint these jets are allowed. No NEF cut was implemented for this analysis.

The criteria and cuts discussed in this chapter were implemented for the $R = 0.3$ and $R = 0.4$ jet analysis along with jets found using the EMCAL triggered data.

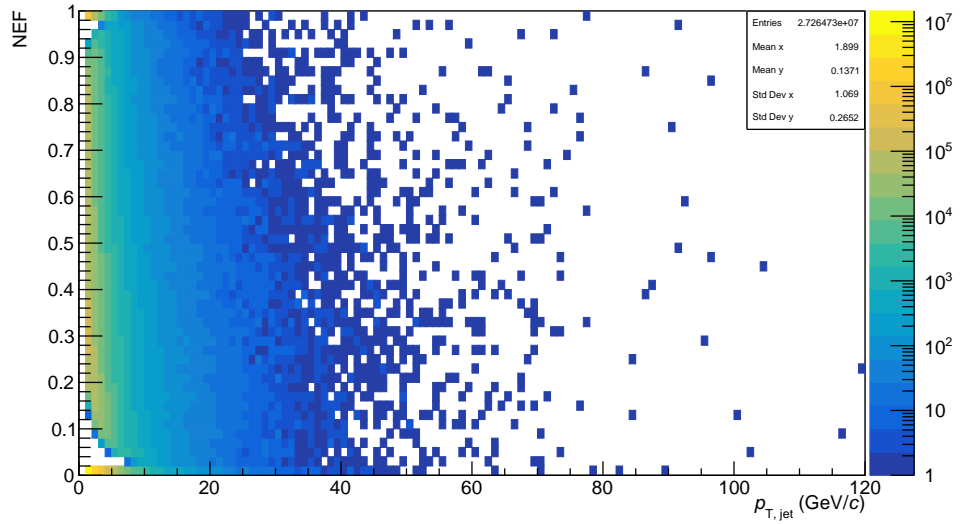


Figure 5.15: $R = 0.2$ NEF per jet P_T .

Chapter 6

Corrections and Systematic Uncertainties

This large amount of data collected for the 8 TeV data set offers a unique chance to explore jet cross-sections using high statistics. In order to measure the jet double differential cross-section, the following formula is used,

$$\frac{d^2\sigma^{jet}}{d\eta dp_T} = \frac{1}{\epsilon_{reco}} \frac{A_{trigger}}{\epsilon_{trigger}(p_T)} \times C_{MC} \times \frac{1}{A} \times \frac{1}{\mathcal{L}_{int}} \times \frac{dN_{jet}^2}{dp_T d\eta} \quad (6.1)$$

where,

- ϵ_{reco} is the efficiency for reconstructing the jet in the ALICE detector.
- $A_{trigger}$ is the acceptance for EMCal triggered events and $\epsilon_{trigger}(p_T)$ is the EMCal trigger efficiency. These factors correct for imperfections in the electronics of the EMCal and the overall factors are equal to one in Min Bias events.

- C_{MC} is a correction factor due to detector effects and it allows for comparisons between the ALICE experiment and other experiments or theoretical calculations. Unfolding is used to determine this factor.
- \mathcal{L}_{int} is the integrated luminosity during the period when the data was recorded.
- A is the geometrical detector acceptance.
- $\frac{dN_{jet}^2}{dp_T d\eta}$ is the inclusive jet momentum spectra.

By incorporating the additional terms in Equation 6.1 we can obtain a fully corrected inclusive jet cross-section that can be compared to theoretical calculations and other experiments. Further cuts for the geometric acceptance, corrections for detector effects, and efficiency calculations need to be accounted for to create a fully corrected jet result. This chapter will conclude with a presentation of the systematic errors that are reported with the final jet cross-sections

6.1 Raw Jet Spectra

This analysis measured inclusive jet results for radii between 0.1 and 0.5. However, jet results for radii $R = 0.2$ to $R = 0.4$ will be presented in the body of this chapter. Figures 6.1, 6.2, and 6.3 show the raw (uncorrected) p_T spectra for inclusive jets from both Min Bias and EMCAL triggered data. It is also evident from these figures that the EMCAL triggered data greatly extends the kinematic reach of the measured jet spectra, to about 200 GeV/c. The EMCAL data introduces a bias at low- p_T as seen in the different distribution shapes. The

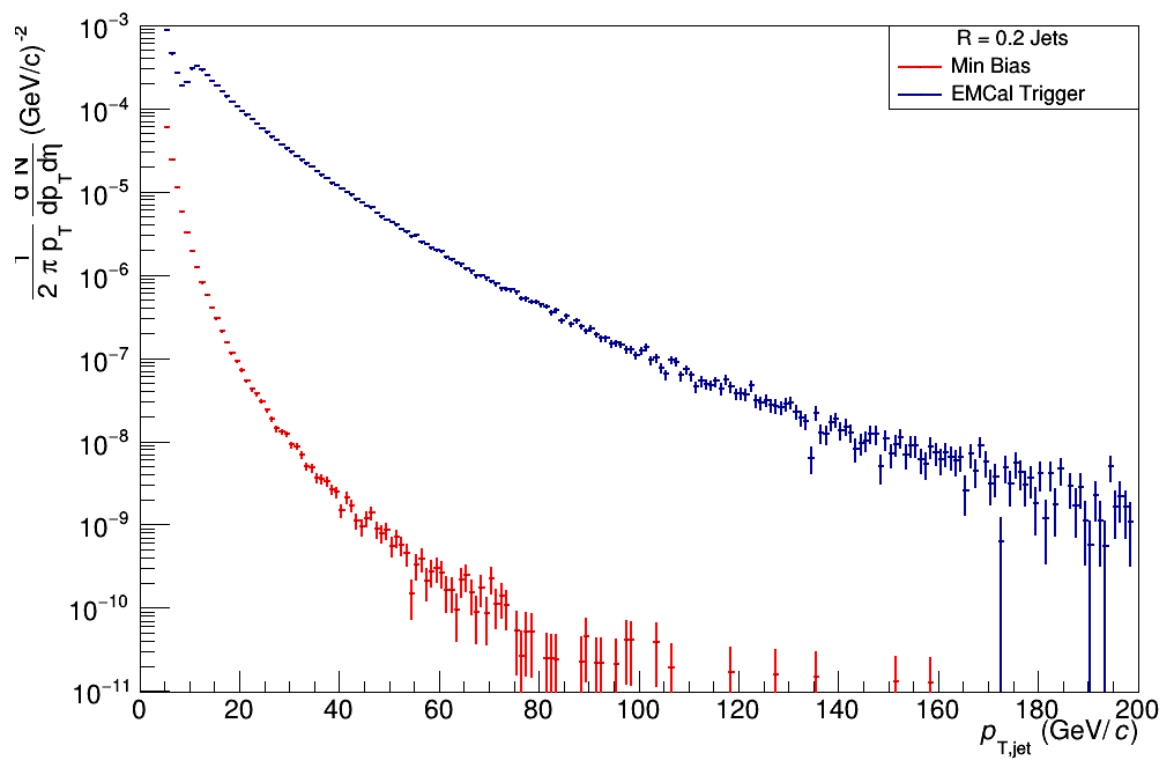


Figure 6.1: Raw inclusive $R = 0.2$ jet spectra from the 8 TeV Min Bias and EMCal triggered data

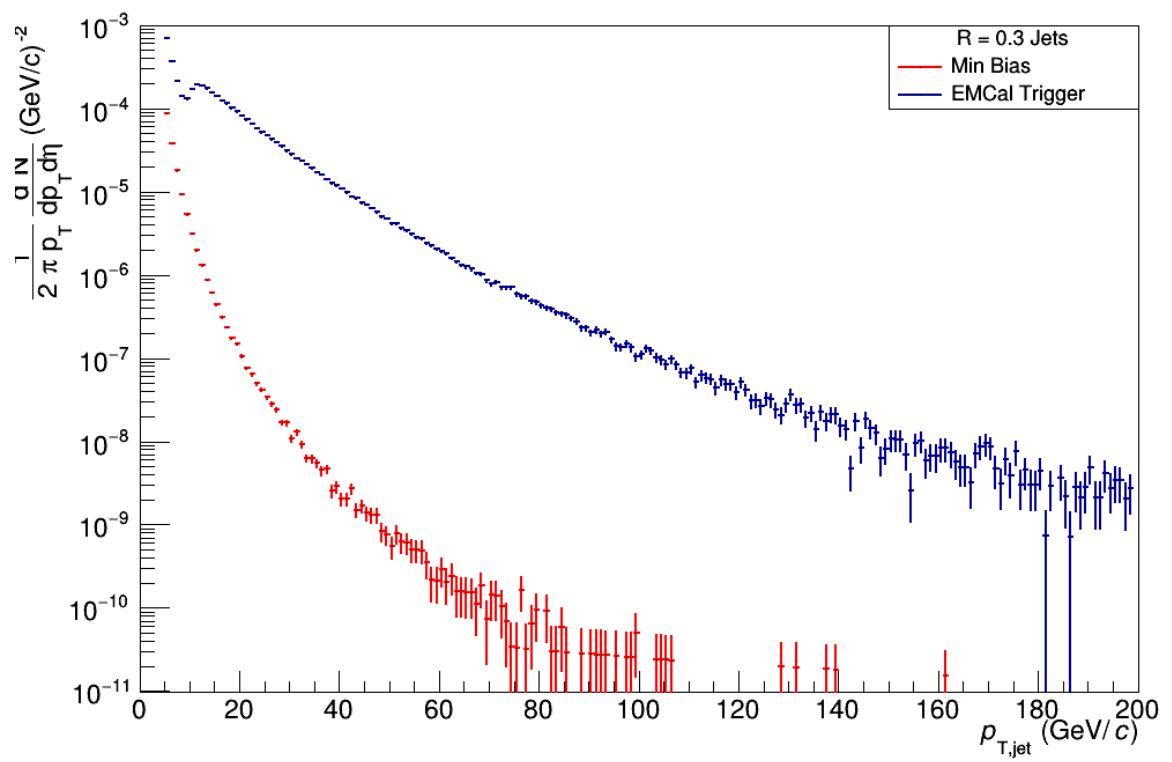


Figure 6.2: Raw inclusive $R = 0.3$ jet spectra from the 8 TeV Min Bias and EMCal triggered data

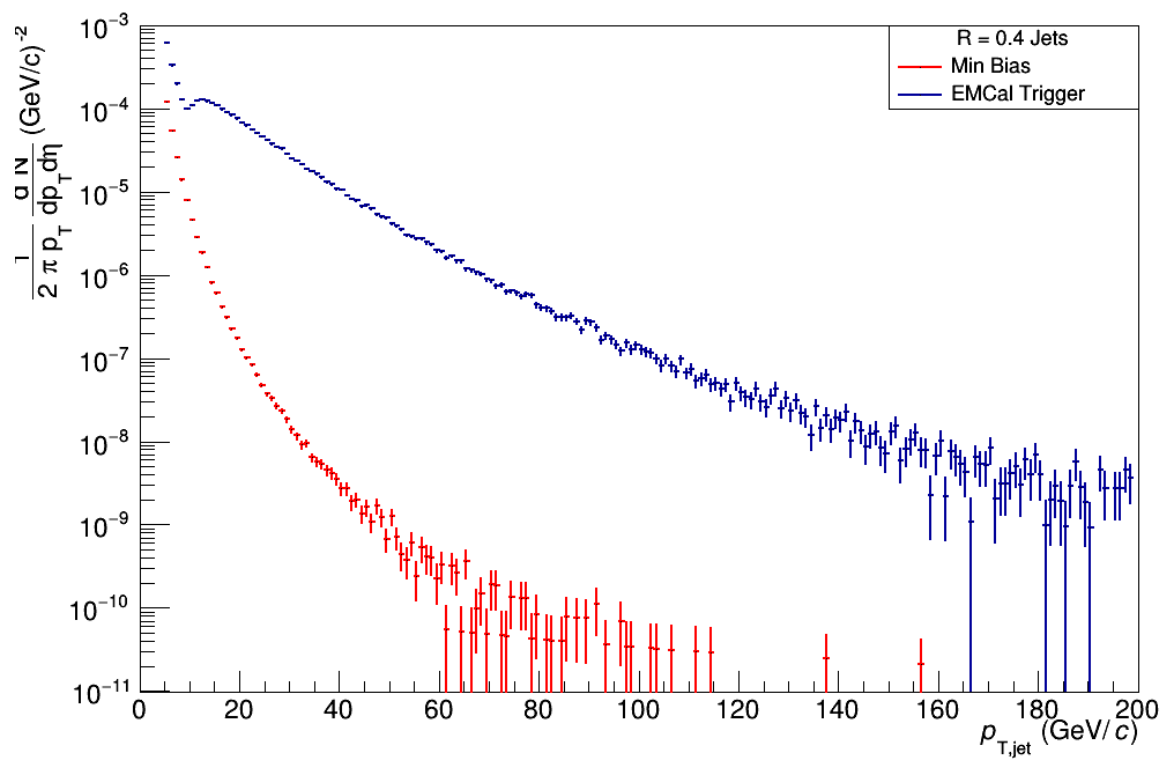


Figure 6.3: Raw inclusive $R = 0.4$ jet spectra from the 8 TeV Min Bias and EMCal triggered data

next sections of this chapter will discuss corrections to the data including trigger scaling unfolding.

6.2 Acceptance Correction

Jet spectra, cross-sections, and ratios of cross-sections are reported over the full azimuth angle and pseudorapidity acceptance in this thesis. Because jets are constrained to the EMCAL a geometric factor was used to correct for the limited acceptance of the detector. This thesis explored jet radii between 0.1 and 0.5, in order to study the effects of wide angle radiation on jet fragmentation. Jet measurements in heavy-ion collisions typically use radii of 0.2 to reduce the impact of the high multiplicity . Due to these geometric corrections the centroid of a jet is constrained to,

$$|\eta_{jet}| \leq 0.7 - R, \quad 1.4 + R \leq \phi_{jet} \leq 3.14 - R. \quad (6.2)$$

$$A(p_T) = \frac{(1.4 - 2R) \times (1.745 - 2R)}{2\pi}. \quad (6.3)$$

For jets between $R = 0.1$ through $R = 0.5$ the following jet acceptance corrections were used, see Table 5.2.

6.3 EMCAL Triggered Data

As discussed in Chapter 3, the ALICE detector is unable to record all events that occur in the experiment. The use of a trigger allows for events with rare processes to be saved with

a high efficiency and analyzed. The high- p_T EMCal trigger used for the 8 TeV data extends the kinematic reach of the spectra and the sample of jets from the data. This thesis looked at the two primary Level-1 triggers configured for the EMCal, the jet trigger and the gamma trigger[106]. Although both of the Level-1 triggers were investigated in this analysis, only the EGA trigger was ultimately used for the final jet cross-sections and spectra.

The jet trigger is a patch consisting of 32 x 32 EMCal towers. The patch samples all possible tower conditions until the patch meets the minimum predefined energy threshold. Once this threshold is surpassed the event is recorded and tagged as a jet triggered event. A similar procedure is followed for the gamma trigger, but with a smaller patch region of 4 x 4 towers and a different energy threshold.

The bump at low- p_T seen in Figures 6.1 - 6.3 is the trigger turn on curve and the peak corresponds to the trigger threshold for the EGA trigger. A jet in the EMCal acceptance should fire the jet trigger and the gamma should fire due to the presence of a photon or electron. The EMCal triggered events have a higher yield of jets compared to the Min Bias spectra. The triggered data is downscaled, this corrects the enhancement and makes the triggered data equivalent to the Min Bias data. The triggered data also needs to be corrected by reconstructing the jet that fired the jet trigger. This analysis was concerned with analyzing

Table 6.1: EMCal jet acceptance for radii 0.1 - 0.5.

Jet R	A
0.1	0.296
0.2	0.214
0.3	0.146
0.4	0.091
0.5	0.048

jets that fired the trigger and removing any bias to processes outside of jet production. Therefore jets were matched to the trigger patch. In order to only correct jets that fired a trigger in the EMCal the following procedure was implemented. First both the jet and gamma trigger patches were reconstructed offline. Next the energy thresholds were set for each trigger. Then the centroid of the trigger was found by finding the center-of-mass for each reconstructed patch in η, ϕ). After all patches are reconstructed and their weighted centroids found the patch each patch is geometrically matched to the jet centroid. The geometrical matching requirement followed a simple quadratic relationship which constrained the center of the trigger to inside the jet radius,

$$\sqrt{(\phi_{jet} - \phi_{EMCalpatch})^2 + (\eta_{jet} - \eta_{EMCalpatch})^2} \leq R_{jet}. \quad (6.4)$$

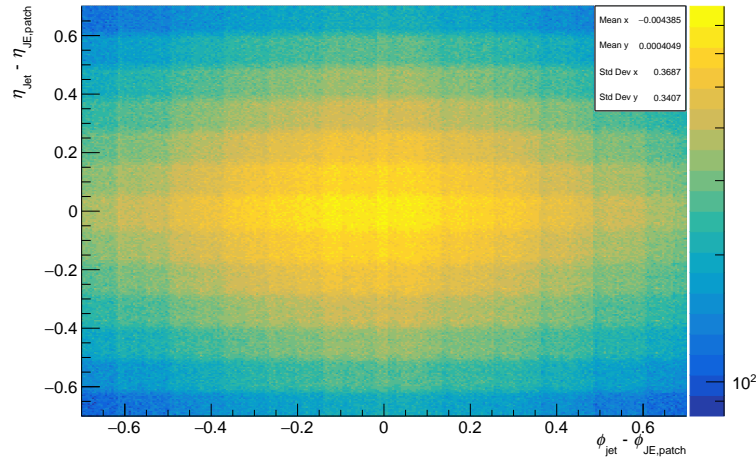


Figure 6.4: Distance to closest reconstructed jet patch to $R = 0.2$ jet with the EMCal triggered data.

Figures 6.4 and 6.5 show the distance between a reconstructed jet and its closest reconstructed EMCal trigger patch for $R = 0.2$ jets using the triggered data. Since a trigger

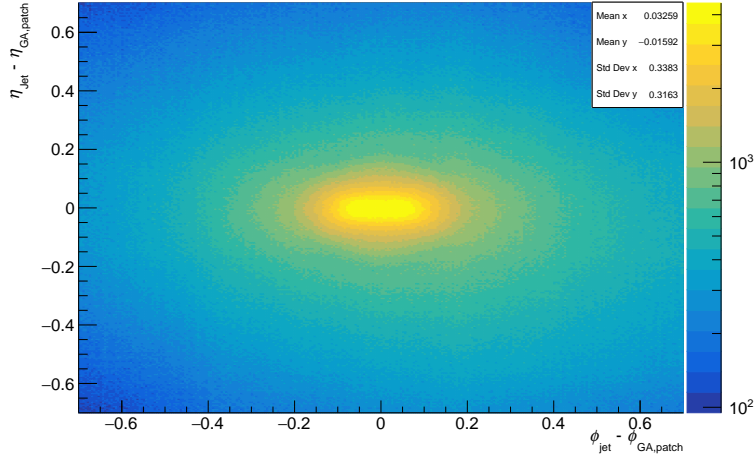


Figure 6.5: Distance to closest reconstructed gamma patch to $R = 0.2$ jet with EMCal triggered data.

patch may be fired if two or more jets are within the geometric area of the trigger patch this could lead to double counting. In order to correct for this, the jet spectra from the triggered data is scaled by the number of triggers, N_{trig} , fired that fell within the jet. We can see that with the gamma trigger that the peak of the distribution was within the jet radius of $R = 0.2$ while with the jet trigger the distribution is more uniformly distributed. Although the jet patch was investigated for use in this analysis complications with the trigger reconstruction meant that only the gamma patch was used for the final jet measurements.

Once this correction was implemented, the triggered data were then downscaled in order to combine it with the Min Bias data. The downscale correction factors, shown in Figure 6.6, were obtained by taking the ratio of the EMCal jet spectra to the Min Bias jet spectra and fitting the plateau region to a line. Below ~ 40 GeV/ c , the efficiency in the triggered data is changing rapidly and hard to determine. Due to the Min Bias data being sufficient in measuring the low kinematic range of the jet spectra the downscaled EMCal data is used

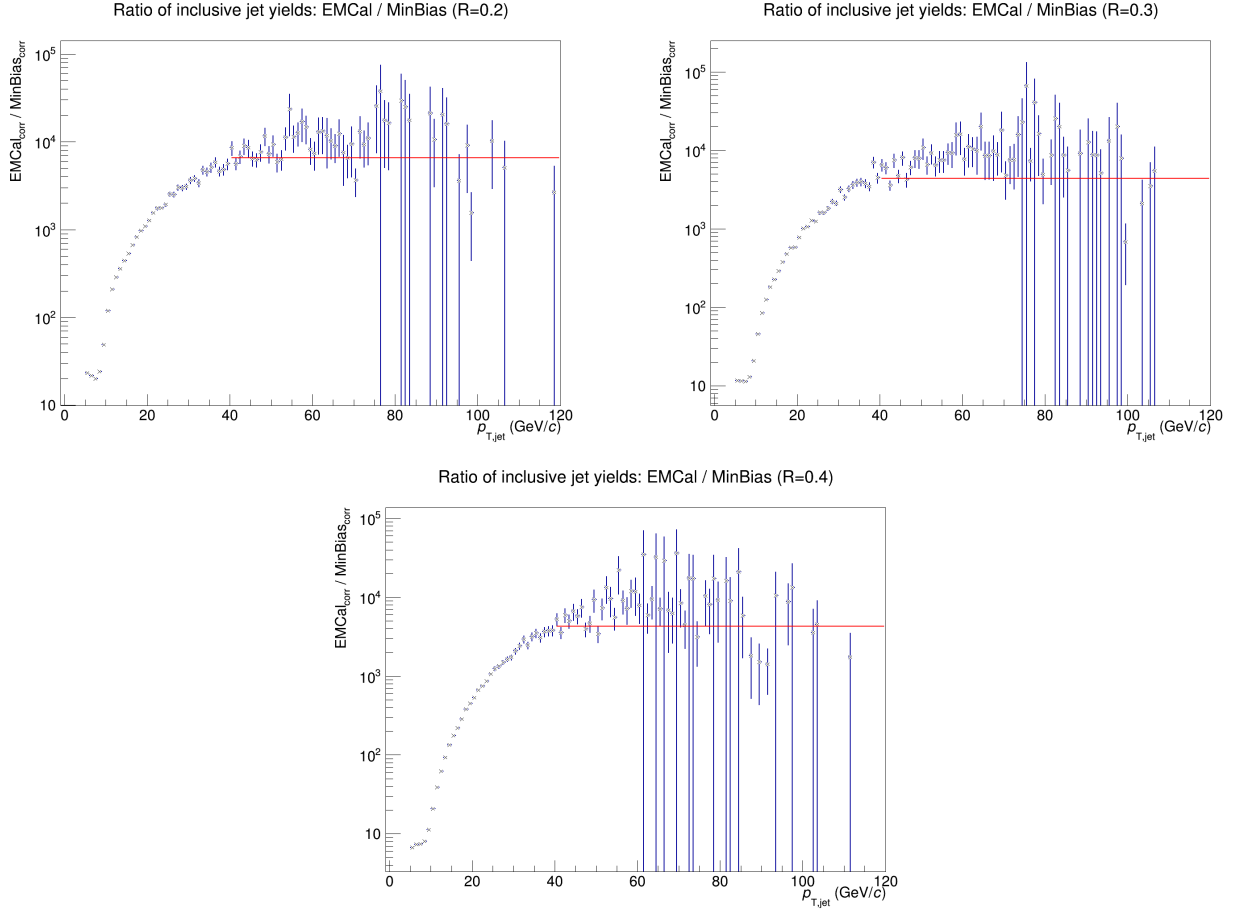


Figure 6.6: EMCal triggered data correction factors for $R=0.2$, $R=0.3$, and $R=0.4$ jets.

at $40 \text{ GeV}/c$ and above. The scale factors seen in 6.6 were obtained after the corrections to the Monte Carlo models were done.

6.4 Particle Level Corrections

The reconstructed jet p_T has a number of detector effects present in the measurement. These effects included such things as:

- Tracking inefficiencies from the TPC and ITS.

- Missing jet energy components from long-lived particles, such as the K_L^0 and neutron, that are cut by the EMCAL timing requirement.
- TPC track p_T and EMCAL cluster energy resolutions.
- Hadronic corrections to the EMCAL cluster spectrum.
- Material loss in the detectors.

‘Bin-by-bin’ corrections is a method by which these detector effects are removed from the raw inclusive jet spectra so that a ‘true’ jet spectra may be obtained and compared with theoretical calculations or other experimental results.

In order to correct a jet spectra, it is necessary to generate a response matrix that simulates the described effects above. In order to generate the response matrix, a Pythia generated event is embedded into a GEANT simulation of the ALICE detector. Each LHC period has a unique GEANT simulation produced for it to account for changes in the detector performance. The differences in the simulations take into account all the hot and dead sectors for the subdetectors, along with their calibrated performance during that specified data taking. The bin-by-bin corrections used in this analysis were taken from the Pythia+GEANT simulations produced from the ALICE collaboration. The magnitude of any one of the effects unfolding is supposed to account for is not expected to be very large, but combined may be significant, thus the Monte Carlo corrections are an important step in this analysis.

Response Matrix

The output from the Pythia portion of the simulation contains all the final state hadrons, regardless if they will be detected in the experiment. This is known as the particle-level. The

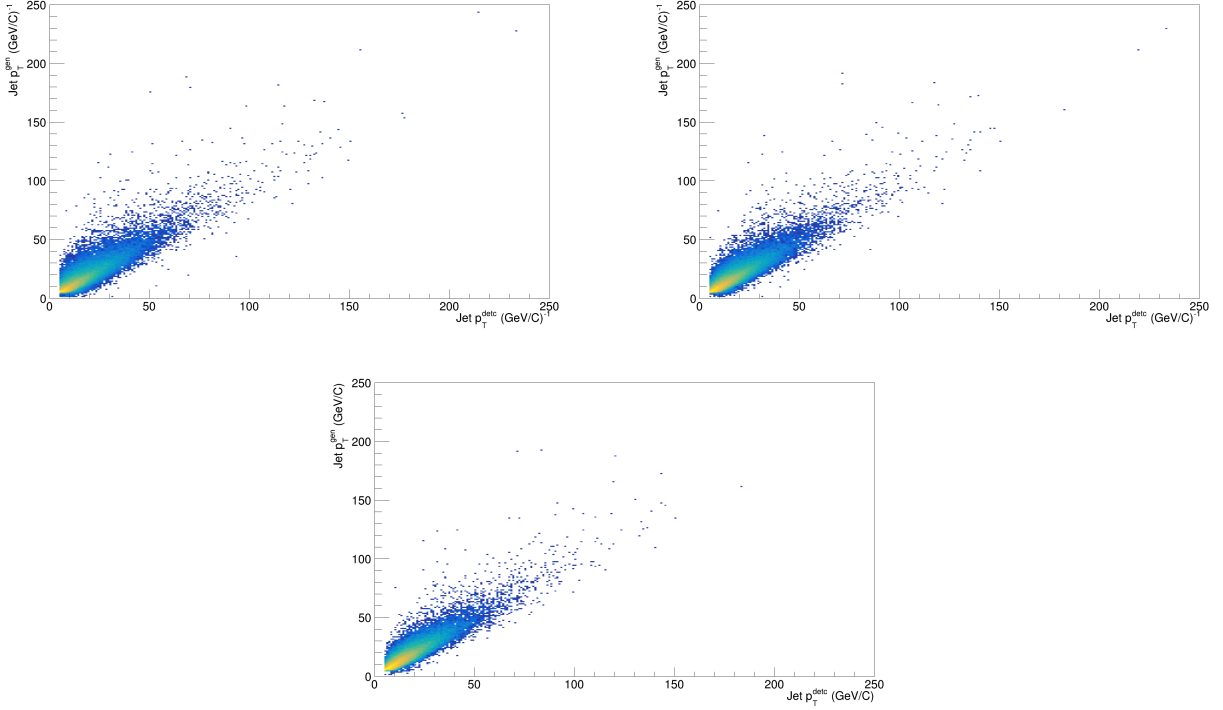


Figure 6.7: Response Matrices for $R = 0.2$, $R = 0.3$, and $R = 0.4$ jets.

particle-level Pythia jets are constructed from the primary particles generated via Pythia.

After the particle-level jet passes through the GEANT simulation of ALICE we obtain the detector-level jets with all detector inefficiencies incorporated. The response matrix is constructed by geometrically matching particle-level jets to detector-level. The particle-level jet centroid $(\phi_{part}, \eta_{part})$ is matched to the detector-level jet centroid (ϕ_{det}, η_{det}) via a constraint on the displaced distance between the two jet centroids. This distance was constrained to: $\Delta R = \sqrt{(\phi_{part} - \phi_{det})^2 + (\eta_{part} - \eta_{det})^2} \leq 0.25$. Once a jet was matched at the detector level to a jet generated from the particle level the response matrix was incremented by jet p_T at both the detector and Monte Carlo levels.

Figure 6.7 shows the response matrices for the $R = 0.2$, $R = 0.3$, and $R = 0.4$ jets. The response matrices display a somewhat linear relationship below 50 GeV on both axis and

show that above ~ 100 GeV the matrices lack statistics. This is primarily due to the Monte Carlo Pythia and PHOJet events simulated for the 8 TeV pp run did not model the high- p_T EMCal triggers. The jet finder was configured for a minimum jet energy of 100 MeV and no minimum energy requirement at the particle-level. The detector level jet finders were configured in the same manner as they were for the raw jet spectra measurement.

Corrections to Particle Level

Unfolding was performed using the `RooUnfold`[108] software package. `RooUnfold` can perform corrections using the bin-by-bin method, it can also unfold using either the Bayesian or singular value decomposition. Unfolding was initially attempted but due to limited statistics it was unstable. Corrections were applied using the bin-by-bin[109] algorithm.

$$C_{MC}(p_T^{low} : p_T^{high}) = \frac{\int_{p_T^{low}}^{p_T^{high}} dp_T \frac{dF_{meas}^{uncorr}}{dp_T} \times \frac{d^2 N_{MC}^{particle}/d\eta dp_T}{d^2 N_{MC}^{detector}/d\eta dp_T}}{\int_{p_T^{low}}^{p_T^{high}} dp_T \frac{dF_{meas}^{uncorr}}{dp_T}} \quad (6.5)$$

where $d^2 N_{MC}^{particle}/dp_T d\eta$ is the Pythia particle level inclusive jet spectra, $d^2 N_{MC}^{detector}/dp_T d\eta$ is the GEANT detector-level inclusive jet spectra, dF_{meas}^{uncorr}/dp_T is a weight function which minimizes the dependence on the two simulation spectra shapes, and finally p_T^{low} and p_T^{high} are the lower and upper bin limits. Due to the limited statistics derived from the available Monte Carlos, the bin-by-bin corrections were stable for a jet momentum range of: $p_{T,jet} \in [10 \text{ GeV}, 120 \text{ GeV}]$ for both the raw Min Bias and EMCal triggered data sets.

Corrected Jet Spectra

At low- p_T it was observed that unfolding increased the yield of the spectra while at high- $p_T \geq 40$ GeV the yield was decreased for all jet radii in this analysis. This is most likely due to the lack of statistics in the response matrix. Once the bin-by-bin corrections have been performed for the fine binned spectra the output along with the bin-by-bin correction factors are obtained between 10 GeV and 120 GeV, these corrected spectra are shown in Figure 6.8, 6.9, and 6.10.

Unfolded EMCal Triggered Spectra

The bin-by-bin procedure was repeated again for the EMCal triggered jet spectra. The response matrix from the Min Bias sample was used for the bin-by-bin unfolding. The detector level and particle level jets were configured in the same manner as above and the output from the unfolded triggered spectra are reported over the same kinematic range as the Min Bias spectra, as seen in Figure 6.11, 6.12, and 6.13.

Due to the limitations of the response matrix, the bin-by-bin corrections of the EMCal triggered data was only stable up to 120 GeV. Again, it should be noted that the hump in the EMCal jet spectra is due to the firing threshold of the trigger. The corrected EMCal jet spectra were used to estimate the ratio that the jet yields between the Min Bias and triggered data samples, from this point the trigger scaling was calculated.

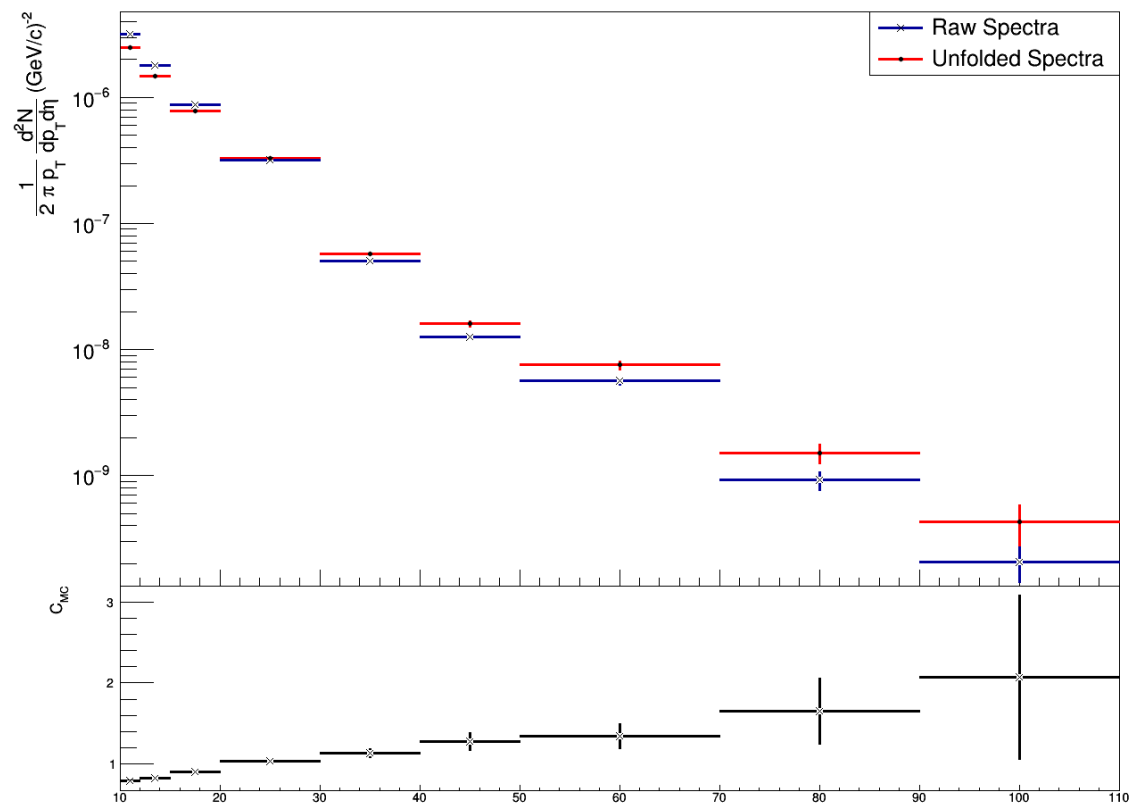


Figure 6.8: $R = 0.2$ bin-by-bin corrected Min Bias jet spectra.

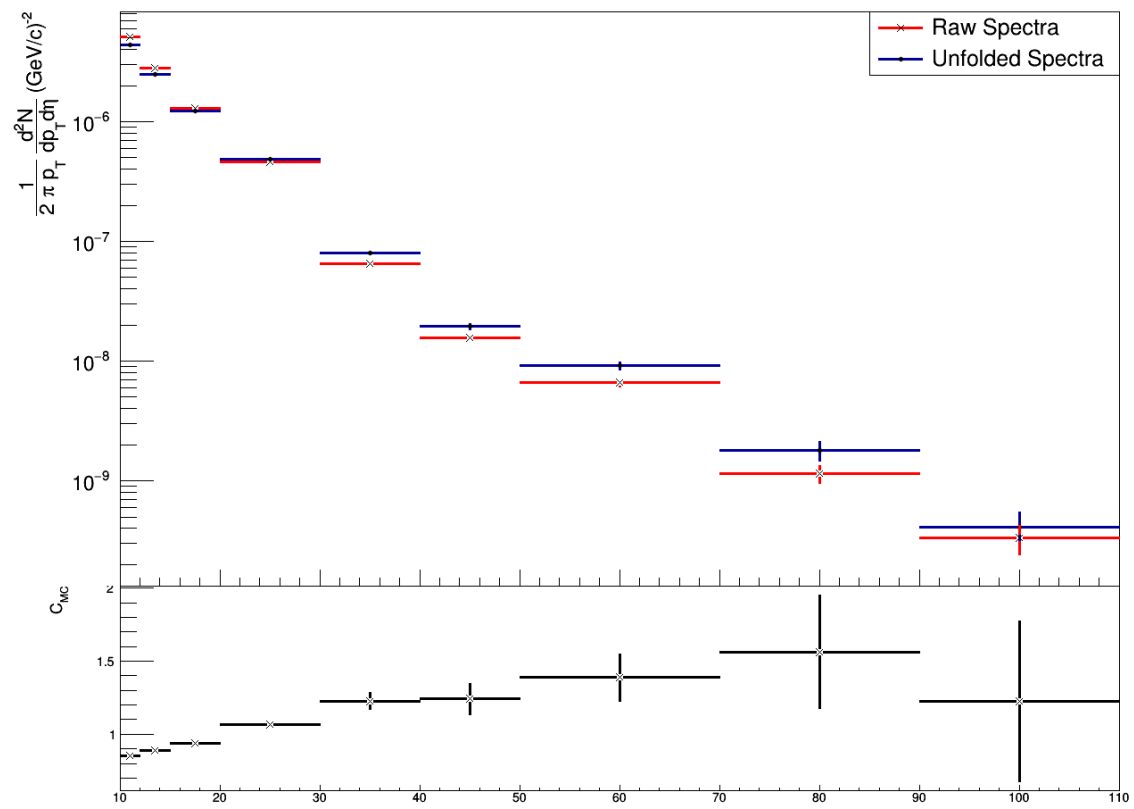


Figure 6.9: $R = 0.3$ bin-by-bin corrected Min Bias jet spectra.

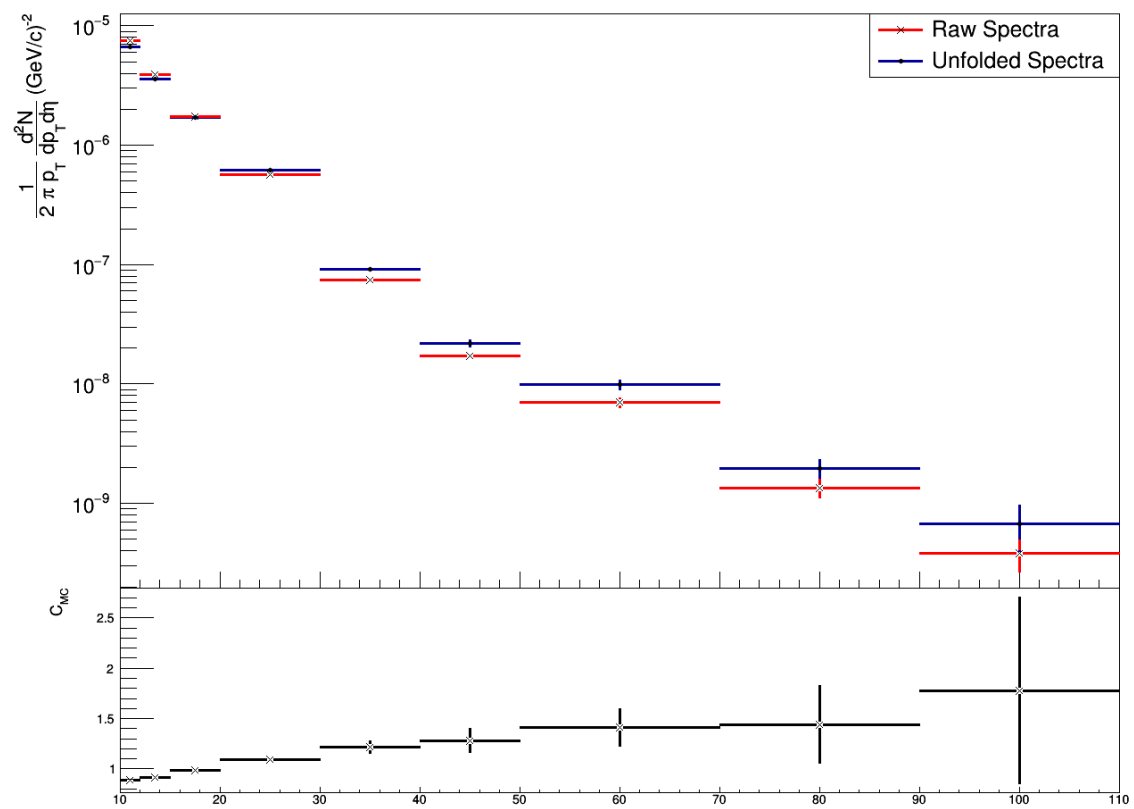


Figure 6.10: $R = 0.4$ bin-by-bin corrected Min Bias jet spectra.

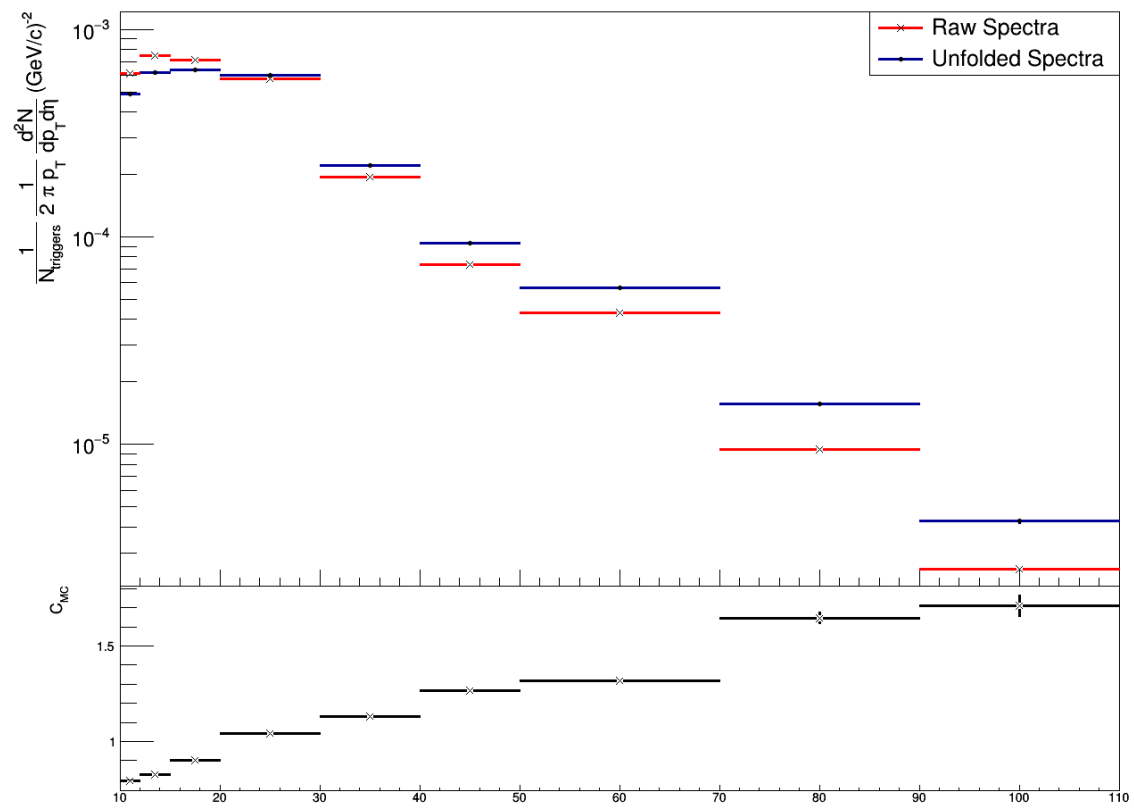


Figure 6.11: $R = 0.2$ bin-by-bin corrected EMCAL triggered jet spectra.

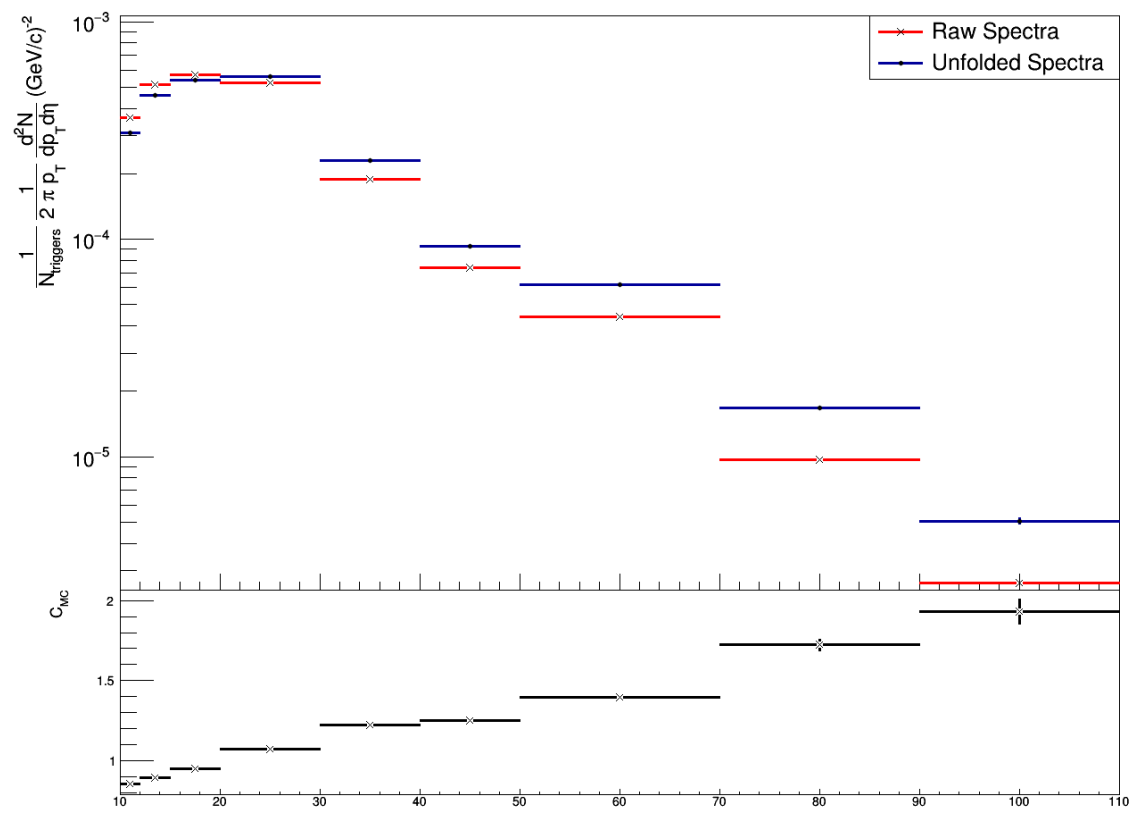


Figure 6.12: $R = 0.3$ bin-by-bin corrected EMCAL triggered jet spectra.

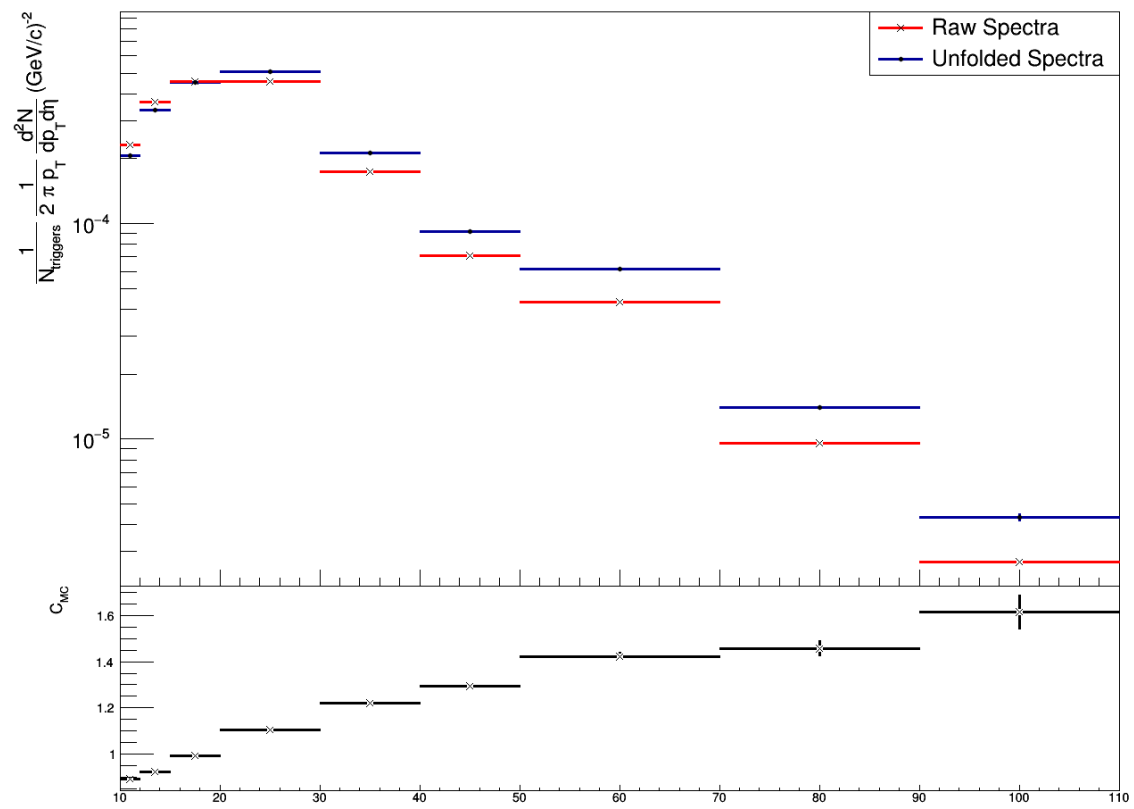


Figure 6.13: $R = 0.4$ bin-by-bin corrected EMCAL triggered jet spectra.

6.5 Jet Reconstruction and Matching Efficiency

In order to quantify the inefficiencies due to unfolding along with the inefficiencies in the ALICE experiment in reconstructing jets, we quantify the jet reconstruction efficiency, $\epsilon_{reco}(p_{T,jet})$, and the jet matching efficiency, $\epsilon_{match}(p_{T,jet})$.

$$\epsilon_{reco}(p_{T,jet}) = \frac{N_{reco}(p_{T,jet})}{N_{Truth}(p_{T,jet})} \quad (6.6)$$

$$\epsilon_{match}(p_{T,jet}) = \frac{N_{match}(p_{T,jet})}{N_{Truth}(p_{T,jet})} \quad (6.7)$$

where $N_{reco}(p_{T,jet})$ is the reconstructed jet yield at the detector level per p_T bin, $N_{match}(p_{T,jet})$ is the reconstructed jet at the detector level that was matched to a particle level jet per p_T bin, and $N_{Truth}(p_{T,jet})$ is the particle-level particle jet yield from the Pythia embedded event per p_T bin.

The $N_{Truth}(p_{T,jet})$ were obtained by running FastJet on Pythia events with no constituent p_T cut, while $N_{match}(p_{T,jet})$ and $N_{reco}(p_{T,jet})$ had the same kinematic cuts as the data driven analysis mentioned earlier in this chapter. The particle-level jets contained no geometric acceptance cut in order to account for jets that may have been reconstructed at the detector level, but had no match to a particle level because part of the particle level jet was outside the EMCAL acceptance. The spectra were corrected by these efficiencies after the bin-by-bin corrections were performed. The correction factors are shown in Figures 6.14 and 6.15.

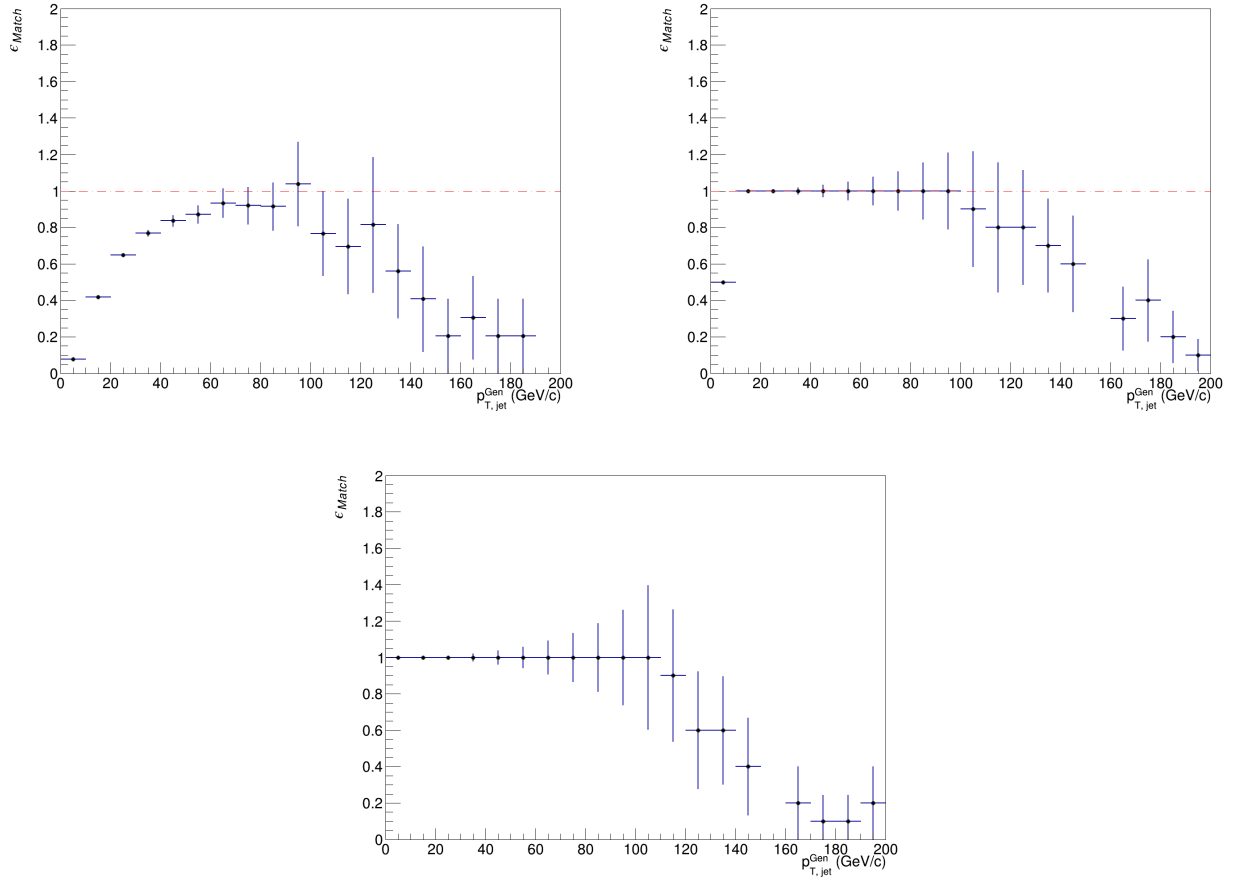


Figure 6.14: Jet matching efficiency for jets between $R = 0.2$ and $R = 0.4$.

6.6 Systematic Uncertainties

The systematics may be broken into two categories: uncertainties in the jet energy scale (JES) which shift the momentum spectra along the momentum axis, and uncertainties in the jet yield, which shift the spectra along the spectra/cross-section axis. The total systematic uncertainty to the jet cross-section is obtained by adding each contributing systematic together in quadrature. The systematical and statistical uncertainties presented in this analysis will be reported as uncertainties to the yield of the spectra.

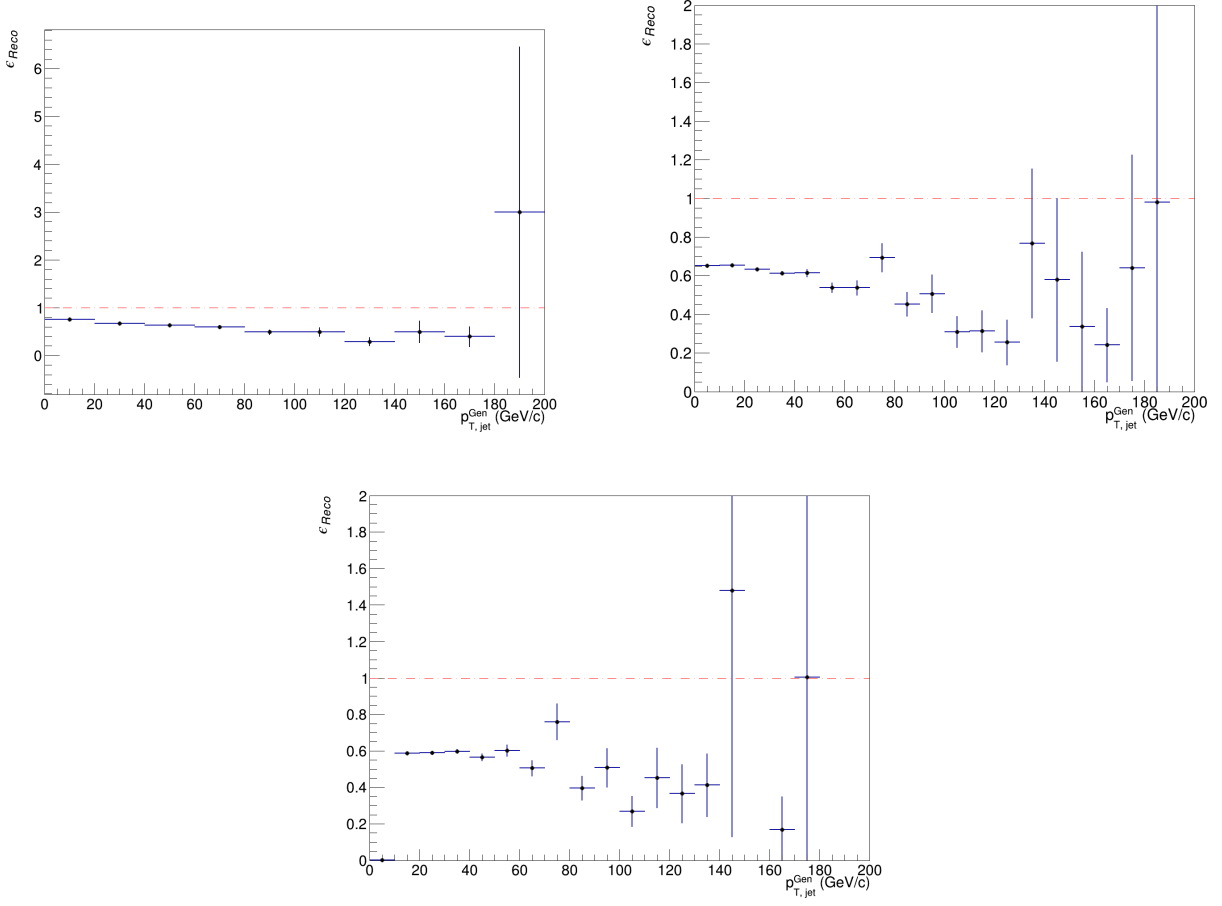


Figure 6.15: Jet reconstruction efficiency for jets between $R = 0.2$ and $R = 0.4$

In general the systematic uncertainties were obtained by using small variations for the analysis cuts and parameters used in this analysis. A feature in some of the following uncertainties is the wide statistical fluctuations seen at the highest jet p_T bins. A small change in a input parameter can cause a relatively large flow into and out of a high granularity bin, which does not represent a systematic uncertainty. In order to obtain the systematic at the highest jet p_T bins it was necessary to extrapolate the uncertainty from the low p_T range. There is a degree of arbitrariness to this procedure and at times the uncertainty from a given systematic is assigned a conservative value.

Systematic Uncertainty to Jet Energy Scale

The following sections present and discuss the uncertainties caused by shifts to the JES.

Tracking Efficiency Sensitivity

Only a fraction of charged tracks generated by the hard scattering of two protons will be detected in the TPC due to its finite track efficiency. Uncertainties in the efficiency of the TPC were studied and found to account for a 5% discrepancy[110]. In order to obtain the uncertainty on the JES due to the tracking efficiency, this analysis was repeated while throwing out 5% of the tracks from each event and remeasuring the jet spectra. Once this new jet spectrum was generated, it was corrected using the bin-by-bin corrections and the ratio of this new spectra was taken with the original spectra to gauge the uncertainty from the tracking efficiency.

Figure 6.16 shows the systematical uncertainties for $R = 0.2$, $R = 0.3$, and $R = 0.4$ jets. From the figures a 10% systematic was assigned to $R = 0.2$ and $R = 0.3$ jets, while a 15% systematic uncertainty was given to $R = 0.4$ jets for this analysis.

Hadronic Correction

The uncertainty in the JES due to the hadronic correction applied to EMCAL clusters was measured by changing the nominal value of $f_{sub} = 1$ in equation 5.2 to 0.7 and the analysis chain is repeated. Figure 6.17 shows the ratio of the new spectra with the original, and the uncertainty due to the hadronic correction was around 5% for all jet radii.

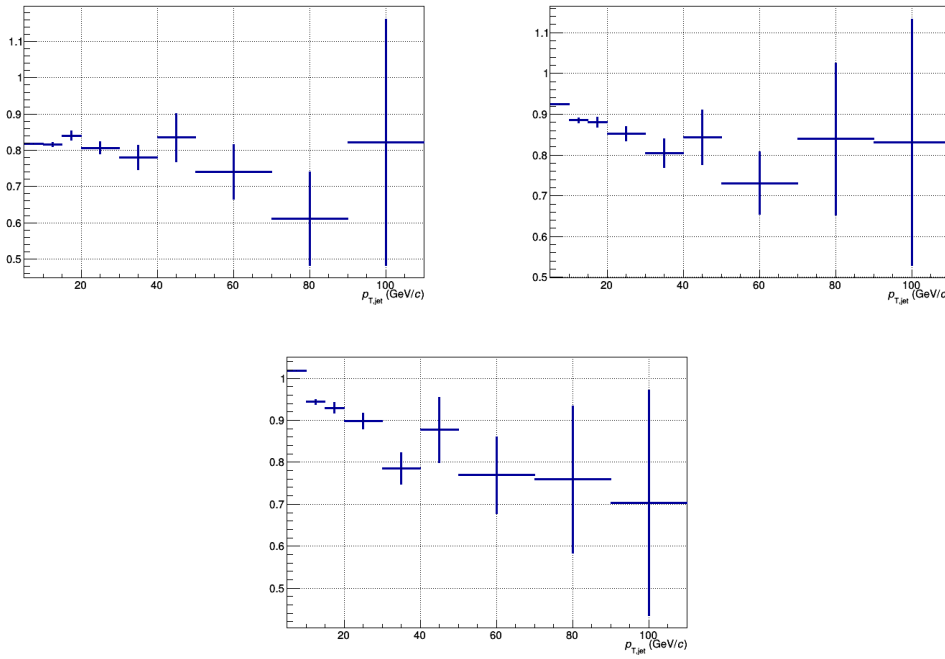


Figure 6.16: Systematic due to TPC tracking efficiency; $R = 0.2$ (top left), $R = 0.3$ (top right), $R = 0.4$ (bottom).

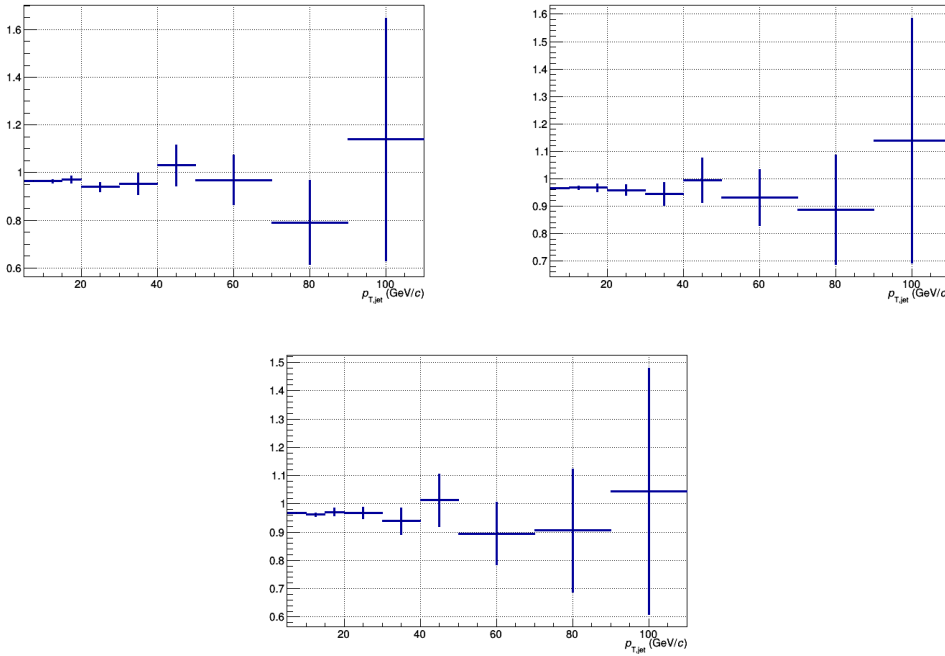


Figure 6.17: Systematic due to hadronic correction efficiency; $R = 0.2$ (top left), $R = 0.3$ (top right), $R = 0.4$ (bottom).

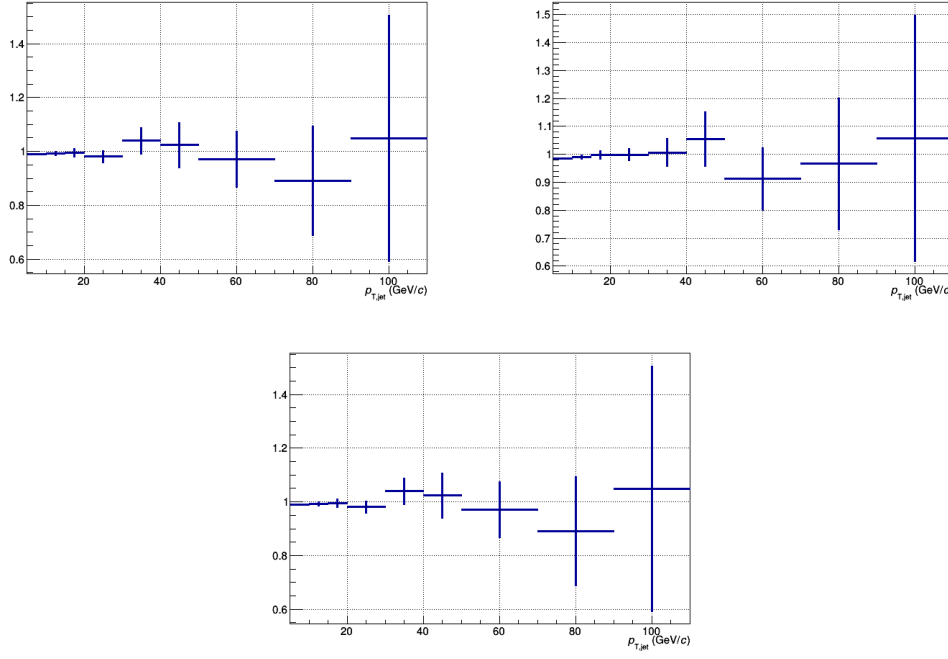


Figure 6.18: Systematic due to EMCal clusterization algorithm; $R = 0.2$ (top left), $R = 0.3$ (top right), $R = 0.4$ (bottom).

Sensitivity to EMCal Clusterization Algorithm

The clusterization algorithm, discussed in Chapter 5, which limits the number of EMCal towers in a cluster to a maximum of nine. In order to test the sensitivity the JES has to the clusterization algorithm, a different algorithm was chosen and a new spectra was generated. The new algorithm is similar to the original algorithm with the exception that the total size of the cluster is forced to be smaller then nine towers. Similar to the other systematics presented, we see large fluctuations at high- p_T due to sparsely field binning.

Figure 6.18 shows the systematic uncertainty to the clusterization for each of the jet radii. At low- p_T I assigned an uncertainty of between 1% and 3% for a given jet radii. At high- p_T I assigned a 5% for $R = 0.2$ and 10% uncertainty for $R = 0.3$ and $R=0.4$ jets to help account for the statistical fluctuations.

Systematic Uncertainty to Jet Yield

The following sections discuss the systematic uncertainties affecting the jet yield.

Track p_T Resolution

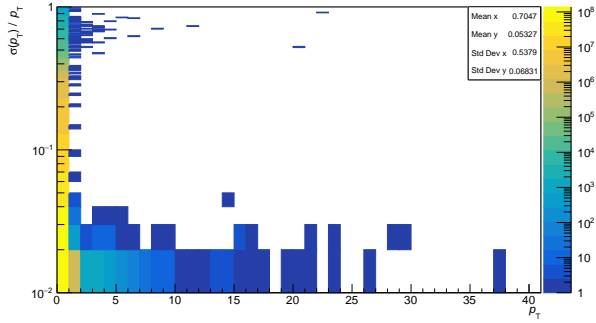


Figure 6.19: Inclusive TPC track momentum resolution, Min Bias 8 TeV.

The momentum resolution of the TPC is estimated using the covariance matrix generated from the Kalman filtering[111] pad signal on the TPC read-out region. Figure 6.19 shows that for the vast majority of the p_T range in this analysis the momentum resolution is below 3%. To estimate the systematic uncertainty due to the p_T resolution, tracks are smeared by 3% in p_T and the variation between the new and original spectra are used to estimate the uncertainty. From the generated plots seen in Figure 6.20 the uncertainties were below 5% for all jet radii.

Cluster Energy Resolution

Similar to the p_T resolution, the uncertainty due to the EMCal energy resolution is done by smearing the energy of the clusters by the energy resolution function measured from the test beam and seen in Figure 3.8. The ratio of the spectra with the smear versus the original

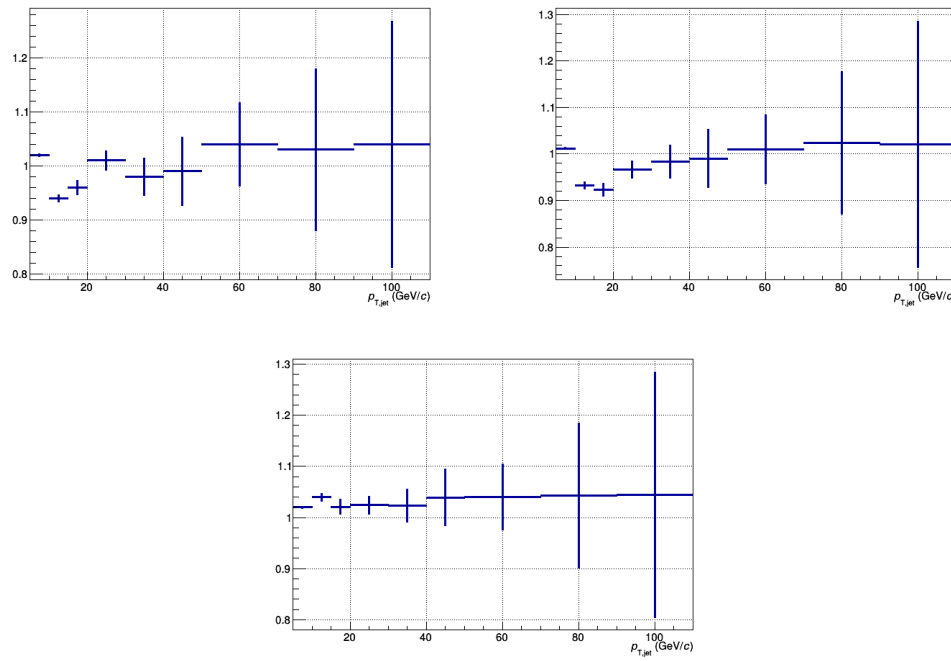


Figure 6.20: P_T resolution systematic; $R = 0.2$ (top left), $R = 0.3$ (top right), $R = 0.4$ (bottom).

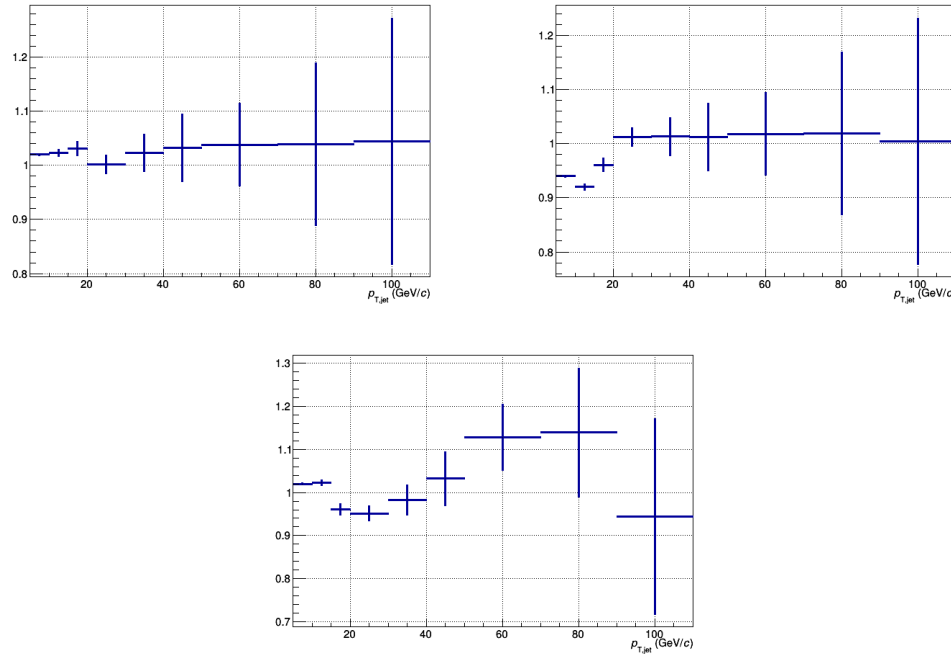


Figure 6.21: Systematic due to the energy resolution; $R = 0.2$ (top left), $R = 0.3$ (top right), $R = 0.4$ (bottom).

spectra are show in Figure 6.21. The uncertainties for the $R = 0.2$ and $R = 0.3$ jets appear well defined and around 1% - 2%. The large variation with $R = 0.4$ jet energy resolution is due to low statistical fluctuations and a conservative 5% uncertainty was assigned to this radii.

Luminosity Uncertainty

The luminosity of a hadronic collider, \mathcal{L} , is given by the expression

$$\mathcal{L} = \frac{R}{\sigma} \quad (6.8)$$

where R is the interaction rate and σ is the visible cross section. Due to the fact that we only measure events within a 10 cm window within the primary vertex region of ALICE we must scale the total luminosity to that which is delivered within the experiment. This scale factor is determined by dividing the total number of Min Bias events to those accepted within the 10 cm window. $N_{MB}^{tot}/N_{MB}^{10cmvertex} = 1.024$, which was obtained from the event QA criteria used in this analysis as discussed in Chapter ???. The total cross-section and luminosity along with there uncertainties were determined during a a special 8 TeV Van der Meer scan run performed in April of 2012[105]. The total systematic uncertainty for the Min Bias trigger were obtained by measuring the visible cross-section using the T0 and V0 detectors. The Min Bias trigger was defined as V0AND which required a hit in both the V0A and V0C. The cross section was reported as being a combined average for Min Bias with the V0AND as,

$$\sigma_{V0} = (55.8 \pm 1.2) \text{ mb} \quad (6.9)$$

with a combined systematic uncertainty of 2.19% on the visible cross section and 2.60% on the luminosity. Both this cross-section and its uncertainty were scaled by the 1.024 factor to account for the 10 cm vertex region in ALICE before combining with the spectra to obtain the final cross-sections.

Total Uncertainty

A summary of the total systematic errors used in the final analysis is given in Table 6.2. Some of the uncertainties, for example the p_T resolution, used an asymmetric value between the low- p_T range, below 40 GeV/c , versus high- p_T range, above 60 GeV/c , to account for the statistical fluctuations. The systematic uncertainties to the yield and JES were added in quadrature.

Table 6.2: Summary of JES and Yield Uncertainties.

Systematic Errors			
Systematic	R = 0.2 Jets	R = 0.3 Jets	R = 0.4 Jets
Clusterization (below 40 GeV/c)	1.0%	1.0%	3.0%
(above 40 GeV/c)	5.0%	10.0%	10.0%
Hadronic	5.0%	4.0%	5.0%
Track Eff (below 40 GeV/c)	20.0%	15.0%	15.0%
(above 40 GeV/c)	25.0%	20.0%	25.0%
Unfolding	6.0%	6.0%	6.0%
p_T Resolution	2.0%	1.0%	4.0%
E Resolution	2.0%	1.0%	5.0%
Luminosity	2.2%	2.2 %	2.2%
Total Sys (low- p_T)	8.9%	6.6%	10.9%
(high- p_T)	10.3%	9.1 %	14.5%

Chapter 7

Jet Results and Outlook

7.1 8 TeV Inclusive Jet Results and Discussion

Differential Jet Cross-Section

Figures 7.1, 7.2, and 7.3 show the inclusive jet cross-sections from $R = 0.2$ through $R = 0.4$ jet radii. The figures are split into two sections. The cross-sections as measured from ALICE along with the associated statistical errors are shown in black. The associated systematic errors from the ALICE data as discussed in this chapter are shown as the green shaded area. Min Bias Monte Carlo generated events from Pythia (Red), PHOjet (blue), and Herwig (magenta) are included and shown as colored bands to convey the statistical uncertainties from each simulation. On the bottom half of each plot are the relative ratios of the ALICE jet cross-sections to one of the Monte Carlos using the same color scheme as above.

First, we can see that the cross-sections are measured over a wide range, about five orders of magnitude, between $20 \text{ GeV}/c$ to $160 \text{ GeV}/c$ in p_T . The $R = 0.2$ and $R = 0.3$

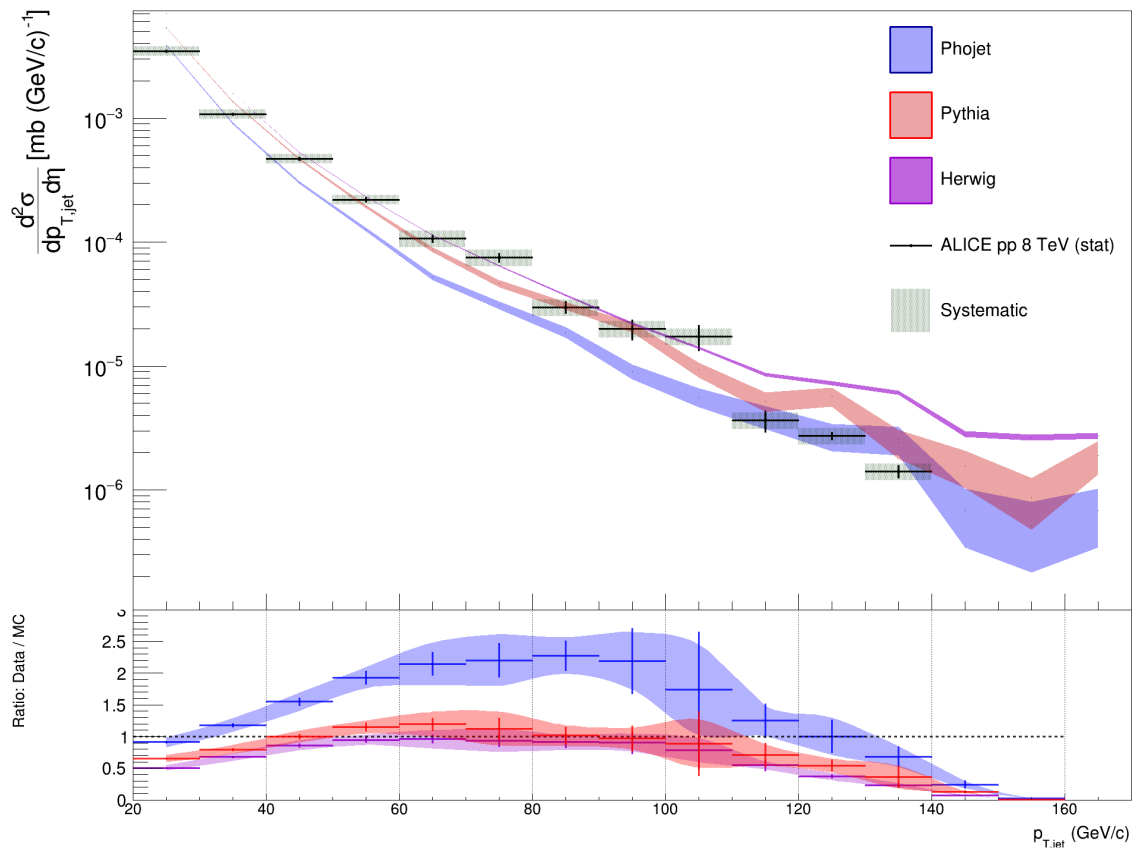


Figure 7.1: 8 TeV inclusive jet differential cross-section for $R = 0.2$.

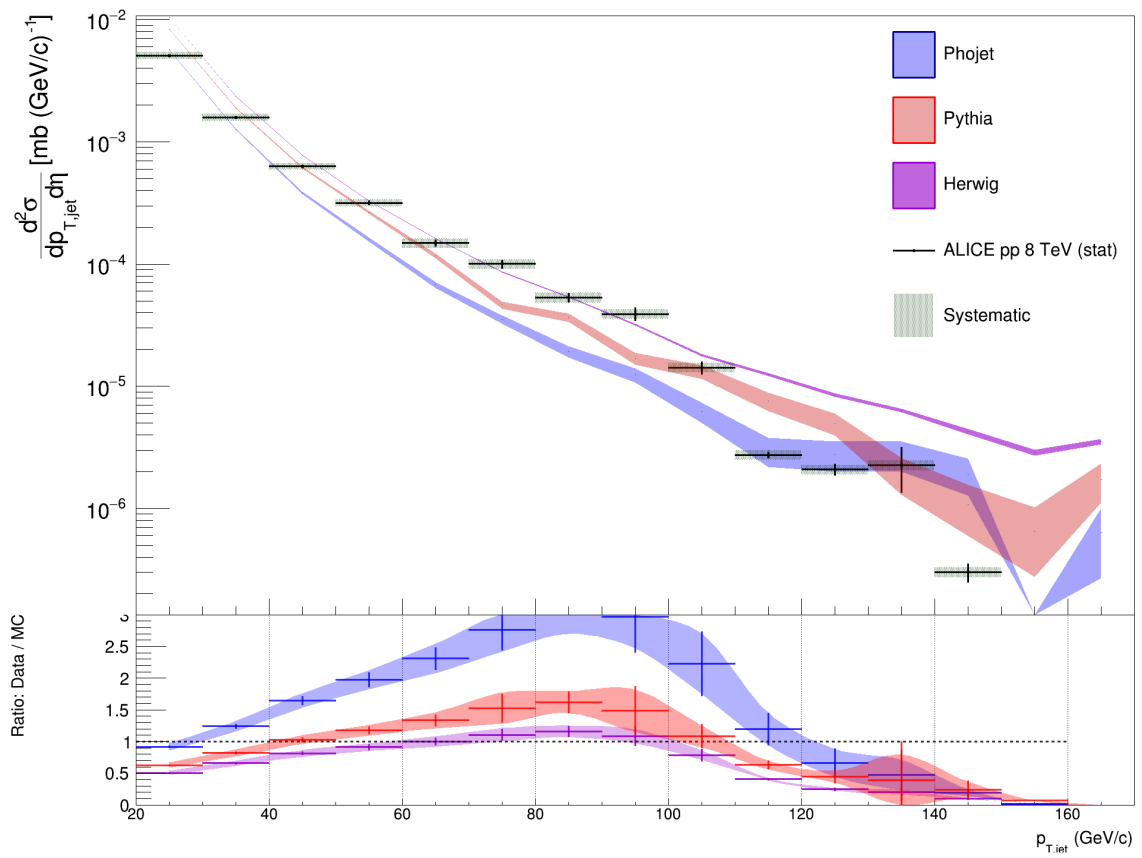


Figure 7.2: 8 TeV inclusive jet differential cross-section for $R = 0.3$.

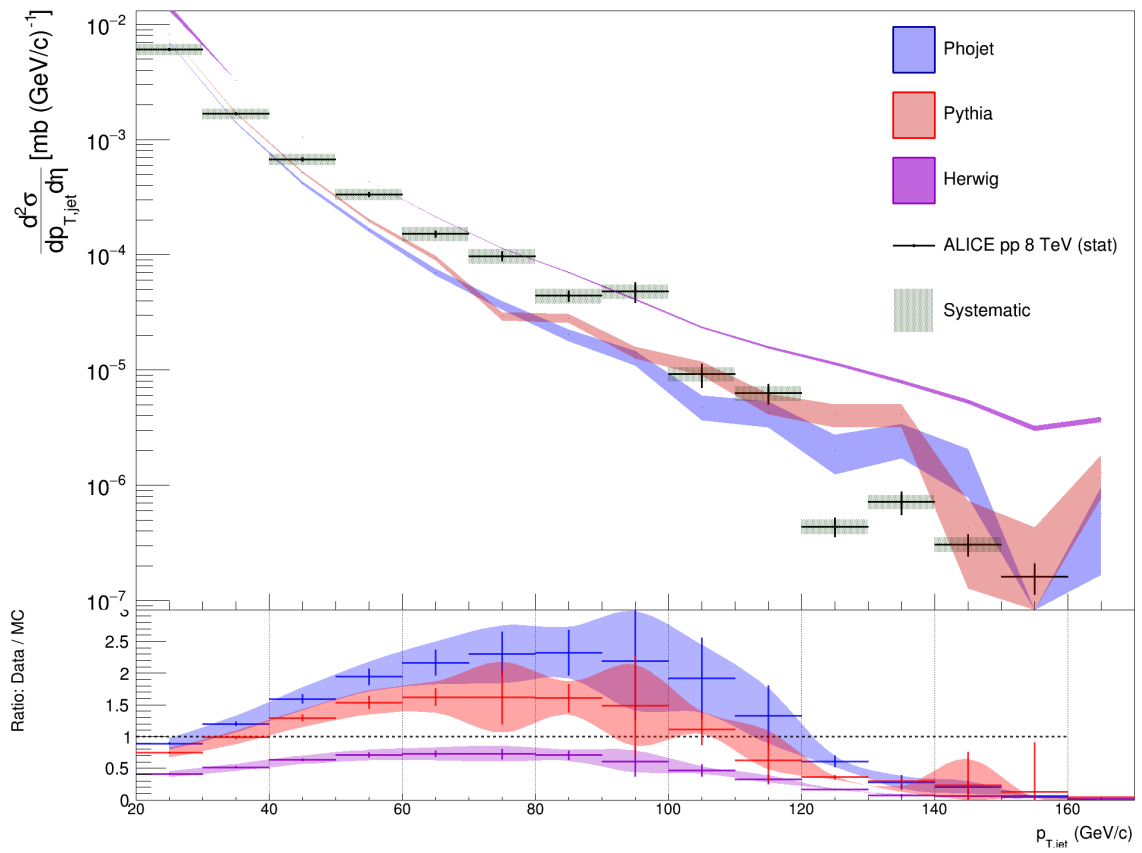


Figure 7.3: 8 TeV inclusive jet differential cross-section for $R = 0.4$.

cross-sections show a well defined trend between $20 \text{ GeV}/c$ - $\sim 100 \text{ GeV}/c$, after this point the data has a hard drop after which the data points show wider fluctuations. This same trend is seen in the $R = 0.4$ jet cross-section but the jerk happens earlier in p_T around $80 \text{ GeV}/c$. The fluctuations are an artifact of the bin-by-bin corrections and the lack of EMCal trigger simulations as discussed in Chapter 6.

Comparing the data to the models we see that the two simulations produced by the ALICE Collaboration, Pythia and PHOjet, tend to under predict the data. PHOjet has the least agreement with the data. The poor agreement with PHOjet can be explained by the fact that PHOjet is an older Monte Carlo generator and better tuned to describing lower energy experiments. PHOjet may also be under estimating the data because it focuses on describing photon interactions. The Monte Carlo Simulation from Herwig was produced on a local server farm at the University of Tennessee. I used a Min Bias tune of Herwig and generated 150 million events and we see that reflected in the low statistical errors. The Herwig simulation tends to slightly over predict the data. Both Herwig and Pythia agree well with the data between $20 \text{ GeV}/c$ to $100 \text{ GeV}/c$. It is hard to say that one is ‘better’ than the other because of the relatively large statistical errors from Pythia. However, for the $R = 0.4$ jet cross-section we can see that the data seems to trend better towards the clusterization description of hadronization used in Herwig. At large jet radii hadronization should be a smaller effect. The better agreement seen for $R = 0.4$ jets may be due to Herwig being better at modeling QCD compared to Pythia or PHOjet.

These results help to further our understanding of jets and the QCD phenomena behind them. Through scaling these results may serve as a reference for heavy-ion collisions and help to better constrain our understanding of parton energy loss mechanisms in the QGP.

Jet Cross-Section Ratios

The ratio of the jet cross-sections as a function of the jet radii is defined as,

$$\mathcal{R}(p_T; R_1, R_2) = \frac{d\sigma(R_1)/d\eta dp_T}{d\sigma(R_2)/d\eta dp_T}, \quad (7.1)$$

where R_1 and R_2 are the jet radii in question. This probes the transverse structure of jets and is sensitive to QCD hadronization[112]. Figures 7.4, 7.5, and 7.6 report the ratios of the jet cross-sections between $R = 0.2 / R = 0.4$, $R = 0.3 / R = 0.4$, and $R = 0.2 / R = 0.3$ respectively. The figures show the relative ratios plotted from the 8 TeV ALICE data, Pythia, PHOjet, and Herwig. Errors between the cross-sections of different radii are considered uncorrelated and added in quadrature to form the error bars reported in the figures.

A similar analysis to this thesis was performed using a 2.76 TeV data sample collected from ALICE[113] and it is compared to the 8 TeV data seen in Figure 7.4 and 7.6 using green bullet points. In order to avoid double counting by sampling the same jet found using different radii parameters in Fastjet I used a disjointed samples of the 8 TeV data generate each of the ratio plots. In order to use the full data set it would be necessary to generate the covariance matrix which is a non-trivial process. From the results of the cross-section ratios, we see that the 8 TeV data as reported from this thesis agrees well with the 2.76 TeV results in Figure 7.4. Interestingly it seems that the PHOjet model agrees well with the data for all three figures and is the simulation that agrees the best for the $\sigma(R = 0.3) / \sigma(R = 0.4)$ ratio. It can be concluded that the Pythia ratios have the least agreement because it only includes the LO matrix to calculate partonic showers, which does not model the angular

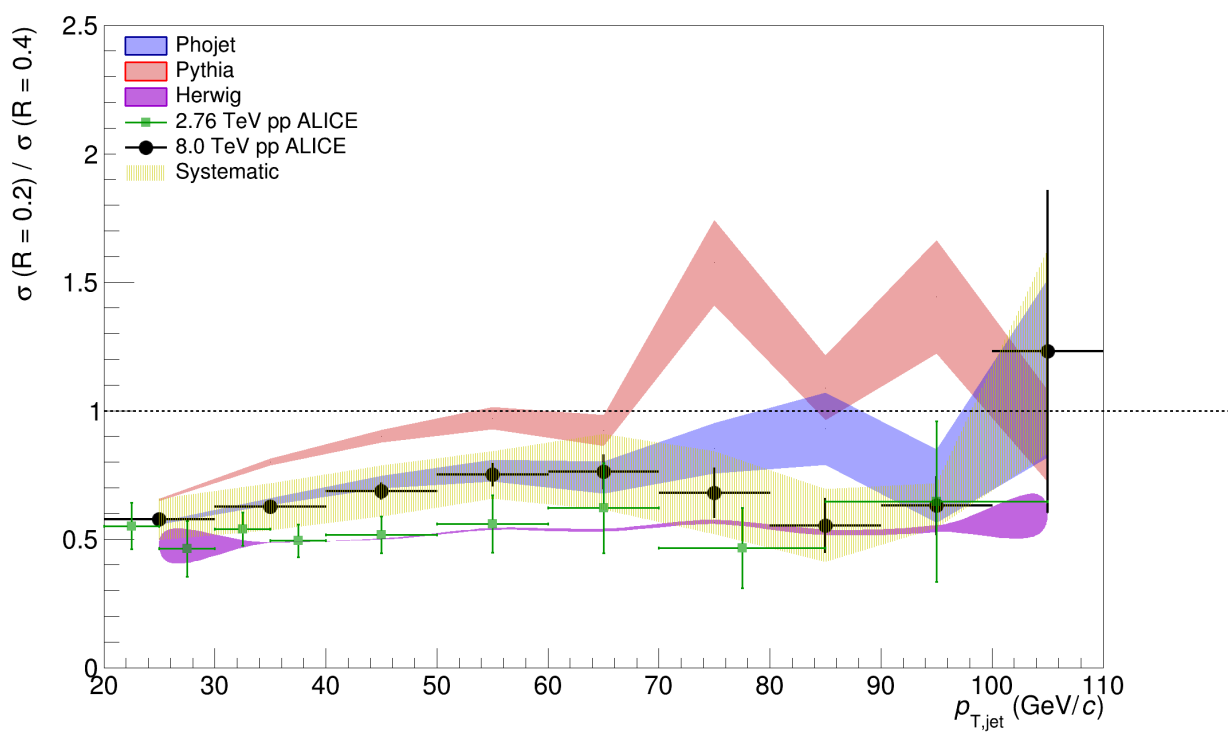


Figure 7.4: Ratio of the jet cross-sections $R = 0.2$ to $R = 0.4$.

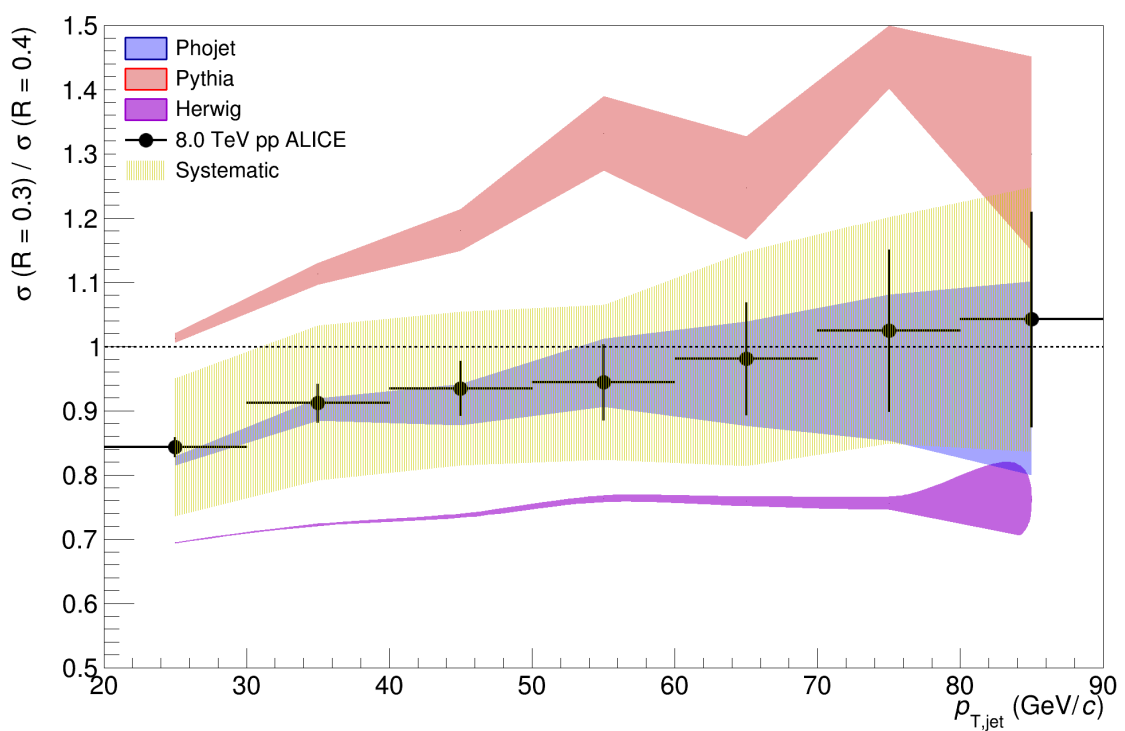


Figure 7.5: Ratio of the jet cross-sections $R = 0.3$ to $R = 0.4$.

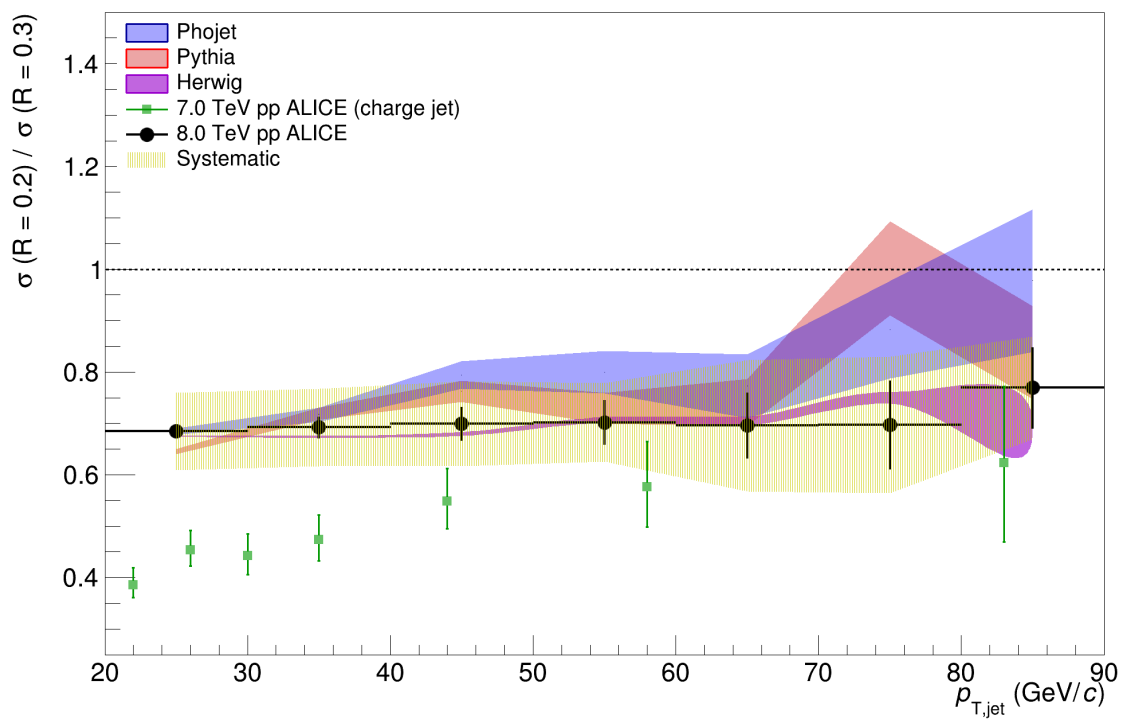


Figure 7.6: Ratio of the jet cross-sections $R = 0.2$ to $R = 0.3$.

ordering of QCD radiation very well. Herwig tends to under predict the data, especially at low- p_T , which is expected and may be understood in terms of limitations modeling low energy background particles with tune used in this thesis (v2.3).

Similar to the previous results these ratios can be used to constrain jet quenching in the QGP. These results also report the first ratio of jet cross-sections between $R = 0.2$ and $R = 0.3$. This is especially helpful for heavy-ion collisions as most jet results from heavy-ions use either an $R = 0.2$ or $R = 0.3$ jet radius to suppress the background in the high multiplicity environment.

7.2 Summary and Conclusion

Hadronization is the phenomena by which colored partons are confined to colorless hadrons. When two partons undergo a high energy collision they will fragment and hadronize into a jet. By measuring jet properties in proton-proton collisions we can probe different hadronization models. In heavy-ion collisions a new form of matter known as the Quark-Gluon Plasma is created. Jets are created at the earliest moments of a heavy-ion collision and are sensitive to energy loss mechanisms in the QGP. Reconstructing full jets is a promising method for probing jet quenching and hadronization

This thesis presents the first measurements of inclusive full jets at $\sqrt{s} = 8$ TeV using the ALICE detector. Using the time projection chamber and the electromagnetic calorimeter can obtain a satisfactory level of uncertainty to both the jet energy scal and jet yields. This thesis presents a novel approach to reconstruct the jet that fired the high- p_T EMCal trigger and how to scale this in order to combine with minimmum bias events. by combing the two

triggered data samples we obtained jet measurements over a wide kinematic range, especially to low momentum. Low-momentum reconstruction of jets and their constituents probe jet quenching in heavy-ion collisions.

The good agreement between the r8 TeV data and Monte Carlo simulations show the jets are a well calibrated probe for testing QCD phenomena. In terms of the kinematic reach, the results of this thesis are in good agreement with QCD calculations down to $20 \text{ GeV}/c$ through $100 \text{ GeV}/c$ in p_T . This range may be extended with better Monte Carlos in the future. With a better Monte Carlo simulations we could see the range extend to $200 \text{ GeV}/c$ in p_T using the EMCal triggered data. The comparisons with the Monte Carlos agree well, with the most tension lying with PHOjet

The results from this thesis can also be used in future heavy-ion runs to probe jet quenching, as these results would serve as a baseline comparison. The work in this thesis also presents the jet measurements from ALICE down to $20 \text{ GeV}/c$, which will be important for probing energy loss in the QGP. By measuring these very low energy jets we can probe the full energy loss mechanism for partons traversing the QGP. Previous higher energy jet results would tend to bias to jets that traveled a very short distance through the QGP.

In addition to the jet results, this thesis presented work upgrading the ALICE TPC in anticipation for the high luminosity upgrade of the LHC anticipated to begin in mid-2021. The multiwire proportional chamber design of the original TPC will be replaced with a stack of gaseous electron multiplier foils that will allow for a continuous readout of data.

With the increase in energy and luminosity seen at the LHC, we have moved into the era of high-precision testing of pQCD. The work set forward by this thesis sets the stage for using jets future ALICE data sets, especially after the high luminosity upgrade of the LHC

is complete. Although it dates to 2012, the 8 TeV contains some of the largest data sets available at a given energy from the LHC. This makes it an important data set and worthy of future investigations. What results we will gain from the upgraded LHC and jets is only left to our imagination and to nature's mercy.

Bibliography

- [1] C. Patrignani et al. Review of Particle Physics. *Chin. Phys.*, C40(10):100001, 2016.
[xii](#), [xvii](#), [2](#), [143](#)
- [2] Vardan Khachatryan et al. Measurement of the inclusive 3-jet production differential cross section in proton–proton collisions at 7 TeV and determination of the strong coupling constant in the TeV range. *Eur. Phys. J.*, C75(5):186, 2015. [xii](#), [6](#)
- [3] Jets at cms and the determination of their energy scale, July 2012. [xii](#), [7](#)
- [4] Matt Dobbs and Jorgen Beck Hansen. The HepMC C++ Monte Carlo event record for High Energy Physics. *Comput. Phys. Commun.*, 134:41–46, 2001. [xii](#), [9](#)
- [5] J. Feltesse. Introduction to Parton Distribution Functions. *Scholarpedia*, 5(11):10160, 2010. revision #186761. [xii](#), [11](#)
- [6] Martin Erdmann. Investigation of quark - anti-quark interaction properties using leading particle measurements in e+ e- annihilation. *Phys. Lett.*, B510:29–35, 2001.
[xii](#), [12](#)
- [7] B. R. Webber. Hadronization. In *Proceedings: Summer School on Hadronic Aspects of Collider Physics, Zuoz, Switzerland, Aug 23-31, 1994*, pages 49–77, 1994. [xii](#), [13](#)
- [8] Bo Andersson, Sandipan Mohanty, and Fredrik Soderberg. Recent developments in the Lund model. In *36th Annual Winter School on Nuclear and Particle Physics (PINP 2002) and 8th St. Petersburg School on Theoretical Physics St. Petersburg, Russia, February 25-March 3, 2002*, 2002. [xii](#), [14](#)

- [9] Jan Rak and Michael J. Tannenbaum. *QCD in hard scattering*, pages 214–243. Cambridge Monographs on Particle Physics, Nuclear Physics and Cosmology. Cambridge University Press, 2013. [xiii, 16](#)
- [10] Gerald C. Blazey et al. Run II jet physics. In *QCD and weak boson physics in Run II. Proceedings, Batavia, USA, March 4-6, June 3-4, November 4-6, 1999*, pages 47–77, 2000. [xiii, 17](#)
- [11] Ryan Atkin. Review of jet reconstruction algorithms. *J. Phys. Conf. Ser.*, 645(1):012008, 2015. [xiii, 17, 22](#)
- [12] Bedangadas Mohanty. Exploring the QCD phase diagram through high energy nuclear collisions: An overview. *PoS*, CPOD2013:001, 2013. [xiii, 26, 29](#)
- [13] J. D. Bjorken. Highly relativistic nucleus-nucleus collisions: The central rapidity region. *Phys. Rev. D*, 27:140–151, Jan 1983. [xiii, 28](#)
- [14] Morad Aaboud et al. Measurement of the nuclear modification factor for inclusive jets in Pb+Pb collisions at $\sqrt{s_{\text{NN}}} = 5.02$ TeV with the ATLAS detector. *Phys. Lett.*, B790:108–128, 2019. [xiii, 30, 31](#)
- [15] Esma Mobs. The CERN accelerator complex. Complexe des accélérateurs du CERN. Jul 2016. General Photo. [xiii, 34](#)
- [16] W. M. Alberico, A. Beraudo, A. De Pace, A. Molinari, M. Monteno, M. Nardi, and F. Prino. Heavy-flavour spectra in high energy nucleus-nucleus collisions. *Eur. Phys. J.*, C71:1666, 2011. [xiii, 38](#)

- [17] J. Alme et al. The ALICE TPC, a large 3-dimensional tracking device with fast readout for ultra-high multiplicity events. *Nuclear Instruments and Methods in Physics Research A*, 622:316–367, October 2010. [xiii, 40](#)
- [18] Ralf Diener. Gas amplification with micro pattern gas detectors. [xiii, 41](#)
- [19] Betty Bezverkhny Abelev et al. Performance of the ALICE Experiment at the CERN LHC. *Int. J. Mod. Phys.*, A29:1430044, 2014. [xiii, 43](#)
- [20] G Bourdaud. Gamma-jet physics with the electro-magnetic calorimeter in the alice experiment at lhc. *Journal of Physics: Conference Series*, 110(3):032006, 2008. [xiii, 44](#)
- [21] U. Abeysekara et al. ALICE EMCal Physics Performance Report. 2010. [xiii, 46](#)
- [22] Cristiane Jahnke. J/ψ production as a function of event multiplicity in pp collisions at $\sqrt{s} = 13$ TeV using EMCAL-triggered events with ALICE at the LHC. In *14th International Workshop on Hadron Physics (Hadron Physics 2018) Florianopolis, Santa Catarina, Brazil, March 18-23, 2018*, 2018. [xiv, 47](#)
- [23] B Abelev et al. Upgrade of the ALICE Experiment: Letter of Intent. Technical Report CERN-LHCC-2012-012. LHCC-I-022. ALICE-UG-002, CERN, Geneva, Aug 2012. [xiv, 49, 50, 51](#)
- [24] Erik Brückner and Timo Hildén. GEM Foil Quality Assurance For The ALICE TPC Upgrade. *EPJ Web Conf.*, 174:03004, 2018. [xiv, 51, 60](#)

- [25] Purba Bhattacharya, Bedangadas Mohanty, Supratik Mukhopadhyay, Nayana Majumdar, and Hugo Natal da Luz. 3D simulation of electron and ion transmission of GEM-based detectors. *Nucl. Instrum. Meth.*, A870:64–72, 2017. [xiv](#), [52](#)
- [26] Dick Majka. The alice tpc upgrade project. Quark Matter 2017, 2017. [xiv](#), [xv](#), [54](#), [59](#)
- [27] Upgrade of the ALICE Time Projection Chamber. Technical Report CERN-LHCC-2013-020. ALICE-TDR-016, Oct 2013. [xiv](#), [51](#), [55](#)
- [28] Addendum to the Technical Design Report for the Upgrade of the ALICE Time Projection Chamber. Technical Report CERN-LHCC-2015-002. ALICE-TDR-016-ADD-1, Feb 2015. [xiv](#), [xv](#), [51](#), [56](#), [57](#)
- [29] Jens Erik Brücken and Timo Eero Hildén. The GEM QA Protocol of the ALICE TPC Upgrade Project. In *5th International Conference on Micro Pattern Gas Detectors (MPGD2017) Temple University, Philadelphia, USA, May 22-26, 2017*, 2018. [xv](#), [60](#), [61](#)
- [30] Francesco Noferini. The ALICE PID performance in Run 1 and perspectives in view of Run 2. In *Proceedings, 3rd Large Hadron Collider Physics Conference (LHC 2015): St. Petersburg, Russia, August 31-September 5, 2015*, pages 523–528, Gatchina, 2016. Kurchatov Institute, Kurchatov Institute. [xviii](#), [144](#)
- [31] Paul Langacker. Introduction to the Standard Model and Electroweak Physics. In *Proceedings of Theoretical Advanced Study Institute in Elementary Particle Physics on The dawn of the LHC era (TASI 2008): Boulder, USA, June 2-27, 2008*, pages 3–48, 2010. [1](#)

- [32] Tatsumi Aoyama, M. Hayakawa, Toichiro Kinoshita, and Makiko Nio. Tenth-Order Electron Anomalous Magnetic Moment — Contribution of Diagrams without Closed Lepton Loops. *Phys. Rev.*, D91(3):033006, 2015. [Erratum: *Phys. Rev.* D96,no.1,019901(2017)]. [1](#)
- [33] Michael Riordan. The discovery of quarks. *Science*, 256(5061):1287–1293, 1992. [4](#)
- [34] Frank Wilczek. Asymptotic freedom: From paradox to paradigm. *Proc. Nat. Acad. Sci.*, 102:8403–8413, 2005. [Rev. Mod. Phys.77,857(2005)]. [5](#)
- [35] J. D. Bjorken. Asymptotic sum rules at infinite momentum. *Phys. Rev.*, 179:1547–1553, Mar 1969. [7](#)
- [36] J. D. Bjorken. Can We Measure Parton Parton Cross-Sections? *Phys. Rev.*, D8:4098, 1973. [7](#)
- [37] Wolfgang Kurt Hermann Panofsky. Low q electrodynamics, elastic and inelastic electron (and muon) scattering. 1968. [11](#)
- [38] K. Kovarik, T. Jezo, A. Kusina, F. I. Olness, I. Schienbein, T. Stavreva, and J. Y. Yu. CTEQ nuclear parton distribution functions. *PoS*, DIS2013:274, 2013. [11](#)
- [39] Richard D. Ball, Valerio Bertone, Stefano Carrazza, Christopher S. Deans, Luigi Del Debbio, Stefano Forte, Alberto Guffanti, Nathan P. Hartland, José I. Latorre, Juan Rojo, and Maria Ubiali. Parton distributions for the LHC Run II. *JHEP*, 04(arXiv:1410.8849. EDINBURGH 2014-15. IFUM-1034-FT. CERN-PH-TH-2013-253. OUTP-14-11P. CAVENDISH-HEP-14-11):040. 138 p, Oct 2014. Comments: 138 pages, 64 figures. Several typos in text and references corrected, one reference added. [11](#)

- [40] Harald Fritzsch. QCD: 20 years later. In *QCD 20 Years Later: Proceedings, Workshop, Aachen, Germany, June 9-13, 1992*, pages 827–852, 1992. [12](#)
- [41] John C. Collins, Davison E. Soper, and George F. Sterman. Factorization of Hard Processes in QCD. *Adv. Ser. Direct. High Energy Phys.*, 5:1–91, 1989. [12](#)
- [42] Nora Brambilla, Xavier Garcia i Tormo, Joan Soto, and Antonio Vairo. The Logarithmic contribution to the QCD static energy at $N^{**}4$ LO. *Phys. Lett.*, B647:185–193, 2007. [12](#)
- [43] B. R. Webber. A QCD Model for Jet Fragmentation Including Soft Gluon Interference. *Nucl. Phys.*, B238:492–528, 1984. [15](#)
- [44] L. L. Jenkovszky, V. K. Magas, J. T. Londergan, and A. P. Szczepaniak. Explicit Model Realizing Parton-Hadron Duality. *Int. J. Mod. Phys.*, A27:1250157, 2012. [15](#)
- [45] J E Huth, N Wainer, K Meier, N J Hadley, F Aversa, Mario Greco, P Chiappetta, J P Guillet, S Ellis, Zoltán Kunszt, and Davison Eugene Soper. Toward a standardization of jet definitions. (FERMILAB-CONF-90-249-E):7 p, Dec 1990. [17](#)
- [46] Matteo Cacciari, Gavin P. Salam, and Gregory Soyez. FastJet User Manual. *Eur. Phys. J.*, C72:1896, 2012. [21](#), [23](#)
- [47] Megan Connors, Christine Nattrass, Rosi Reed, and Sevil Salur. Jet measurements in heavy ion physics. *Rev. Mod. Phys.*, 90:025005, 2018. [23](#)
- [48] Torbjorn Sjostrand, Stephen Mrenna, and Peter Z. Skands. A Brief Introduction to PYTHIA 8.1. *Comput. Phys. Commun.*, 178:852–867, 2008. [24](#)

- [49] Peter Zeiler Skands. Tuning Monte Carlo Generators: The Perugia Tunes. *Phys. Rev.*, D82:074018, 2010. [24](#)
- [50] A. Capella, U. Sukhatme, C.-I. Tan, and J. Tran Thanh Van. Dual parton model. *Physics Reports*, 236(4):225 – 329, 1994. [25](#)
- [51] Cheuk-Yin Wong. *Introduction to high-energy heavy-ion collisions*. World Scientific, Singapore, 1994. Erratum. [25](#)
- [52] Fritz W. Bopp, R. Engel, and J. Ranft. Rapidity gaps and the PHOJET Monte Carlo. In *High energy physics. Proceedings, LAFEX International School, Session C, Workshop on Diffractive Physics, LISHEP'98, Rio de Janeiro, Brazil, February 16-20, 1998*, pages 729–741, 1998. [25](#)
- [53] M. Bahr et al. Herwig++ Physics and Manual. *Eur. Phys. J.*, C58:639–707, 2008. [25](#)
- [54] T. Csorgo. New form of matter at CERN SPS: Quark matter but not quark gluon plasma. *Nucl. Phys. Proc. Suppl.*, 92:62–74, 2001. [,62(2000)]. [27](#)
- [55] I. Arsene et al. Quark gluon plasma and color glass condensate at RHIC? The Perspective from the BRAHMS experiment. *Nucl. Phys.*, A757:1–27, 2005. [27](#)
- [56] K. Adcox et al. Formation of dense partonic matter in relativistic nucleus–nucleus collisions at rhic: Experimental evaluation by the {PHENIX} collaboration. *Nuclear Physics A*, 757(1–2):184 – 283, 2005. First Three Years of Operation of {RHIC}. [27](#)
- [57] B.B. Back et al. The {PHOBOS} perspective on discoveries at {RHIC}. *Nuclear Physics A*, 757(1–2):28 – 101, 2005. First Three Years of Operation of {RHIC}. [27](#)

- [58] J. Adams et al. Experimental and theoretical challenges in the search for the quark–gluon plasma: The {STAR} collaboration’s critical assessment of the evidence from {RHIC} collisions. *Nuclear Physics A*, 757(1–2):102 – 183, 2005. First Three Years of Operation of {RHIC}. [27](#)
- [59] Barbara V. Jacak and Berndt Müller. The exploration of hot nuclear matter. *Science*, 337(6092):310–314, 2012. [27](#)
- [60] Natasha Sharma, Tony Perez, Andy Castro, Lokesh Kumar, and Christine Nattrass. Methods for separation of deuterons produced in the medium and in jets in high energy collisions. *Phys. Rev.*, C98(1):014914, 2018. [27](#)
- [61] R. Thomas, Burkhard Kampfer, and G. Soff. Gluon emission of heavy quarks: Dead cone effect. *Acta Phys. Hung.*, A22:83–91, 2005. [29](#)
- [62] Shanshan Cao, Tan Luo, Guang-You Qin, and Xin-Nian Wang. Heavy and light flavor jet quenching at rhic and lhc energies. *Physics Letters B*, 777:255 – 259, 2018. [30](#)
- [63] Michael L. Miller, Klaus Reygers, Stephen J. Sanders, and Peter Steinberg. Glauber modeling in high energy nuclear collisions. *Ann. Rev. Nucl. Part. Sci.*, 57:205–243, 2007. [30](#)
- [64] Klochkov and I Selyuzhenkov and. Centrality determination in heavy-ion collisions with the CBM experiment. *Journal of Physics: Conference Series*, 798:012059, jan 2017. [30](#)
- [65] James L. Nagle and William A. Zajc. Small System Collectivity in Relativistic Hadronic and Nuclear Collisions. *Ann. Rev. Nucl. Part. Sci.*, 68:211–235, 2018. [32](#)

- [66] Wenbin Zhao, You Zhou, Hao jie Xu, Weitian Deng, and Huichao Song. Hydrodynamic collectivity in proton–proton collisions at 13 tev. *Physics Letters B*, 780:495 – 500, 2018.

[32](#)

- [67] STEPHEN MYERS. The large hadron collider 2008–2013. *International Journal of Modern Physics A*, 28(25):1330035, 2013. [33](#)

- [68] Thomas Taylor and Daniel Treille. The Large Electron Positron Collider (LEP): Probing the Standard Model. *Adv. Ser. Direct. High Energy Phys.*, 27:217–261, 2017.

[33](#)

- [69] G. Aad et al. The ATLAS Experiment at the CERN Large Hadron Collider. *JINST*, 3:S08003, 2008. [33](#)

- [70] S. Chatrchyan et al. The CMS Experiment at the CERN LHC. *JINST*, 3:S08004, 2008. [33](#)

- [71] A. Augusto Alves, Jr. et al. The LHCb Detector at the LHC. *JINST*, 3:S08005, 2008. [33](#)

- [72] K. Aamodt et al. The ALICE experiment at the CERN LHC. *JINST*, 3:S08002, 2008. [33](#)

- [73] Serguei Chatrchyan et al. Observation of a new boson at a mass of 125 GeV with the CMS experiment at the LHC. *Phys. Lett.*, B716:30–61, 2012. [33](#)

- [74] Georges Aad et al. Observation of a new particle in the search for the Standard Model Higgs boson with the ATLAS detector at the LHC. *Phys. Lett.*, B716:1–29, 2012. [33](#)

[75] C. Fabjan and J. Schukraft. The Story of ALICE: Building the dedicated heavy ion detector at LHC. In '*The Large Hadron Collider: A marvel technology*', EPFL-Press Lausanne, Switzerland, 2009 (Editor: L. Evans), chapter 5.4, 2011. [36](#)

[76] Vladimir V. Gligorov, Simon Knapen, Benjamin Nachman, Michele Papucci, and Dean J. Robinson. Leveraging the ALICE/L3 cavern for long-lived exotics. 2018.

[37](#)

[77] M. Bondila et al. ALICE T0 detector. *IEEE Trans. Nucl. Sci.*, 52:1705–1711, 2005.

[37](#)

[78] E. Abbas et al. Performance of the ALICE VZERO system. *JINST*, 8:P10016, 2013.

[39](#)

[79] Rick Field. Min-Bias and the Underlying Event at the LHC. *Acta Phys. Polon.*, B42:2631–2656, 2011. [40](#)

[80] Constantin Loizides. Glauber modeling of high-energy nuclear collisions at the subnucleon level. *Phys. Rev.*, C94(2):024914, 2016. [40](#)

[81] S. Beolè. The alice inner tracking system: Performance with proton and lead beams. *Physics Procedia*, 37:1062 – 1069, 2012. Proceedings of the 2nd International Conference on Technology and Instrumentation in Particle Physics (TIPP 2011). [39](#)

[82] Jaroslav Adam et al. Particle identification in ALICE: a Bayesian approach. *Eur. Phys. J. Plus*, 131(5):168, 2016. [39](#)

- [83] S. Tangwancharoen et al. A Gating Grid Driver for Time Projection Chambers. *Nucl. Instrum. Meth.*, A853:44–52, 2017. [42](#)
- [84] Christian Lippmann. Performance of the alice time projection chamber. *Physics Procedia*, 37:434 – 441, 2012. Proceedings of the 2nd International Conference on Technology and Instrumentation in Particle Physics (TIPP 2011). [43](#)
- [85] A Fantoni and the ALICE collaboration. The alice electromagnetic calorimeter: Emcal. *Journal of Physics: Conference Series*, 293(1):012043, 2011. [43](#)
- [86] Olivier Bourrion, R Guernane, B Boyer, JL Bouly, and G Marcotte. Level-1 jet trigger hardware for the alice electromagnetic calorimeter at lhc. *Journal of Instrumentation*, 5(12):C12048, 2010. [46](#)
- [87] O Bourrion, N Arbor, G Conesa-Balbastre, C Furget, R Guernane, and G Marcotte. The alice emcal l1 trigger first year of operation experience. *Journal of Instrumentation*, 8(01):C01013, 2013. [46](#)
- [88] Jiri Kral, Terry Awes, Hans Muller, Jan Rak, and Joachim Schambach. {L0} trigger for the {EMCal} detector of the {ALICE} experiment. *Nuclear Instruments and Methods in Physics Research Section A: Accelerators, Spectrometers, Detectors and Associated Equipment*, 693:261 – 267, 2012. [46](#)
- [89] G Apollinari, I Béjar Alonso, O Brüning, M Lamont, and L Rossi. High-Luminosity Large Hadron Collider (HL-LHC) : Preliminary Design Report. 2015. [48](#)
- [90] Levente Molnar and the ALICE Collaboration. Upgrade and physics perspective of alice at the lhc. *Journal of Physics: Conference Series*, 589(1):012014, 2015. [49](#)

- [91] T L Karavicheva and ALICE Collaboration. The fast interaction trigger detector for the alice upgrade. *Journal of Physics: Conference Series*, 798(1):012186, 2017. [49](#)
- [92] B Abelev and all. Technical Design Report for the Upgrade of the ALICE Inner Tracking System. Technical Report CERN-LHCC-2013-024. ALICE-TDR-017, Nov 2013. [49](#)
- [93] Technical Design Report for the Muon Forward Tracker. Technical Report CERN-LHCC-2015-001. ALICE-TDR-018, Jan 2015. [49](#)
- [94] P Buncic, M Krzewicki, and P Vande Vyvre. Technical Design Report for the Upgrade of the Online-Offline Computing System. Technical Report CERN-LHCC-2015-006. ALICE-TDR-019, Apr 2015. [50](#)
- [95] Radoslaw Ryblewski and Michael Strickland. Dilepton production from the quark-gluon plasma using leading-order (3+1)D anisotropic hydrodynamics. *Acta Phys. Polon. Supp.*, 8(2):445, 2015. [50](#)
- [96] Mauricio Martinez and Michael Strickland. Measuring QGP thermalization time with dileptons. *Phys. Rev. Lett.*, 100:102301, 2008. [50](#)
- [97] F. Sauli. GEM: A new concept for electron amplification in gas detectors. *Nucl. Instrum. Meth.*, A386:531–534, 1997. [51](#)
- [98] Maxim Titov. Perspectives of Micro-Pattern Gaseous Detector Technologies for Future Physics Projects. In *Proceedings, CMS Workshop: Perspectives on Physics and on CMS at Very High Luminosity, HL-LHC: Alushta, Crimea, Ukraine, May 28–31, 2012*, pages 241–258, 2013. [51](#)

- [99] M Tang, A Q Liu, A Agarwal, and M H Habib. A single-mask substrate transfer technique for the fabrication of high-aspect-ratio micromachined structures. *Journal of Micromechanics and Microengineering*, 17(8):1575, 2007. [53](#)
- [100] W. You, Y. Zhou, J. Liu, M. Shao, C. Li, H. Chen, Z. Tang, Y. Sun, Y. Zhang, Y. Lv, G. Song, X. Wang, D. Hu, and D. Hong. A new technique for assembling large-size gem detectors. *Journal of Instrumentation*, 12(06):C06036, 2017. [53](#)
- [101] Fabio Sauli. The gas electron multiplier (gem): Operating principles and applications. *Nuclear Instruments and Methods in Physics Research Section A: Accelerators, Spectrometers, Detectors and Associated Equipment*, 805:2 – 24, 2016. Special Issue in memory of Glenn F. Knoll. [53](#)
- [102] Marco Santimaria and Davide Pinci. Study of the GEM detector for the LHCb experiment upgrade, Nov 2013. Presented 19 Dec 2013. [53](#)
- [103] Dorothea Pfeiffer, Lennert De Keukeleere, Carlos Azevedo, Francesca Belloni, Stephen Biagi, Vladimir Grichine, Leendert Hayen, Andrei R. Hanu, Ivana Hřivnáčová, Vladimir Ivanchenko, Vladyslav Krylov, Heinrich Schindler, and Rob Veenhof. Interfacing geant4, garfield++ and degrad for the simulation of gaseous detectors. *Nuclear Instruments and Methods in Physics Research Section A: Accelerators, Spectrometers, Detectors and Associated Equipment*, 935:121 – 134, 2019. [53](#)
- [104] S. Agostinelli et al. GEANT4: A Simulation toolkit. *Nucl. Instrum. Meth.*, A506:250–303, 2003. [53](#)
- [105] ALICE luminosity determination for pp collisions at $\sqrt{s} = 8$ TeV. Mar 2017. [68, 112](#)

- [106] O. Bourrion, R. Guernane, B. Boyer, J. L. Bouly, and G. Marcotte. Level-1 jet trigger hardware for the ALICE electromagnetic calorimeter at LHC. *JINST*, 5:C12048, 2010.

90

- [107] Shreyasi Acharya et al. Charged jet cross section and fragmentation in proton-proton collisions at $\sqrt{s} = 7$ TeV. *Phys. Rev.*, D99(1):012016, 2019. 76

- [108] Tim Adye. Unfolding algorithms and tests using RooUnfold. In *Proceedings, PHYSTAT 2011 Workshop on Statistical Issues Related to Discovery Claims in Search Experiments and Unfolding, CERN, Geneva, Switzerland 17-20 January 2011*, pages 313–318, Geneva, 2011. CERN, CERN. 96

- [109] G. Cowan. A survey of unfolding methods for particle physics. *Conf. Proc.*, C0203181:248–257, 2002. [,248(2002)]. 96

- [110] Betty Bezverkhny Abelev et al. Energy Dependence of the Transverse Momentum Distributions of Charged Particles in pp Collisions Measured by ALICE. *Eur. Phys. J.*, C73(12):2662, 2013. 107

- [111] R. Fruhwirth. Application of Kalman filtering to track and vertex fitting. *Nucl. Instrum. Meth.*, A262:444–450, 1987. 110

- [112] Gregory Soyez. A simple description of jet cross-section ratios. *Physics Letters B*, 698(1):59 – 62, 2011. 119

- [113] Rongrong Ma. Measurements of the inclusive jet cross section and jet fragmentation in pp collisions with the alice experiment at the lhc. *Nuclear Physics A*, 910-911:319 – 322, 2013. Hard Probes 2012. 119

[114] Betty Bezverkhny Abelev et al. Production of charged pions, kaons and protons at large transverse momenta in pp and Pb–Pb collisions at $\sqrt{s_{\text{NN}}} = 2.76$ TeV. *Phys. Lett.*, B736:196–207, 2014. [144](#)

Appendix

A Particle Identification via Bethe-Bloch

The energy loss of a relativistic charged particle traversing through a medium is given by

the Bethe-Bloch relation:

$$\frac{dE}{dx} \propto \frac{1}{\beta^2} \frac{Z}{A} \rho \left[\frac{1}{2} \ln \frac{2m_e c^2 \beta^2 \gamma^2 T_{max}}{I^2} - \beta^2 - \frac{\delta(\beta\gamma)}{2} \right] \quad (2)$$

where ρ is the density of the medium, $\frac{Z}{A}$ is the ratio of the atomic number to the atomic mass of the absorber, β is the ratio of the particle's momentum to energy, T_{max} is the maximum transfer energy from the charged particle to an electron in the medium, I^2 is the mean excitation energy of the medium, $\frac{\delta(\beta\gamma)}{2}$ is a correction factor based on the polarization of the material, and γ^2 is the lorentz factor $\frac{1}{\sqrt{1-\beta^2}}$.

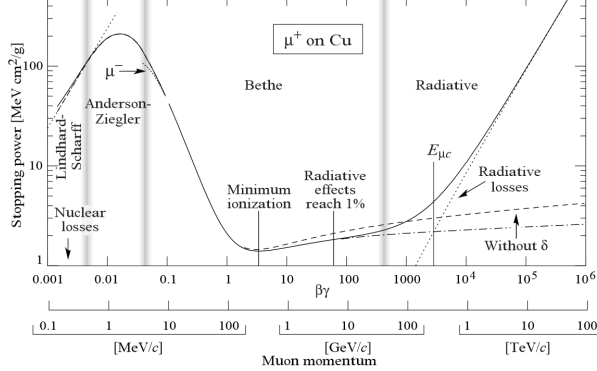


Figure 7: Energy loss of a muon traversing a copper medium between 0.1 MeV to 100 TeV [1].

Figure 7 shows the Bethe-Bloch curve for a muon over a wide kinematic range. At low energies the dominate form of energy loss is via elastic scattering, while at high energies radiation becomes the dominate energy loss mechanism. When $\beta\gamma \approx 3$ the muon loses the least amount of energy possible and is called a minimum ionization particle(MIP).

The ALICE ITS and TPC¹ cannot directly measure the energy loss of a particle traversing either sub-detector. Instead they perform PID by measuring the relative amplitudes from the sub-detector's read-out elements, pixels in the ITS and copper pads in the TPC. The amplitudes are then fit to the Bethe-Bloch equation as seen in Figure 8. Electrons weakly obey the Bethe-Bloch relationship in the kinematic ranges sensitive to the ITS and TPC and thus have a constant energy loss in both detectors.

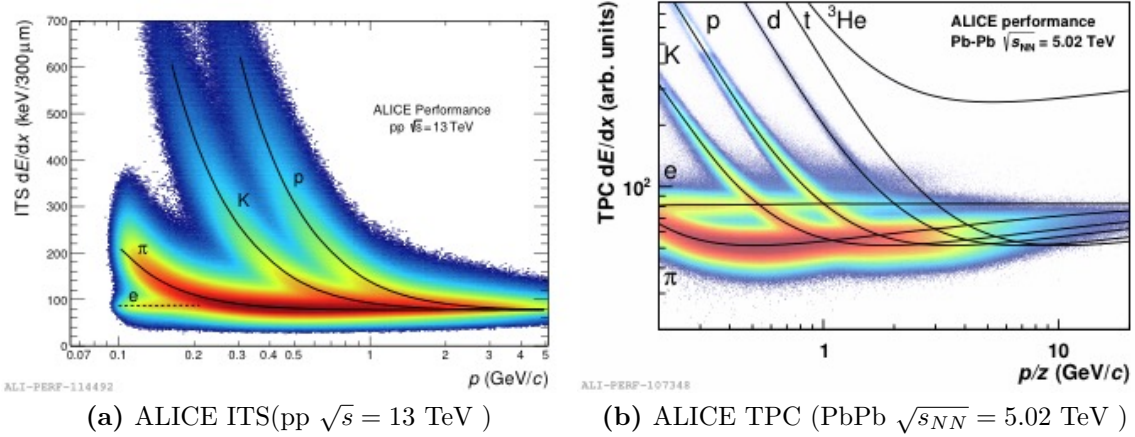


Figure 8: Specific energy loss for the ITS(*left*) and the TPC(*right*) with Bethe-Bloch fits from different particle species traversing each detector[30].

Figure 8 also shows that the Bethe-Bloch curves merge above some kinematic range, 4 GeV in the ITS and 10 GeV in the TPC. Above this kinematic range particles cannot be distinguished on a track-by-track basis, but by using statistical methods and Gaussian fits PID can be extended up to 20 GeV[114].

¹see Chapter 3

Vita

Andrew John Castro was born in San Jose, CA. He grew up in the San Francisco Bay Area and Mexico City. In 2012 he was awarded Bachelors of Science from the California Polytechnic University in Pomona, CA. During his undergraduate education, Andrew worked with Dr. Alex Small on simulating tumor growths and Dr. Antonio Auerilia on high energy physics. In 2011, Andrew spent 3 months at the Euorpean Organization for Nuclear Research (CERN) working with Dr. Tancredi Carli of the ATLAS experiment on parton distribution functions and jet physics. After his undergraduate studies, he entered the University of Tennessee pursuing a Ph.D in Physics. Andrew defended his thesis in 2019. During his time at Tennessee Andrew worked on developing trigger code for the ALICE EMCal, heavy flavor jets, light-nuclei production, hadronization, and Monte Carlo simulations. He also contributed to the upgrade of the ALICE Time Projection Chamber to a continuous readout mode using micro pattern gaseous detectors. Andrew currently works for the Space Radiation Analysis Group with NASA in Houston, Texas. His work is focused on the impact that heavy-ion radiation has on biological material and solutions to shield future manned missions in space.